

**A Measurement of the Atmospheric Neutrino Flux  
and Oscillation Parameters at the Sudbury  
Neutrino Observatory**

by

Thomas John Sonley

Submitted to the Department of Physics  
in partial fulfillment of the requirements for the degree of

Doctor of Philosophy in Physics

at the

MASSACHUSETTS INSTITUTE OF TECHNOLOGY

February 2009

© Massachusetts Institute of Technology 2009. All rights reserved.

Author .....  
Department of Physics  
January 9, 2009

Certified by .....  
Joseph Formaggio  
Assistant Professor  
Thesis Supervisor

Accepted by .....  
Thomas Greytak  
Associate Department Head for Education



# A Measurement of the Atmospheric Neutrino Flux and Oscillation Parameters at the Sudbury Neutrino Observatory

by

Thomas John Sonley

Submitted to the Department of Physics  
on January 9, 2009, in partial fulfillment of the  
requirements for the degree of  
Doctor of Philosophy in Physics

## Abstract

Through-going muon events are analyzed as a function of their direction of travel through the Sudbury Neutrino Observatory. Based on simulations and previous measurements, muons with a zenith angle of  $-1 < \cos(\theta_{zenith}) < 0.4$  are selected as atmospheric neutrino-induced muons. A two-neutrino analysis of these events agrees with the oscillation parameters observed by the Super Kamiokande and Minos experiments, and places 2-D limits of  $\Delta m_{23}^2 = 1.8_{-1.1}^{+7.1} \times 10^{-3} \text{ eV}^2$  at the 68% confidence level, and  $\sin^2(2\theta_{23}) > 0.33$  at the 90% confidence level. In addition, the flux of atmospheric neutrinos is measured in 1-D with a 68% confidence level to be  $1.24_{-0.10}^{+0.11}$  times the prediction of the BARTOL group based on SNO data alone, and  $1.27 \pm 0.09$  times the prediction when the oscillation parameters are constrained by the Super Kamiokande and Minos results.

Thesis Supervisor: Joseph Formaggio  
Title: Assistant Professor



## Acknowledgments

I would like to thank the SNO muon group, Joe Formaggio, Chris Kyba, Tyron Tsui, Feng Zhang, and Charles Currat for building a solid foundation for the atmospheric neutrino analysis. This thesis would not have been possible without their hard work setting up the simulations, writing the muon fitter, and helping to verify that everything was interfacing smoothly. Their work acquiring and fixing the EMuS system was also greatly appreciated. Ben Monreal, Rich Ott, and Jocelyn Monroe along with many people at Bates Lab and SNOLab were also instrumental in getting the EMuS system installed and analyzed.

I also would like to thank my lab mates at MIT, Grey Rybka, Asher Kaboth, Rich Ott and many others for their companionship and for helping me learn the computing skills necessary to complete this thesis.

In addition, I would like to thank my committee members, Joe Formaggio, Peter Fisher, and Krishna Rajagopal. Their thoughtful comments on this thesis have greatly improved it.

I have appreciated the support from my family, Ann, Jeff, and my late father John. They have humored my interest in science since an early age, and have supported me every step of the way from elementary school through graduate school.

Finally, I wish to thank my incredible wife Eleanor for her help and support for the last three years. It has been a long haul and I have been irrational at times, but you have always helped me get past the frustrations and back on track.



# Contents

<b>1</b>	<b>Introduction</b>	<b>15</b>
<b>2</b>	<b>Theory</b>	<b>17</b>
2.1	Neutrino Oscillations . . . . .	17
2.1.1	Atmospheric Neutrino Oscillations . . . . .	19
2.1.2	Measurement at SNO . . . . .	22
2.2	Atmospheric Neutrino Flux . . . . .	23
<b>3</b>	<b>The SNO Detector</b>	<b>29</b>
3.1	Muon Response . . . . .	33
<b>4</b>	<b>Muon Fitter</b>	<b>37</b>
4.1	Muon Fitter Performance . . . . .	39
<b>5</b>	<b>External Muon System</b>	<b>45</b>
5.1	Time to Radius Conversion . . . . .	48
5.2	Data Selection . . . . .	55
5.3	Reconstruction . . . . .	56
<b>6</b>	<b>Analysis</b>	<b>63</b>
6.1	Analysis Overview . . . . .	63
6.2	Simulations . . . . .	64
6.2.1	Cosmic Ray Muon Simulation . . . . .	65
6.2.2	Rock Neutrino Interaction Simulation . . . . .	66

6.2.3	Internal Neutrino Interaction Simulation . . . . .	67
6.3	Analysis Cuts . . . . .	67
6.3.1	Low Level Cuts . . . . .	68
6.3.2	High Level Cuts . . . . .	70
6.3.3	Phase Stability of Cut Variables . . . . .	73
6.3.4	Data - Monte Carlo Agreement of Cut Variables . . . . .	74
<b>7</b>	<b>Signal Extraction</b>	<b>81</b>
7.1	Analytical Pulls Technique . . . . .	82
7.2	Signal Extraction Validation . . . . .	84
7.3	Super Kamiokande and MINOS Constraints . . . . .	88
<b>8</b>	<b>Systematic Uncertainties</b>	<b>97</b>
8.1	Cross-Section Uncertainties . . . . .	97
8.2	Data - Monte Carlo Based Uncertainties . . . . .	98
8.3	Uncertainty Due To Measured Angular Misreconstruction . . . . .	102
8.4	Impact Parameter Bias Uncertainty . . . . .	102
8.5	Solar Modulation . . . . .	104
8.6	Other Uncertainties . . . . .	106
8.7	Summary . . . . .	106
<b>9</b>	<b>Results</b>	<b>109</b>
<b>10</b>	<b>Conclusions</b>	<b>117</b>

# List of Figures

2-1	Super Kamiokande Detector . . . . .	21
2-2	Super Kamiokande Atmospheric Neutrino Measurements . . . . .	24
2-3	Primary Cosmic Ray Spectrum . . . . .	26
2-4	Predicted Atmospheric Neutrino Spectrum . . . . .	27
3-1	Diagram of the SNO Detector . . . . .	31
3-2	SNO Photomultiplier Tubes . . . . .	31
3-3	Sample Central Muon Track in SNO . . . . .	34
3-4	Sample Clipping Muon Track in SNO . . . . .	35
4-1	FTI Charge Probability Comparison . . . . .	40
4-2	PMT Hit Time Distribution . . . . .	40
4-3	Muon Fitter Angular Misreconstruction Simulation . . . . .	41
4-4	Muon Fitter Multiple Scattering Simulation . . . . .	41
4-5	Muon Fitter Impact Parameter Misreconstruction Simulation . . . . .	43
4-6	Muon Fitter Reconstruction Correlation Simulation . . . . .	43
5-1	EMuS Scintillator Panels . . . . .	46
5-2	Location of the EMuS system on the SNO Deck . . . . .	49
5-3	Side View of the EMuS Experiment . . . . .	50
5-4	Back View of the EMuS Experiment . . . . .	50
5-5	EMuS Simulated Drift Time . . . . .	52
5-6	EMuS Drift Time Calculation Timing Cuts . . . . .	52
5-7	EMuS Drift Time Measurement . . . . .	54

5-8	Sample EMuS Track Fit . . . . .	60
5-9	Simulated Misreconstruction Distributions . . . . .	61
5-10	EMuS Angular Misreconstruction Data . . . . .	62
5-11	EMuS Impact Parameter Misreconstruction Data . . . . .	62
6-1	Phase Stability of Cut Variables for Neutrino-Induced Muons . . . . .	75
6-2	Phase Stability of Cut Variables for Cosmic Ray Muons . . . . .	76
6-3	Phase Stability of Cut Variables for Data . . . . .	77
6-4	Data-Monte Carlo Agreement of Cut Variables . . . . .	79
7-1	Likelihood as a function of systematic parameter . . . . .	85
7-2	Statistical Accuracy of Contours in the $\sin^2(2\theta)$ - $\Delta m^2$ Plane . . . . .	87
7-3	Statistical Accuracy of Contours in the Flux Multiplier - $\Delta m^2$ Plane . . . . .	87
7-4	Statistical Accuracy of Contours in the $\sin^2(2\theta)$ - Flux Multiplier Plane . . . . .	91
7-5	Signal Extraction Accuracy on $\Delta m^2$ . . . . .	92
7-6	Signal Extraction Accuracy on $\sin^2(2\theta)$ . . . . .	93
7-7	Signal Extraction Accuracy on the Flux Multiplier . . . . .	93
7-8	Super Kamiokande Contour Plot . . . . .	94
7-9	Approximation of the Super Kamiokande Contours . . . . .	94
7-10	MINOS Contour Plot . . . . .	95
7-11	Approximation of the MINOS Contours . . . . .	95
8-1	Systematic Uncertainty Due to $dE/dx$ Variation . . . . .	99
8-2	Systematic Uncertainty Due to $Q_{RMS}$ Variation . . . . .	100
8-3	Systematic Uncertainty Due to Linear Discriminant Variation . . . . .	101
8-4	Systematic Uncertainty Due To Angular Misreconstruction . . . . .	103
8-5	Impact Parameter Uncertainty Constraints . . . . .	105
8-6	Solar Modulation of Neutrino Flux . . . . .	105
8-7	Energies of Detected Neutrinos . . . . .	107
9-1	SNO Through-going Muon $\cos(\theta_{zenith})$ Distribution . . . . .	112
9-2	Oscillation Results in $\sin^2(2\theta)$ - $\Delta m^2$ Plane . . . . .	112

9-3	Oscillation Results in Flux Multiplier - $\Delta m^2$ Plane . . . . .	113
9-4	Oscillation Results in $\sin^2(2\theta)$ - Flux Multiplier Plane . . . . .	113
9-5	$\Delta m_{23}^2$ Likelihood Curve . . . . .	114
9-6	$\sin^2(2\theta_{23})$ Likelihood Curve . . . . .	114
9-7	Flux Multiplier Likelihood Curve . . . . .	115
9-8	Oscillation Results in $\sin^2(2\theta)$ - $\Delta m^2$ Plane Constrained by Super Kamiokande and MINOS Results . . . . .	115
9-9	Flux Multiplier Likelihood Curve With Constrained Oscillation Pa- rameters . . . . .	116



# List of Tables

2.1	Limits on Neutrino Oscillation Parameters . . . . .	19
3.1	Livetime for the Atmospheric Neutrino Analysis . . . . .	33
4.1	Muon Fitter Accuracy from Monte Carlo . . . . .	42
5.1	Uncertainties associated with wire positioning. . . . .	48
6.1	Through-going Muon Analysis Cuts . . . . .	68
6.2	Cut Efficiencies . . . . .	74
6.3	Cut Rejection Efficiencies . . . . .	76
6.4	Data-Monte Carlo Cut Variable Shifts . . . . .	78
7.1	Likelihood Values for Contours . . . . .	82
7.2	Fit Parameters for Oscillation Parameter Constraints . . . . .	89
8.1	Impact Parameter Uncertainty Constraints . . . . .	104
8.2	Systematic Uncertainties . . . . .	107
8.3	Analytical Pull Vectors . . . . .	108
9.1	Best Fit Floating Systematic Values . . . . .	110



# Chapter 1

## Introduction

In 1965, two experiments independently detected atmospheric neutrinos for the first time. These experiments, located deep underground in South Africa [1] and India [2], detected muons traveling horizontally, which could best be explained by the theoretical flux of muon neutrinos produced by cosmic rays. Since that time, many experiments have measured these atmospheric neutrinos including the Irvine Michigan Brookhaven Experiment (IMB) [3], Kamiokande [4], Frejus [5], and MACRO [6] among others. As measurements of electron and muon neutrinos from cosmic rays accumulated, it was found that the ratio between them was vastly different than predictions based off of cross-sections measured at accelerators. This was believed to be caused by neutrino oscillations.

In 2005, the Super Kamiokande experiment proved that this was the case by measuring the flux of electron and muon neutrinos as a function of their direction of travel through the detector [7]. This experiment provided an excellent measurement of the flux of low energy atmospheric neutrinos as well as the muon to tau neutrino oscillation parameters  $\Delta m_{23}^2$  and  $\theta_{23}$ . However because it was located in the side of a mountain, Super Kamiokande could not measure the raw flux of high energy atmospheric neutrinos. It could only observe high energy muon neutrinos from below the horizon, which have undergone oscillations. Thus the flux of high energy atmospheric neutrinos measured by Super Kamiokande is correlated with the oscillation parameters.

The Sudbury Neutrino Detector, because of its great depth and flat overburden can observe high energy atmospheric neutrinos both above and below the horizon, giving it the unique ability to measure both the neutrino flux and oscillation parameters with relatively high statistics. This thesis will detail an analysis of atmospheric neutrino-induced events in the SNO detector.

A more precise measurement of the flux of high energy atmospheric neutrinos would be useful in many ways. Neutrino telescopes such as AMANDA [8] and Baikal [9] search for neutrinos coming from objects outside of our solar system. Atmospheric neutrinos are both the calibration source and dominant background for these experiments, so a better measurement of the absolute flux of neutrinos will improve their results. In addition, the next generation of neutrino and dark matter detectors will need estimates of the atmospheric neutrino flux to calculate their backgrounds. An improved measurement of the flux will help them reduce the uncertainties on their measurements. Finally, improved measurements of the atmospheric neutrino flux will allow theorists to improve their models of cosmic ray showers which may improve estimates of extremely high energy interaction cross-sections.

# Chapter 2

## Theory

### 2.1 Neutrino Oscillations

Neutrino oscillations occur because neutrinos interact in their flavor eigenstates, but propagate in their mass eigenstates. Thus if a neutrino is created in an electron eigenstate, after traveling for some distance it will have a lower probability of interacting in an electron eigenstate, and a higher probability of interacting in a muon or tau state. In the standard formulation of neutrino oscillations [10], a neutrino of definite flavor  $|\nu_\alpha\rangle$  is a superposition of neutrinos of definite mass  $|\nu_i\rangle$ :

$$|\nu_\alpha\rangle = \sum_i U_{\alpha i}^* |\nu_i\rangle \quad (2.1)$$

where  $U$  is a unitary mixing matrix of the form:

$$U = \begin{pmatrix} 1 & 0 & 0 \\ 0 & c_{23} & s_{23} \\ 0 & -s_{23} & c_{23} \end{pmatrix} \times \begin{pmatrix} c_{13} & 0 & s_{13}e^{-i\delta} \\ 0 & 1 & 0 \\ -s_{13}e^{i\delta} & 0 & c_{13} \end{pmatrix} \times \begin{pmatrix} c_{12} & s_{12} & 0 \\ -s_{12} & c_{12} & 0 \\ 0 & 0 & 1 \end{pmatrix} \times \begin{pmatrix} e^{i\alpha_1/2} & 0 & 0 \\ 0 & e^{i\alpha_2/2} & 0 \\ 0 & 0 & 1 \end{pmatrix} \quad (2.2)$$

where  $c_{ij}$  is shorthand for  $\cos \theta_{ij}$  while  $s_{ij}$  is shorthand for  $\sin \theta_{ij}$ . This equation contains three mixing angles ( $\theta_{12}$ ,  $\theta_{23}$ , and  $\theta_{13}$ ), one charge-parity (CP) violating phase ( $\delta$ ), and two Majorana phases ( $\alpha_1$  and  $\alpha_2$ ). There are no Standard Model predictions for these parameters so they must be measured through experiments. The overall matrix is broken into these four matrices because each matrix is evident in different neutrino oscillation regimes. The first matrix represents mixing between the muon and tau neutrinos through  $\theta_{23}$ . This mixing has been observed in high energy atmospheric neutrino [7] and beamline experiments [11, 12]. The second matrix represents mixing between electron and tau neutrinos through  $\theta_{13}$ , and includes the CP violating phase. This matrix should be seen as a second order effect in any other oscillation experiment. The third matrix represents mixing between electron and muon neutrinos through  $\theta_{12}$ . This mixing is observed in reactor neutrinos [13] and in solar neutrino experiments [14, 15] through the Mikheyev-Smirnov-Wolfenstein (MSW) effect [16, 17]. The last matrix differs from the identity matrix only if neutrinos are Majorana particles, and would show up in neutrinoless double beta decay experiments [18].

The most precisely measured oscillation parameters come from electron neutrino disappearance from the sun and from nuclear reactors. A global fit to these two methods [13] yields  $\tan^2(\theta_{12}) = 0.47_{-0.05}^{+0.06}$  and  $\Delta m_{12}^2 = 7.59 \pm 0.21 \times 10^{-5} \text{ eV}^2$  at the 68% confidence level. Muon neutrino disappearance measurements at higher energies give the best limits on muon to tau neutrino oscillations. Super Kamiokande [7] has measured  $\sin^2(2\theta_{23}) > 0.92$  at the 90% confidence level using atmospheric neutrinos, while MINOS [11] has measured  $\Delta m_{23}^2 = 2.74_{-0.26}^{+0.44} \times 10^{-3} \text{ eV}^2$  at the 68% confidence level using a neutrino beam. Oscillations from electron to tau neutrinos have not been seen, although the CHOOZ experiment [19] has placed a limit of  $\sin^2(2\theta_{13}) < 0.19$  at the 90% confidence level. Because these oscillations have not been detected, no limits have been placed on  $\Delta m_{13}^2$  or the CP violating phase. Neutrinoless double beta decay has not been observed, so no limits can be placed on the majorana phases.

While in general the formula for oscillations is very complicated, a simplified two neutrino model can be used with reasonable accuracy. This simplification works

Oscillation Parameter	Confidence Level	Source
$\tan^2(\theta_{12}) = 0.47_{-0.05}^{+0.06}$	1-D 68%	Solar + KamLAND [13]
$\Delta m_{12}^2 = 7.59 \pm 0.21 \times 10^{-5} \text{ eV}^2$	1-D 68%	Solar + KamLAND [13]
$\sin^2(2\theta_{23}) > 0.92$	2-D 90%	Super Kamiokande [7]
$\Delta m_{23}^2 = 2.74_{-0.26}^{+0.44} \times 10^{-3} \text{ eV}^2$	1-D 68%	MINOS [11]
$\sin^2(2\theta_{13}) < 0.19$	2-D 90%	CHOOZ [19]
$\Delta m_{13}^2$ has never been observed.		

Table 2.1: Current limits on neutrino oscillation parameters.

because  $\Delta m_{12}^2$  and  $\Delta m_{23}^2$  are separated by an order of magnitude and  $\sin^2(2\theta_{13})$  is small. In addition, atmospheric neutrinos have large energies, so the MSW effect is insignificant. For atmospheric neutrino oscillations, the two-neutrino oscillation formula is:

$$P(\nu_\mu \rightarrow \nu_\mu) = 1 - \sin^2(2\theta_{23}) \sin^2\left(1.27\Delta m_{23}^2 \frac{L}{E}\right) \quad (2.3)$$

where  $\Delta m_{23}^2$  is the difference in squared masses of the neutrino mass eigenstates in  $\text{eV}^2$ ,  $L$  is the distance the neutrino has traveled in km, and  $E$  is the neutrino energy in GeV. In almost all cases it is fair to use this two particle mixing assumption rather than the full three particle formalism. This equation will be used to predict the disappearance of muon neutrinos and the appearance of tau neutrinos in the atmospheric neutrino flux.

### 2.1.1 Atmospheric Neutrino Oscillations

Atmospheric neutrinos are produced in cosmic ray showers. A primary cosmic ray from outer space (usually a proton or Helium nucleus) interacts in the upper atmosphere, producing a shower of hadrons and mesons. Some of these mesons (primarily pions and kaons) decay via the weak interaction and produce muons and muon neutrinos. The muons travel down through the atmosphere and are stopped after traveling a few kilometers through the surface of the earth. In the Sudbury Neutrino Observatory (SNO), these cosmic ray muons are seen traveling downward through the detector. The muon neutrinos travel straight through the earth because of their low cross-section with matter. While the majority of these atmospheric neutrinos pass

through the earth without interacting, one will occasionally interact within the earth to produce a muon that can pass through the SNO detector. If the neutrino was produced on the far side of the earth, the resulting neutrino induced muon will be seen traveling upward through the detector. By measuring the flux of these upward-going muons, SNO can measure the flux of atmospheric neutrinos.

The best measurement of atmospheric neutrinos comes from the Super Kamiokande experiment due to its large detector volume and long livetime [7]. The Super Kamiokande detector is a cylindrical water Cherenkov detector that contains 50 kilotons of ultra-pure light water observed by 11146 Photomultiplier Tubes (see figure 2-1). It is located in a mountain in Kamioka, Japan under an overburden of 2700 meters water equivalent. Figure 2-2 shows the measured flux of electron and muon neutrinos along with their fit to the oscillation parameters. The three leftmost plots show the measured flux of electron neutrinos. Since there is no excess of electron neutrinos compared to theoretical predictions, it can be inferred that the disappearing muon neutrinos must be oscillating into tau neutrinos. The eight plots to the right show the flux of muon neutrinos as a function of zenith angle. There are eight plots because neutrino-induced muons with different energies produce different event topologies in the detector. In general, the plots to the lower right have higher energy. The top six plots on the right ( $\mu$ -like and PC) come from muon neutrino interactions within the detector, allowing neutrinos from all directions to be measured. The bottom two plots (Upward stopping  $\mu$  and Upward through-going  $\mu$ ) come from neutrino-induced muons which enter the detector. Since the neutrino interaction vertex cannot be detected, there is no way to tell the difference between a cosmic ray muon and a neutrino-induced muon other than by its direction. Super Kamiokande is located in the side of a mountain so cosmic ray muons can come in horizontally. Only upward-going muons are included in these fluxes to reduce the contamination from cosmic ray muons.

The different energy regions provide different information about the oscillation parameters. The level of the deficit of upward going internal muon neutrino interactions measures  $\sin^2(2\theta_{23})$ , while the slope of the upward stopping muon plot and

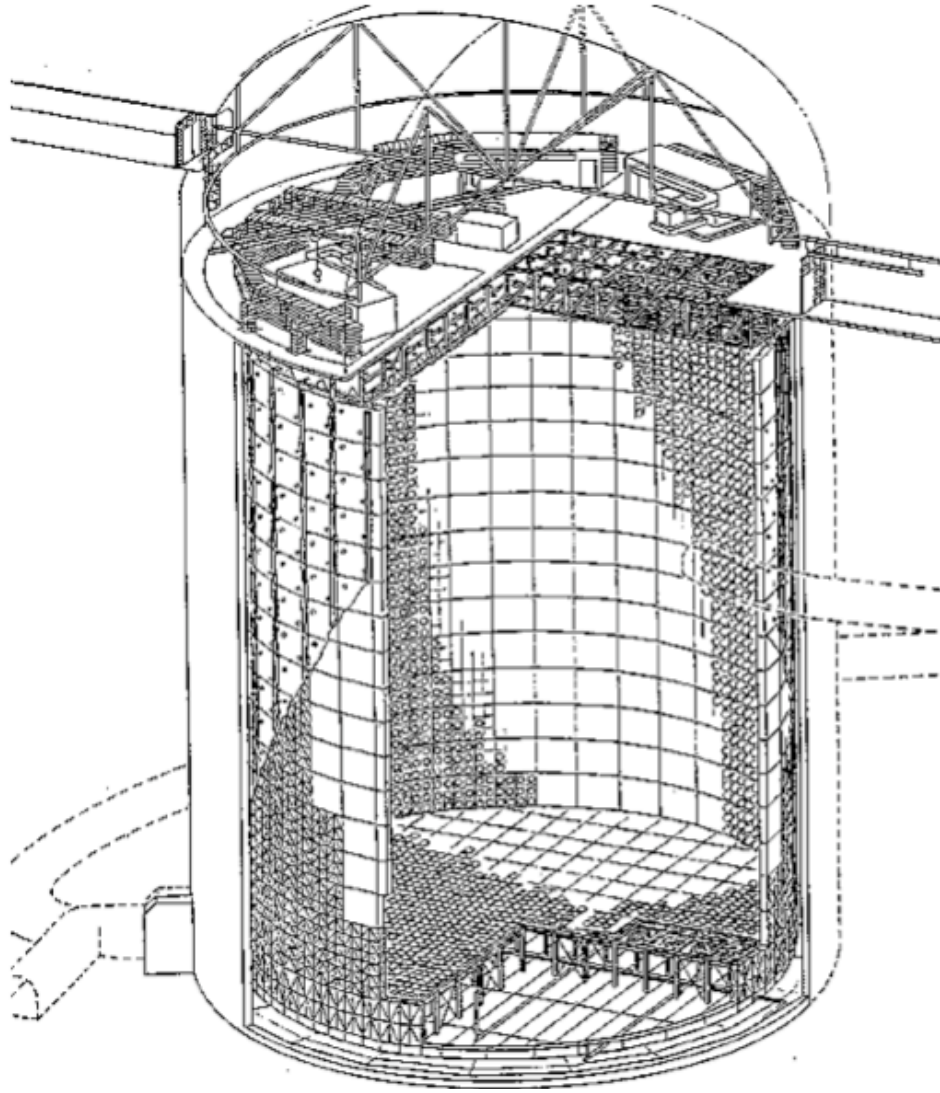


Figure 2-1: A drawing of the Super Kamiokande detector. The cutaway shows the inside lined with photomultiplier tubes comprising a photocathode coverage of about 40%. The thin outer region is shown with a sparser density of outward facing PMTs. Taken from [7].

the upward through-going muon plot give the largest constraint on  $\Delta m_{23}^2$ . However, the slope of these plots also has a component due to the raw flux of atmospheric neutrinos. While to first order, the flux of atmospheric neutrinos should be the same from all directions, the changing density of the atmosphere gives a shape to the atmospheric neutrino flux independent of oscillations. High energy muon neutrinos are created by the decay of high energy pions and kaons. However these mesons travel through the atmosphere, and can lose energy or be destroyed by strong interactions with gas nuclei. This becomes a large effect when the mean free path of the meson is comparable to its decay length. Since the mean free path is proportional to the density of gas atoms, mesons traveling downward through the atmosphere produce fewer high energy muon neutrinos than those traveling horizontally through the atmosphere. Horizontal mesons produce neutrinos that are observed at  $\cos(\theta_{zenith})$  near 0, while downward mesons produce neutrinos that are observed near  $\pm 1$ . This produces an excess of neutrinos near  $\cos(\theta_{zenith}) = 0$  which can be seen in the no oscillations prediction (boxes) in the PC (partially contained) plot in figure 2-2. The same excess occurs in the upward stopping muon and upward through-going muon distributions, and gives a shape that is similar to the effect of  $\Delta m_{23}^2$ . Thus if the flux of atmospheric neutrinos at high energy could be independently constrained, the limits on  $\Delta m_{23}^2$  could be improved.

### 2.1.2 Measurement at SNO

Although the Sudbury Neutrino Observatory is a smaller detector than Super Kamiokande and will thus have lower statistics, it is able to observe atmospheric neutrinos in a region that Super Kamiokande cannot. The rate of internal neutrino interactions scales with the volume of the detector. Since Super Kamiokande has around 20 times the volume of SNO, SNO will not be competitive for internal neutrino interactions. However the rate of through-going neutrino-induced muons is proportional to the area of the detector, and Super Kamiokande has only 5 times the area of SNO and a similar livetime. More importantly, SNO is located deep underground under a flat overburden. Because of this, cosmic ray muons coming in at large angles lose all of

their energy before they reach the detector. This means that SNO has a region from  $0 < \cos(\theta_{zenith}) < 0.4$  in which it can observe through-going neutrino-induced muons that Super Kamiokande could not. These neutrinos will not have traveled far enough to oscillate, so this region will measure the raw flux of atmospheric neutrinos. This measurement of the flux of atmospheric neutrinos will be useful in refining models of the atmospheric neutrino flux and improving estimates of backgrounds in neutrino oscillation, dark matter, and neutrino telescope experiments.

## 2.2 Atmospheric Neutrino Flux

In order to measure neutrino oscillations, the flux of atmospheric neutrinos must be known. Groups such as Honda, et al. [20] and the BARTOL group [21] have calculated the expected flux of atmospheric neutrinos. These calculations use the measured flux of primary cosmic rays as an input and simulate cosmic ray showers to estimate the flux of atmospheric neutrinos. The simulations attempt to model the solar system correctly by taking into account including solar modulation, the geomagnetic cutoff, bending of showers due to the earth's magnetic field, and the location of different detectors [22]. They also attempt to use the most up to date cosmic ray fluxes and cross-sections. There are, however, significant uncertainties associated with the calculations. Different models for hadron production in high energy collisions produce different numbers of pions and kaons at different energies. Differences in simulations lead to around a 10% uncertainty in the expected flux of atmospheric neutrinos [23]. The measured flux of cosmic rays also has uncertainties. As seen in figure 2-3, the flux of cosmic rays is well measured at low energies by the AMS (Alpha Magnetic Spectrometer) [24] and BESS (Balloon-borne Experiment with Superconducting Spectrometer) [25, 26] experiments. However at higher energies there are fewer measurements and significantly larger uncertainties on the flux. This leads to a 15% uncertainty on the expected flux of atmospheric neutrinos at SNO [23].

These uncertainties are not only on the overall normalization of the atmospheric

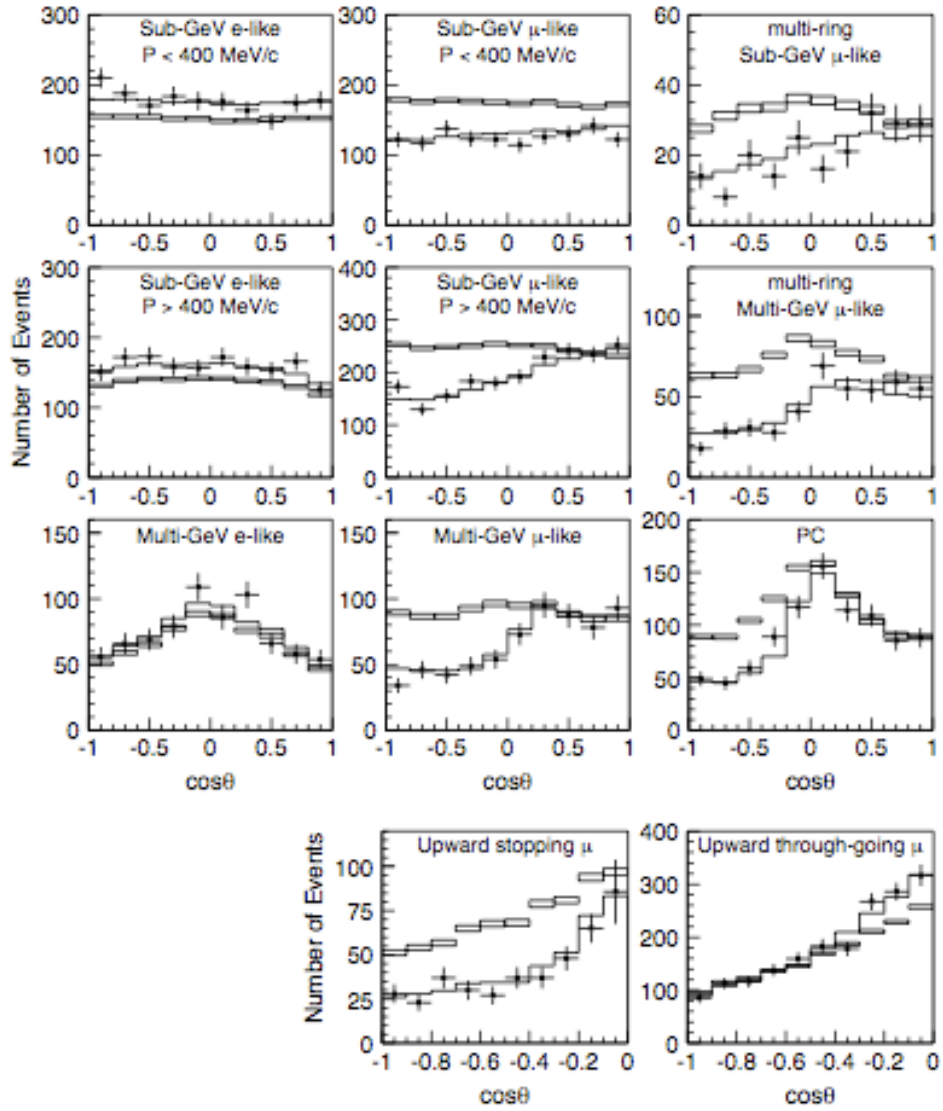


Figure 2-2: Atmospheric Neutrino Flux as a function of zenith angle measured by the Super Kamiokande experiment [7]. The crosses represent the measured flux while the boxes represent the no oscillation prediction and the lines represent the best fit flux including oscillations.

neutrino flux, but also on the energy scaling of the flux. However these energy scaling uncertainties are difficult to include in the analysis, and are most important for precision measurement of the oscillation parameters. Since SNO is expected to have lower statistics than Super Kamiokande, SNO's measurement of the flux of atmospheric neutrinos will be more important than it's measurement of the oscillation parameters. In order to perform this measurement, the neutrino flux calculated by the BARTOL group (see figure 2-4) will be used as the input atmospheric neutrino flux, and uncertainties on the energy scaling will be ignored. The measurement of the flux of atmospheric neutrinos will thus be a measurement of how much the normalization of the BARTOL flux must be changed to fit SNO's data.

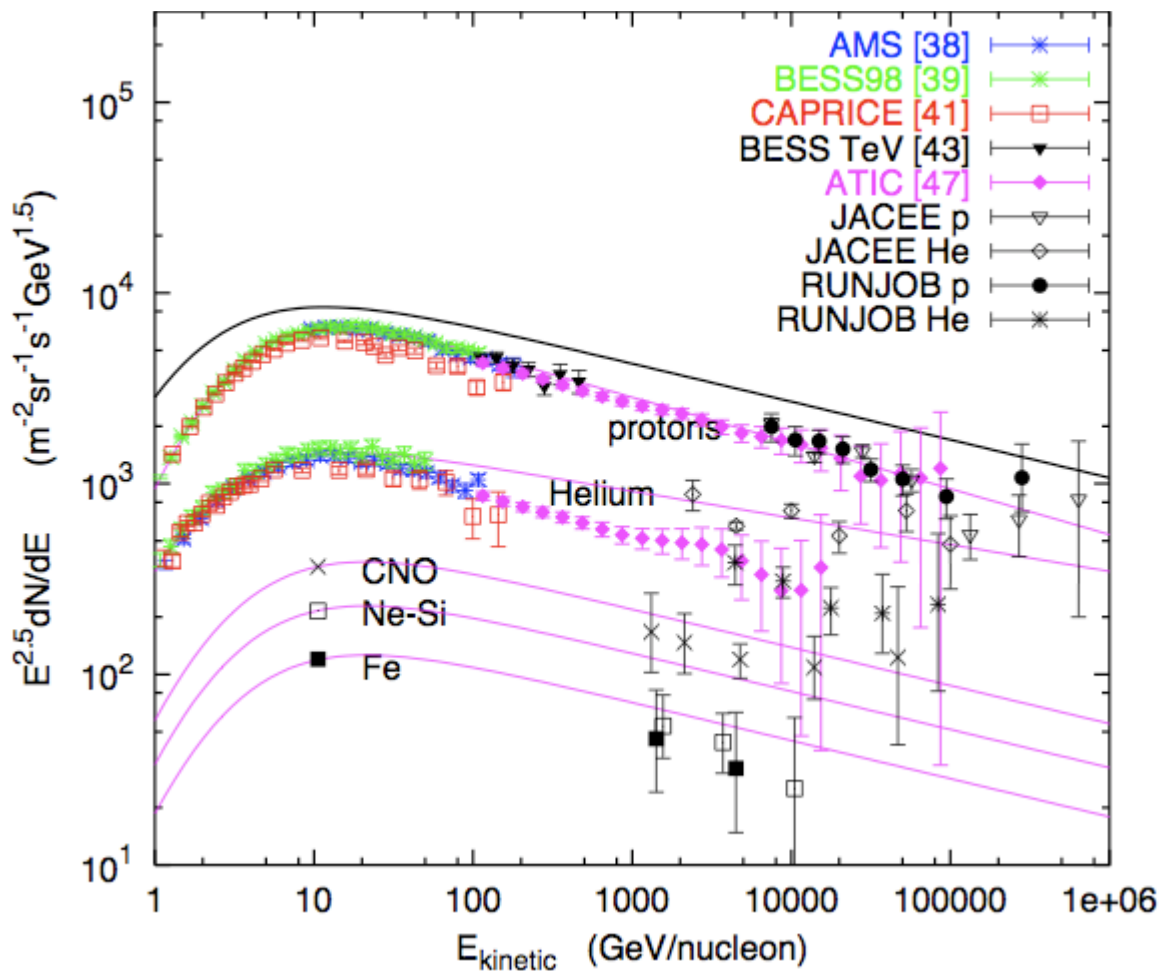


Figure 2-3: Spectrum of cosmic rays seen by various experiments [24, 25, 27, 26, 28, 29, 30, 31]. Fits to this spectrum [32] are used as an input to calculate the flux of atmospheric neutrinos. Taken from [23].

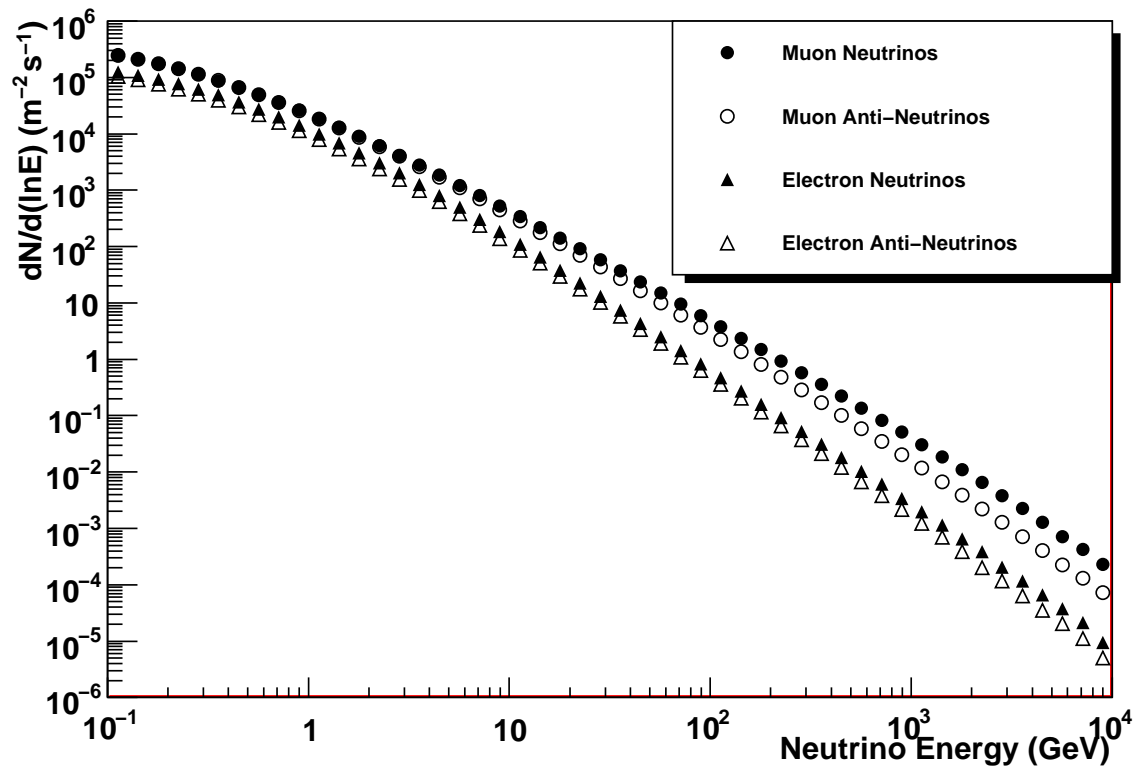


Figure 2-4: Spectrum of atmospheric neutrinos predicted by the BARTOL group [21]. While the prediction is a function of azimuthal and polar angles, this spectrum has been integrated over all directions.



# Chapter 3

## The SNO Detector

The SNO Detector is a large water-Cherenkov detector optimized for observing solar neutrinos. The detector is filled with heavy water which provides two unique interaction mechanisms for studying solar neutrinos. In the first interaction, the charged current interaction ( $\nu_e + d \rightarrow p + p + e^-$ ), an electron neutrino interacts with a deuteron to produce two protons and an energetic electron which is observed in the detector. In the second interaction, the neutral current interaction ( $\nu_x + d \rightarrow p + n + \nu_x$ ), a neutrino of any flavor scatters off of a deuteron, breaking it apart. The neutron is then captured on another nucleus and that capture is detected in a variety of ways depending on the phase of SNO. A third interaction, the elastic scattering interaction ( $\nu_x + e^- \rightarrow \nu_x + e^-$ ), is also present. In this interaction, a neutrino interacts with an electron, giving it more energy so that it can be detected. Any flavor of neutrino can participate in this interaction through the exchange of a Z boson, but electron neutrinos may also exchange a W boson, making this reaction more sensitive to electron neutrinos. Previous results from SNO ([14] and [33] among others) have demonstrated that the total flux of solar neutrinos as measured by the neutral current interaction is consistent with the standard solar model. However the flux of electron neutrinos as measured by the charged current and elastic scattering reactions is around three times lower, indicating that electron neutrinos from the sun oscillate into other neutrino flavors.

The SNO experiment has been described in great detail in journal articles [34,

33, 14] and theses [35, 36, 37]. This section will review the aspects most relevant to the atmospheric neutrino analysis. The detector consists of 1 kiloton of heavy water contained in a 6m radius acrylic sphere (see figure 3-1). The acrylic sphere is surrounded by an array of photomultiplier tubes (PMTs) at a radius of 850 cm. Ultra-pure light water fills the volume between the acrylic vessel and the PMTs. The detector is located in a cylindrical cavity in the rock. The volume between the cavity walls and the detector is filled with light water, and observed by 91 outward-looking PMTs. These PMTs serve as a muon veto for the solar neutrino analysis. The detector is nearly spherically symmetric except for the neck. The neck is a 6.8m tall, 1.5m diameter cylinder at the top of the detector used to deploy calibration sources. There are no PMTs in the neck, except for 4 PMTs at the top which are used to veto light leaks.

The heavy water region is observed by 9438 20 inch diameter Hamamatsu R1408 PMTs which provide 31% photocathode coverage. This is extended to 54% through the use of 27 cm light concentrators mounted around the PMTs (see figure 3-2). The PMTs are run at approximately 2kV, for a gain of  $10^7$ . Each PMT is independently triggered by a programmable threshold crossing discriminator. Once the discriminator fires the PMT charge is recorded using two integrator circuits set at high and low gains. Each circuit is read out twice, at early and late times. Three quantities are measured: the high gain integrated charge at short (QHS) and long (QHL) times, and the low gain integrated charge at long times (QLL). The global trigger system sums the total number of hit PMTs and their charge at all times using analog electronics. The system has multiple triggering modes, the most important of which for this analysis is the NHIT trigger. If enough PMTs fire (roughly 20 for most solar neutrino data taking), the trigger system sends a global trigger signal to all of the readout cards and records the time between the discriminator firing and the global trigger as well as QHS, QHL, and QLL. If fewer PMTs fire than the trigger threshold, the charge and timing of those PMT hits are discarded.

The detector is located in the Creighton mine in Sudbury, Ontario, Canada at a depth of 2072 m under a flat overburden. This corresponds to  $5891 \pm 94$  meters water

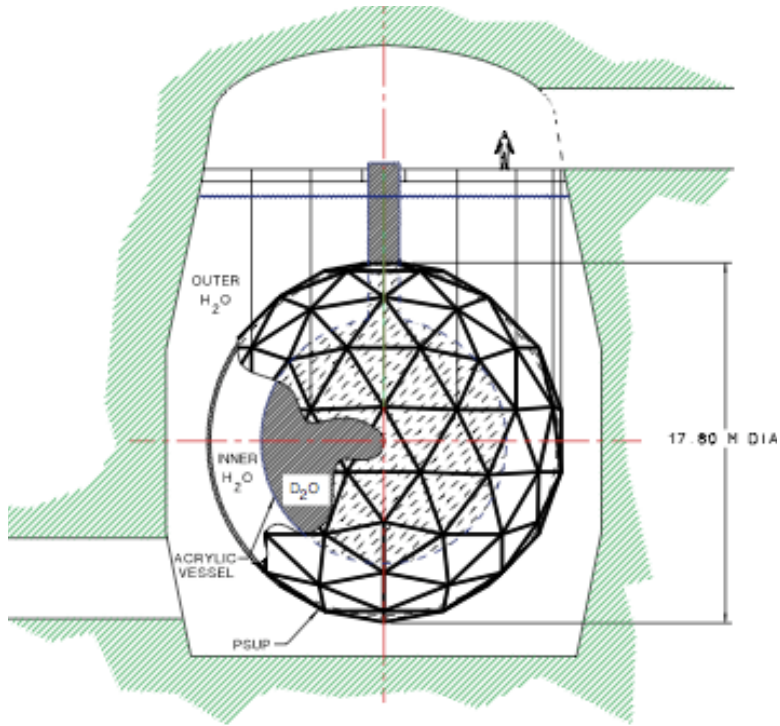


Figure 3-1: The SNO detector inside of the rock cavity. The black triangles represent the PMT support structure, while the the dark grey region represents the acrylic sphere and neck. Taken from [34].



Figure 3-2: A view of the SNO photomultiplier tubes. Note the flower petal-like reflectors around each PMT. These serve to increase the photocathode coverage of the detector by 75%.

equivalent. Only very energetic cosmic ray muons can reach this depth, resulting in a rate of 3 cosmic ray muons passing through the detector per hour. In addition, these muons come in almost vertically. Almost no cosmic ray muons are expected to come in with  $\theta_{zenith}$  less than 66 degrees.

The SNO detector went through three distinct phases in order to reduce systematic uncertainties on the solar neutrino measurement. In the first phase, pure heavy water ( $D_2O$ ) was used as both the target and the detector medium. Neutrinos of all three flavors interact with the deuteron via the neutral current weak interaction, releasing a neutron. The neutron is subsequently captured on another deuteron, producing tritium and releasing a photon. SNO's neutral current measurement is thus a neutron counting experiment. In the second phase, salt was added to the heavy water. The  $^{35}Cl$  in the salt has a larger neutron capture cross-section and releases a higher energy photon, which changes the systematics of the neutral current measurement. Finally, in the third phase, independent  $^3He$  proportional counters (NCDs) were added to the detector. These counters detect neutrons by the reaction  $^3He + n \rightarrow p + ^3H$ . The energy released in this interaction is carried by the proton and triton, which ionize electrons in the gas, producing a pulse on the wire running through the center of the counters. Since these detectors are read out by oscilloscopes rather than PMTs, they have completely different noise profiles and dead times, and thus uncorrelated systematic uncertainties.

Data from all three phases will be used in the atmospheric neutrino analysis. The  $D_2O$  phase data was collected from November 2nd, 1999 to May 28th, 2001. The Salt phase data was recorded between July 26th, 2001 and August 28th, 2003, while the NCD phase data was collected between November 27th, 2004 and November 28th, 2006. The data is collected in runs that range from 30 minutes to 96 hours in length. Runs that are flagged with unusual circumstances (presence of calibration sources, detector maintenance, high noise rates, etc.) are removed from the analysis. The livetime of the data set is measured using a GPS-synchronized 10 MHz clock on a run-by-run basis. The uncertainty of the livetime is estimated by comparing with a 50 MHz system clock. Corrections to the livetime are made due to certain data

Phase	Livetime
D <sub>2</sub> O	337.262 ± 0.019 days
Salt	499.425 ± 0.016 days
NCD	392.560 ± 0.005 days

Table 3.1: Livetime for the atmospheric neutrino analysis for each phase.

selection cuts. The total livetime used in the atmospheric neutrino analysis is 1229.30 ± 0.03 days. Table 3.1 shows the breakdown of that livetime by phase.

### 3.1 Muon Response

While the SNO detector was designed to observe low energy solar neutrinos, it can also track high energy muons. A muon track at SNO has a few distinguishing features. First, muons are the highest energy particles seen at SNO, and thus they deposit the most energy. While a typical solar neutrino interaction may fire 30 PMTs, a muon that grazes the edge of the detector will fire hundreds of PMTs, and a muon that travels through the center of the detector may fire every PMT. Secondly, muons produce Cherenkov radiation along their entire track. This shows up as a filled in circle of hit PMTs as can be seen in figure 3-3. For muons that graze the edge of the detector, the light concentrators around the PMTs add a triangular region next to the circle as can be seen in figure 3-4. In addition the Cherenkov light travels directly from the muon, so the timing of the PMT hits gives information about the path of the muon. Finally, the muon deposits a significant amount of energy near its track, which produces an "entry wound" and "exit wound" of high charge PMTs which are not visible in the figures.

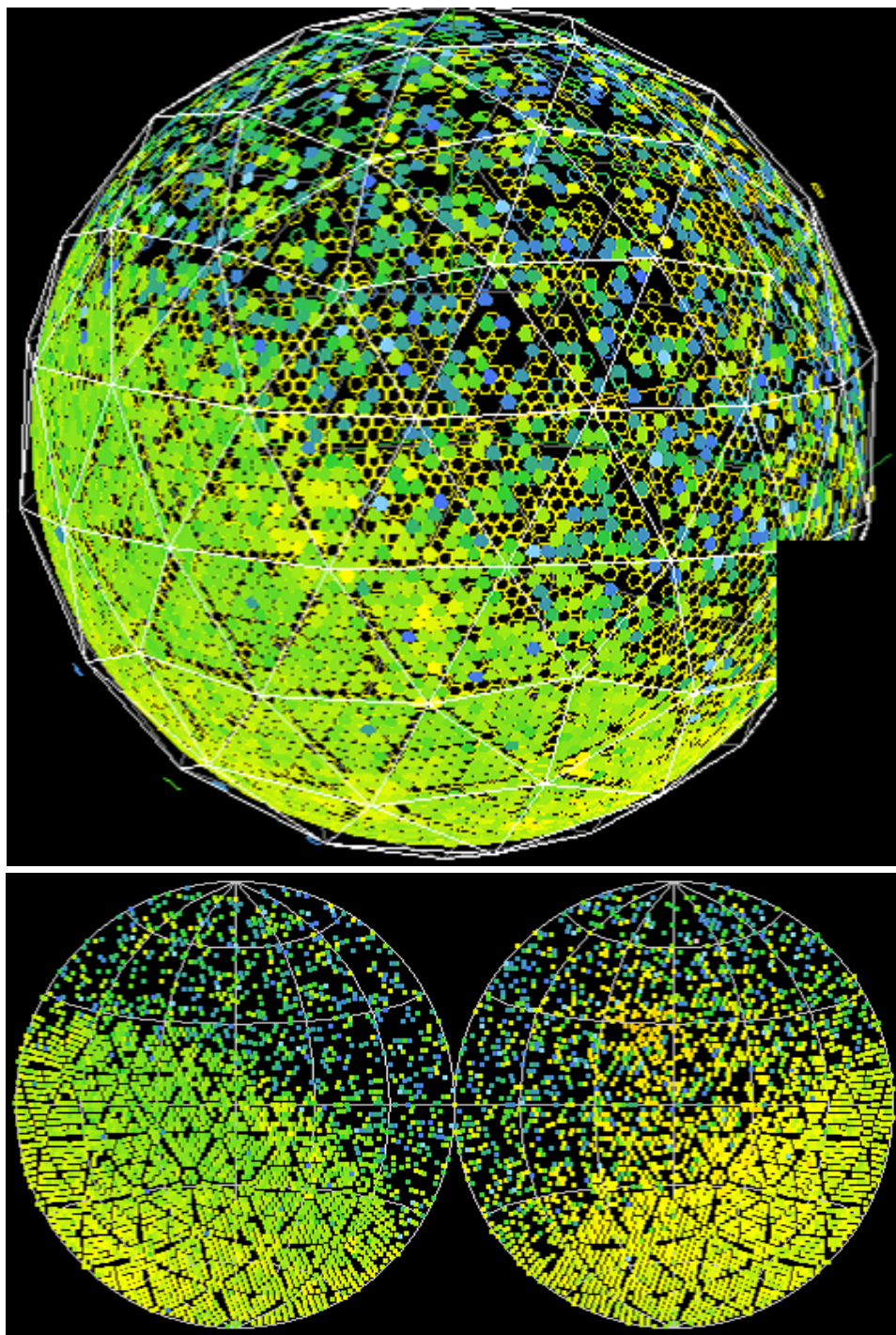


Figure 3-3: A muon track in the SNO detector visualized using the XSNOED event viewer. This muon came from the upper front right, passed near the center of the detector, and exited to the lower back left. The color represents the timing of each PMT hit. Yellow PMTs were hit earlier, while green were hit later.

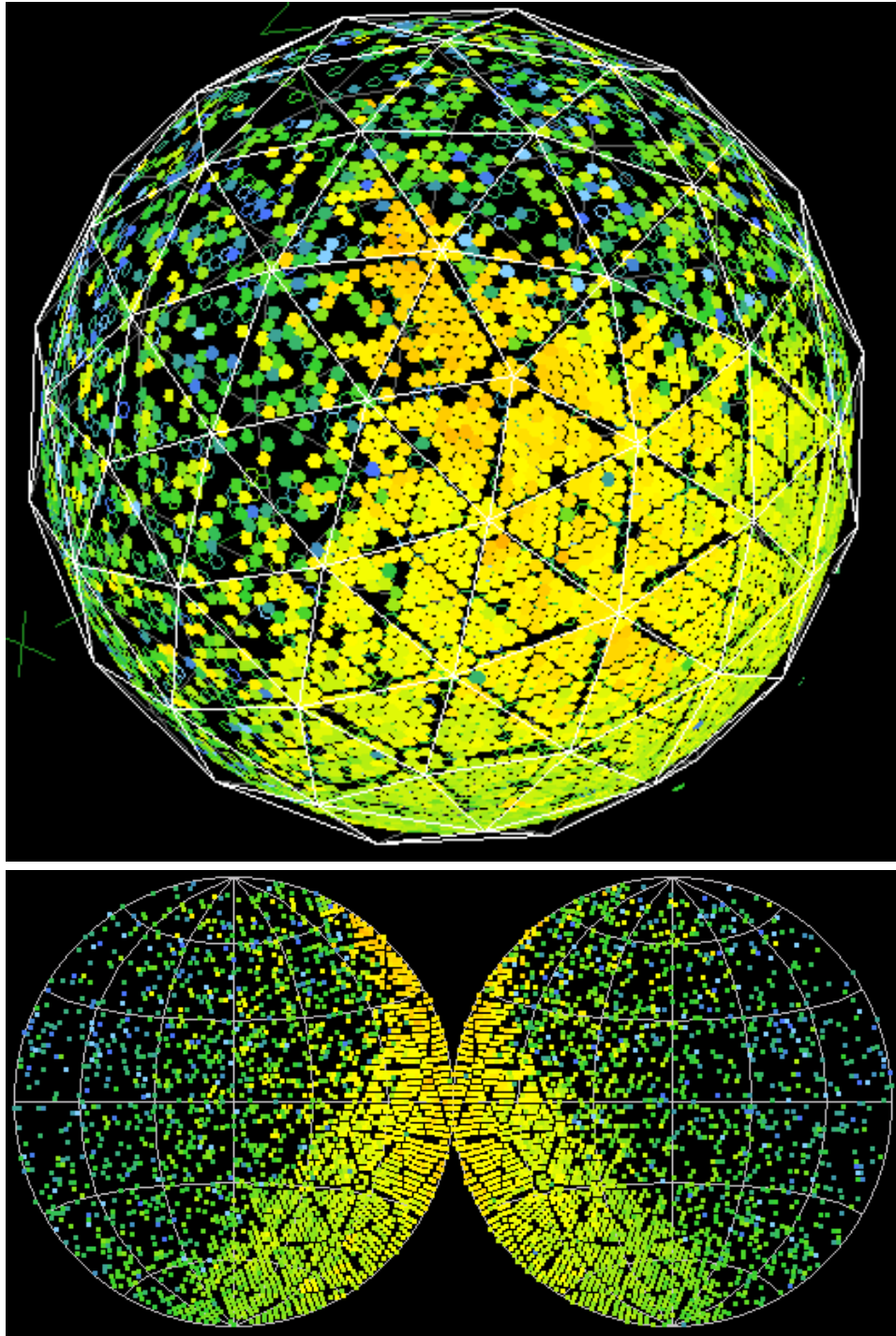


Figure 3-4: A muon track in the SNO detector visualized using the XSNOED event viewer. This muon came from the upper front left, stayed near the edge of the detector, and exited to the lower front right. Note the orange triangular feature in the center of the top picture. This is characteristic of muons with large impact parameters, and is caused by the light concentrators on the PMTs.



# Chapter 4

## Muon Fitter

The FTI muon fitter fits for a through-going muon track [35]. It uses the distribution of hit PMTs along with their charge and timing in a likelihood fit for four quantities: the muon's direction, impact parameter, deposited energy, and a time offset. The likelihood is defined as:

$$L = \prod_{PMTs} \left[ \sum_{n=1}^{\infty} P_N(n|\lambda) P_Q(Q|n) P_T(t|n) \right] \quad (4.1)$$

Where  $\lambda$  is the expected number of photons for that PMT,  $P_N(n|\lambda)$  is the poisson probability of seeing  $n$  photons hit the PMT,  $P_Q(Q|n)$  is the probability of seeing charge  $Q$  given  $n$  photon hits, and  $P_T(t|n)$  is the probability of observing a PMT trigger at time  $t$  given  $n$  photon hits.

The heart of the fitter lies in the first probability term, which is calculated based on Monte Carlo simulations. Chris simulated muons at 108 impact parameter points with random directions through the detector. Based on these simulations, he created lookup tables for how many photons are expected to hit a PMT at a given position with respect to a muon with a certain impact parameter. These lookup tables essentially fit the impact parameter and track direction to line up the Cherenkov ring.

The second term further refines the fit by including the charge information from the PMTs, and allows an estimate of the total energy deposited by the muon, correcting for offline PMTs and the neck of the detector. This probability was calculated

by simulating multiple photon hits on all of the PMTs in SNO. For a given number of photon hits ( $n$ ), the resulting charge ( $Q$ ) distribution is fit to a two-sided gaussian. The three parameters from these fits are then plotted as a function of photon hits and fit again, resulting in [35]:

$$P_Q(Q|n) = \begin{cases} N \exp\left(\frac{-(Q-\bar{Q})^2}{2\sigma_1^2}\right) & Q < \bar{Q} \\ N \exp\left(\frac{-(Q-\bar{Q})^2}{2\sigma_2^2}\right) & Q > \bar{Q} \end{cases} \quad (4.2)$$

$$N = \frac{\sqrt{2}S}{\sqrt{\pi}(\sigma_1 + \sigma_2)} \quad (4.3)$$

$$\bar{Q} = -2.3531 + 0.83075n \quad (4.4)$$

$$\sigma_1 = -1.7565 + 0.7807\sqrt{n} \quad (4.5)$$

$$\sigma_2 = 1.1351 + 0.77393\sqrt{n} \quad (4.6)$$

where  $S$  is a scale factor determined by the histogram binning. Figure 4-1 demonstrates that this fit model agrees very well with the simulations for many photon hits, and acceptably for few photon hits.

The third term in the likelihood refines the fit by including the PMT timing. For each PMT, the time residual can be calculated as:

$$t_{res} = t_{PMT} - t_0 - \frac{d_1}{c} - \frac{d_2}{21.8\text{cm/ns}} \quad (4.7)$$

where  $t_{PMT}$  is the recorded PMT time,  $t_0$  is a the time offset term in the likelihood fit,  $d_1$  is the distance the muon travels before emitting the Cherenkov photon,  $c$  is the speed of light in vacuum, and  $d_2$  is the distance the Cherenkov photon traveled. The Cherenkov photon is assumed to have an angle of  $42^\circ$  with respect to the muon track, making  $d_1$  and  $d_2$  well-defined. With this definition of the time residual, the timing probability term becomes:

$$P_T \sim \frac{1}{\sigma\sqrt{2\pi}} e^{-\frac{t_{res}^2}{2\sigma^2}} \quad (4.8)$$

This equation is then modified to include estimates of prepulsing, late light, and dark noise as a function of the number of expected photon hits [35]. Figure 4-2 demonstrates that for multiple photon hits, the prepulsing probability rises while the probability of late light decreases.

FTI minimizes the likelihood function for the impact parameter, direction, deposited energy, and timing offset using the method of simulated annealing. After the minimization, the likelihood is discarded, and a set of data quality measurements are calculated based on the fit track. These data quality measurements are used in section 6.3 to select through-going muon events.

## 4.1 Muon Fitter Performance

The FTI muon fitter is found to have good reconstruction accuracy on simulated muons. Figure 4-3 shows the misreconstruction angle between the Monte Carlo generated muon direction ( $\vec{u}_g$ ) and the reconstructed muon direction ( $\vec{u}_r$ ):

$$\theta_{mr} = \cos^{-1}(\vec{u}_g \cdot \vec{u}_r) \quad (4.9)$$

This is fit to:

$$p(x) = A\theta(fe^{-\frac{\theta^2}{2\sigma^2}} + (1-f)e^{-\frac{\theta^2}{2(m\sigma)^2}}) \quad (4.10)$$

The extra factor of  $\theta$  is due to phase space arguments. The fit parameters are:  $\sigma = 0.4^\circ$ ,  $f = 0.99$ , and  $m = 4$ . Although the tails are non-gaussian, this fit gives a reasonable estimate for the uncertainty due to angular misreconstruction. One possible source of this width is multiple scattering. Figure 4-4 shows the misreconstruction angle vs the multiple scattering angle:

$$\theta_{ms} = \cos^{-1}[(\vec{p}_{ex} - \vec{p}_g) \cdot \vec{u}_g] \quad (4.11)$$

$\vec{p}_g$  is the generation point of the muon while  $\vec{p}_{ex}$  is the point where the monte carlo muon left the SNO detector. This plot shows that while there is a correlation between

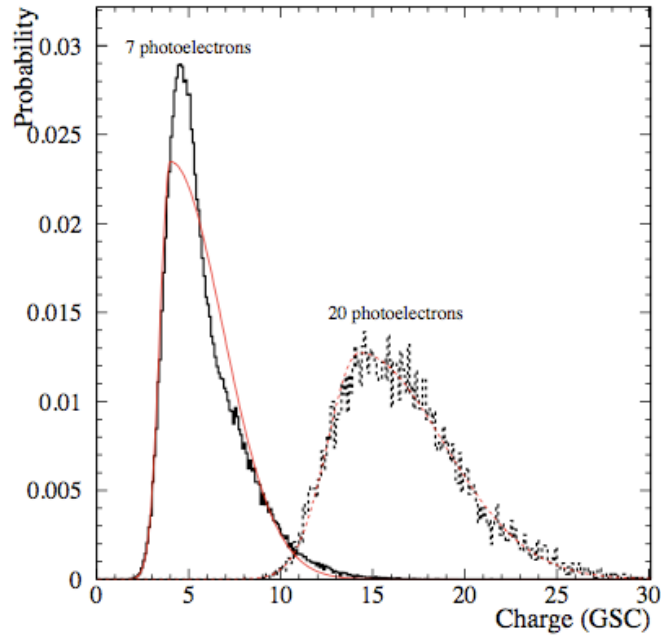


Figure 4-1: Comparison of simulated PMT charge distributions (black) to the model from equation 4.2 (red) used in the FTI fitter [35].

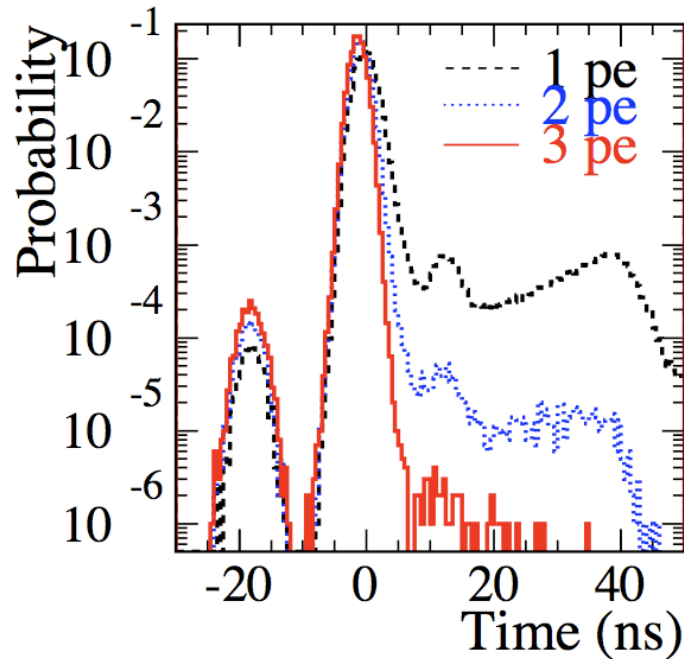


Figure 4-2: Distribution of PMT hit times for multiple photon hits. The black curve shows the distribution of hit times for a single photon hit. The bump at -20 ns comes from PMT prepulsing, while the distribution from 20 ns to 40 ns comes from reflections in the detector and physics processes such as Rayleigh scattering. Taken from [35].

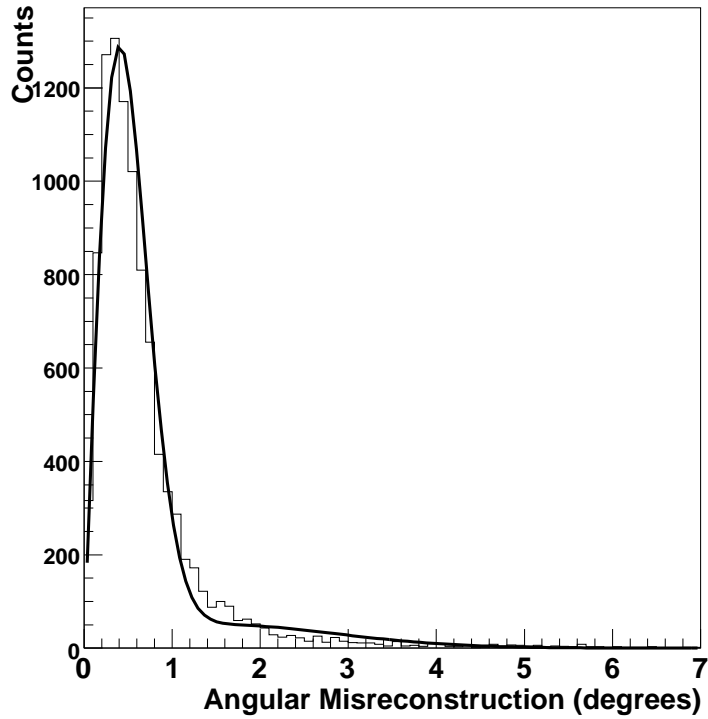


Figure 4-3: FTI Muon Fitter angular misreconstruction of Monte-Carlo muon tracks. The fit parameters are given in table 4.1

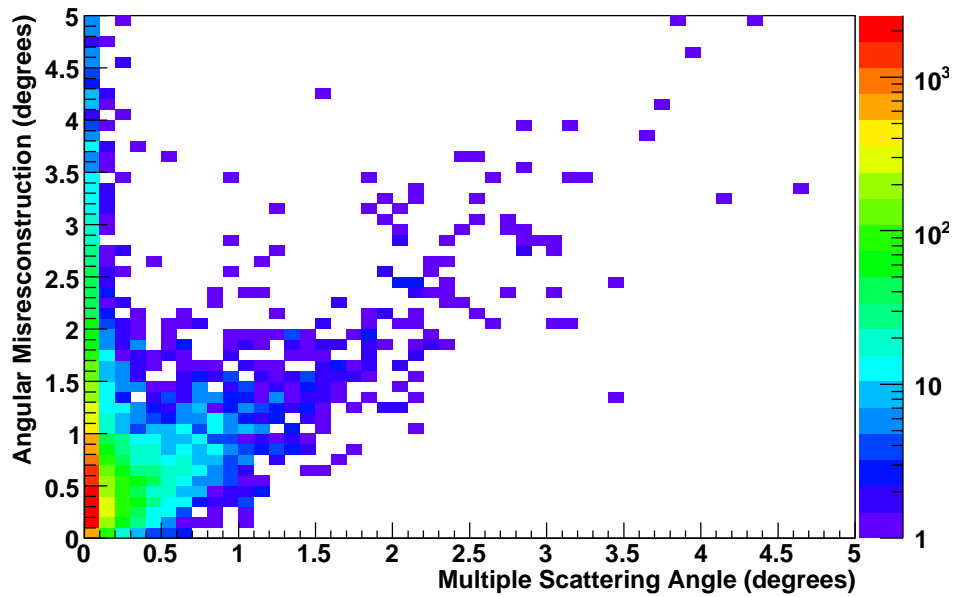


Figure 4-4: FTI angular misreconstruction vs multiple scattering angle for simulated events. There is a correlation between multiple scattering and misreconstruction for scattering angles larger than  $1^\circ$ . However there is not enough multiple scattering to account for the misreconstruction width seen in figure 4-3.

	Mean of Gaussians	Width of Main Gaussian	Weight of Secondary Gaussian	Width of Secondary Gaussian
Angular Misreconstruction		0.4°	1%	1.6°
Impact Parameter Misreconstruction	-0.08 cm	3.0 cm	1.2%	21 cm

Table 4.1: Accuracy of the muon fitter based on Monte Carlo simulations. The forms of the gaussians are given in equations 4.10 and 4.12

multiple scattering and misreconstruction, multiple scattering is not the dominant effect. Eighty percent of the muons were scattered by less than  $0.1^\circ$ , and those muons have the same misreconstruction width as before. Thus the  $0.4^\circ$  width is intrinsic to the fitter.

The impact parameter reconstruction accuracy is shown to be very good in figure 4-5. This is fit to the sum of two gaussians:

$$p(x) = A(fe^{-\frac{(x-\mu)^2}{2\sigma^2}} + (1-f)e^{-\frac{(x-\mu)^2}{2(m\sigma)^2}}) \quad (4.12)$$

where the fit parameters are  $\mu = -0.08$  cm,  $\sigma = 3.0$  cm,  $f = 0.988$ , and  $m = 7$ . It is possible that misreconstruction in angle is correlated with misreconstruction in impact parameter. However figure 4-6 demonstrates that the two are uncorrelated.

Based on these simulations, the muon fitter is extremely accurate. The direction of the muon is reconstructed to better than  $0.5^\circ$ , while the impact parameter is reconstructed to better than 3 cm in a 17 m diameter detector. These reconstruction accuracies are very reasonable for an atmospheric neutrino analysis.

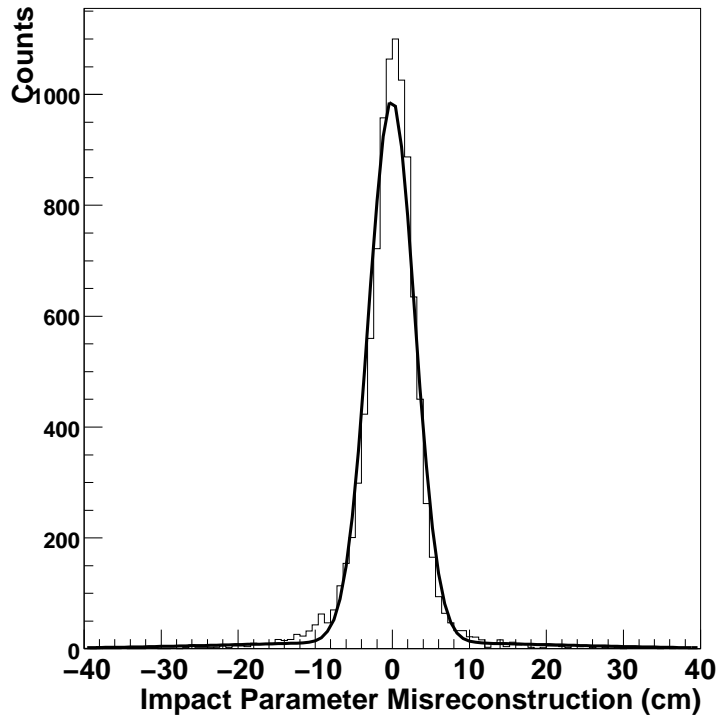


Figure 4-5: FTI impact parameter misreconstruction of Monte-Carlo muon tracks. The fit parameters are given in table 4.1

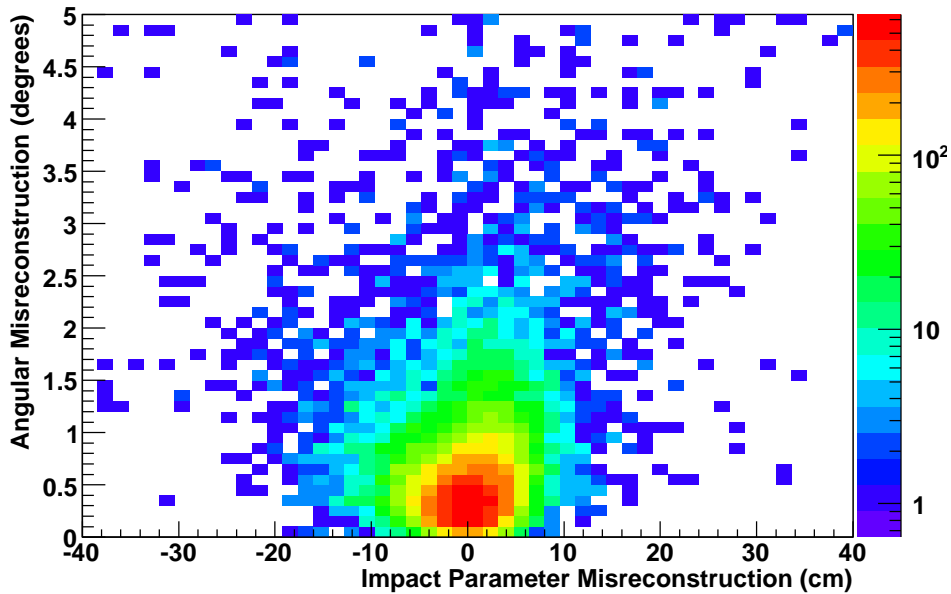


Figure 4-6: FTI angular misreconstruction vs impact parameter reconstruction. This pattern is consistent with  $x$  times a gaussian multiplied by a gaussian, implying that the parameters are uncorrelated.



# Chapter 5

## External Muon System

The SNO External Muon System (EMuS) is intended to provide a cross-check on the accuracy of the FTI muon fitter independent of Monte Carlo simulations. In order to accomplish that objective, a tracking detector was installed above the SNO detector. This section will detail the physical properties of the detector, the methods used to reconstruct tracks, and the agreement between the FTI fitter and the reconstructed tracks.

The External Muon System consists of a series of 128 single-wire chambers arranged into four planes and triggered by 3 large scintillator panels (See Figure 5-3). The panels have been reused from the KARMEN experiment, and consist of Bicron BC412 scintillator read out at each end by four 2 inch Photonis XP2262 Photomultiplier Tubes (PMTs). Figure 5-1 shows the geometry of the panels. The wire chamber cells and electronics were provided by the University of Indiana, Bloomington, IN. Each cell is 7.5 cm wide and has square cross-section with the corners trimmed, providing a near-octagonal shape. The cells are 2.564 meters in length and possess a single 50  $\mu\text{m}$  diameter tungsten wire running through the center. The wire is held at a positive potential of 2500 V (2700 V) while running on the surface (underground) for electron drift and collection. A gas mixture of 90% Ar-10% CO<sub>2</sub> has been used in order to achieve high efficiency and stability, and to meet safety regulations for underground operations.

When a muon passes through the system, it deposits energy in the scintillator and

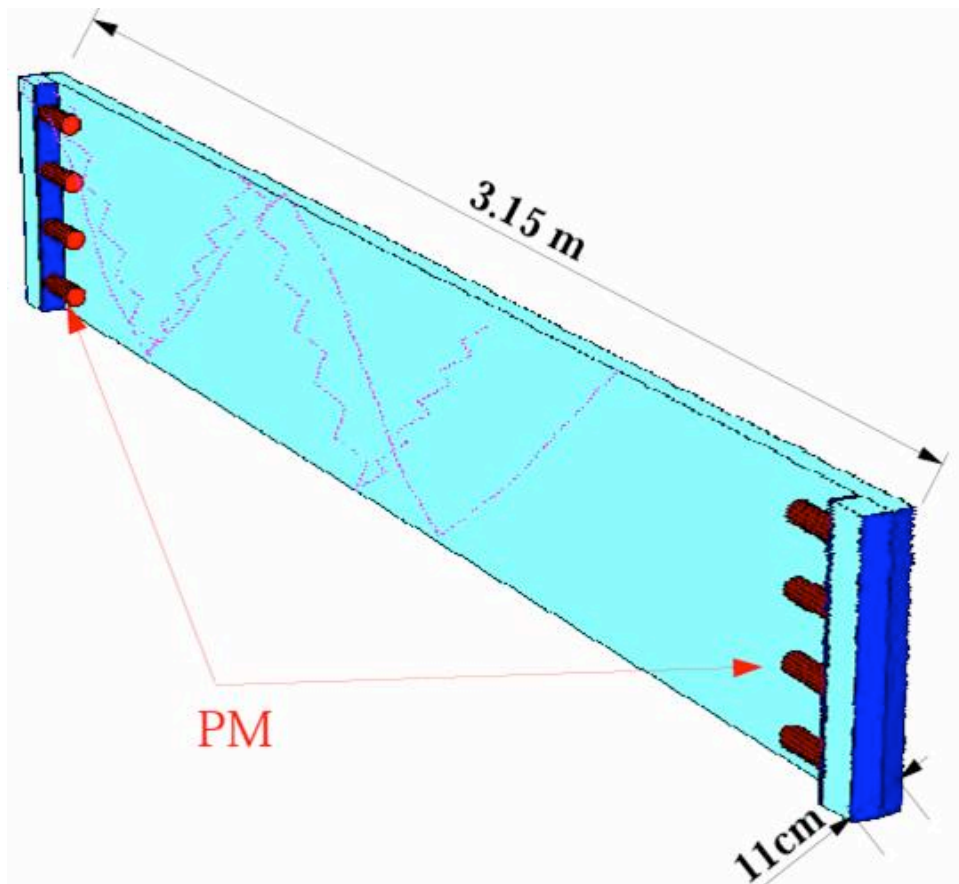


Figure 5-1: The layout of the scintillator panels used in the EMuS detector. The red cylinders represent the readout Photomultiplier Tubes.

ionizes atoms in each of the wire chambers it passes through. The scintillator converts the energy into light that is then detected by the PMTs in a fast process ( $\sim$ ns). In the wire chambers, the high voltage draws the ionization electrons to the wire in a slow drift process ( $\sim\mu$ s). The drift time is proportional to the closest distance between the muon track and the wire, allowing for track reconstruction. The measured drift time for each wire is the time difference between when the scintillator fires and when the drift electrons reach the wire.

The scintillator consists of three large rectangular panels (3.5 m x 70 cm x 5 cm) which cover the active region of the detector. Each scintillator panel is observed at either end by multiple PMTs run in parallel. The signals from the PMTs were sent to a CAMAC Analog to Digital Converter (ADC) and a discriminator. If both ends of a panel fire in coincidence, a start signal is sent to the wire readout modules, and the ADC modules record the pulse-height of each PMT.

Each wire chamber is monitored by an individual Front-End Electronics (FEE) card which outputs an ECL signal if a pulse is detected on the wire. The ECL signal is sent to a CAMAC Time to Digital Converter (TDC) for readout. The TDC cards have 1024 bits of output with 4 ns per bit, giving them a time window of 4.1  $\mu$ s. The FEE cards are very sensitive, and can easily be triggered by noise back-propagating along the readout cables. The CAMAC readout is very noisy, which means that when the readout cables are plugged directly into the TDC, the signal is swamped by noise. In order to minimize this problem, the readout cables were sent through an ECL-NIM-ECL converter which filtered out the majority of the noise. Even with this work-around, noise problems were still present. These problems were due to electrical pickup, and thus very geometry dependent. To fix these remaining problems, FEE cards were traded out and cables moved until the noise was brought to a minimum.

At SNO, the EMuS system is deployed in the ALIMAC region of the detector, which is due west of the neck of the detector in PSUP coordinates (see figure ??). Due to space and solid-angle considerations, the planes are inclined at a  $55^\circ$  angle with the lower end to the west. A survey was performed to find the absolute position of each of the wires with respect to the SNO detector [38]. The survey was able to

locate all of the wires to within 0.67 cm. The dominant sources of uncertainty are summarized in table 5.1. The largest uncertainties come from the method used to locate the detector with respect to SNO. The master survey point used to locate the SNO detector was not visible from the EMuS system. However points on the detector were surveyed when SNO was installed [39], and these points were measured by the EMuS survey and used as reference points. However the two surveys disagreed slightly on the distance between the reference points, introducing a 0.53 cm uncertainty on the X-Y coordinates of the EMuS detector. In addition, the reference point used for the Z-coordinate of the detector was only known to  $\pm 1/8$  in, introducing a 0.32 cm uncertainty. Other uncertainties on the locations of the wires included uncertainties on the floor level, the placement of the wires within the modules, the spacing between wires, and the gaps between the modules. These uncertainties do not apply equally to all wires, and have a maximum value of 0.30 cm.

## 5.1 Time to Radius Conversion

When a muon passes through a wire chamber, it deposits energy [10]. While most of that energy goes into heating the gas and metal, some of it ionizes gas atoms, creating electron-ion pairs. Since we have applied a high voltage across the wire chamber, the electrons will be accelerated towards the wire, while the ions will travel towards the walls. As the electrons move through the gas, they will random walk toward the wire with a characteristic drift velocity [40]. This drift velocity means that electrons generated close to the wire will get to the wire earlier than ones that were generated

SNO X-Y Coordinate	0.53 cm
SNO Z Coordinate	0.32 cm
Floor Level <sup>1</sup>	0.17 cm
Wire Placement	0.08 cm
Wire Spacing <sup>1</sup>	0.18 cm
Gaps Between Modules <sup>1</sup>	0.14 cm
Time to Radius Conversion	0.28 cm
Overall	0.74 cm

Table 5.1: Uncertainties associated with wire positioning.

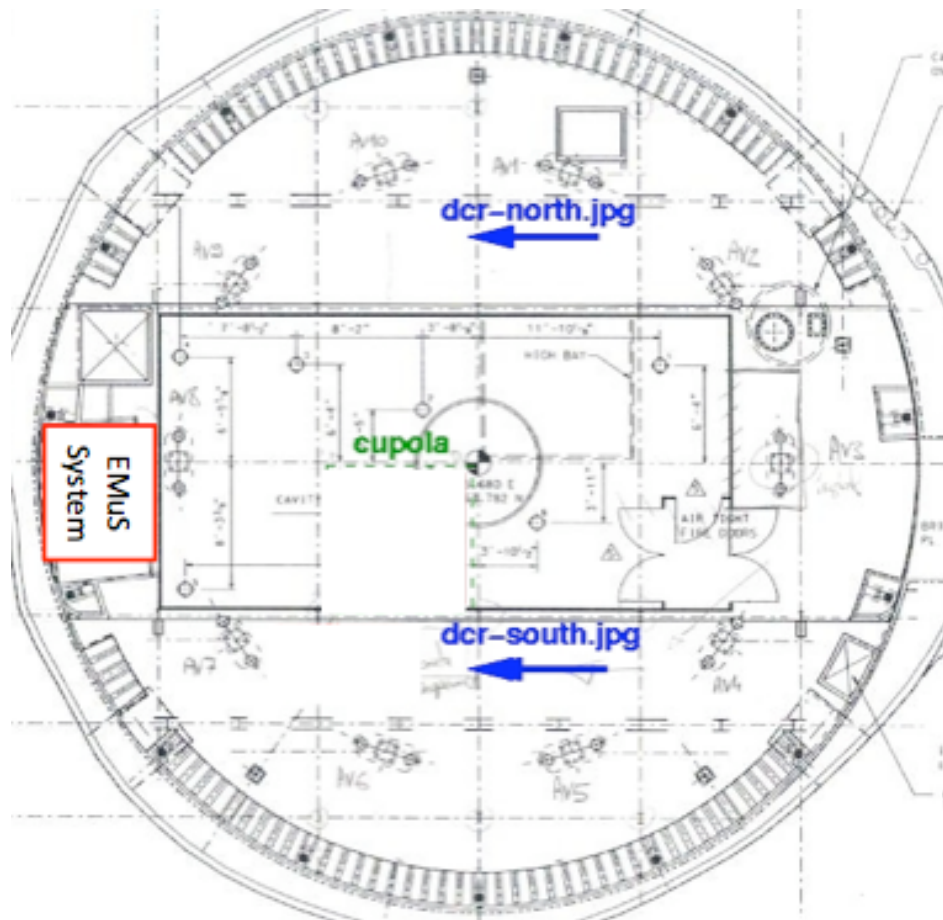


Figure 5-2: Location of the EMuS system on the SNO deck.

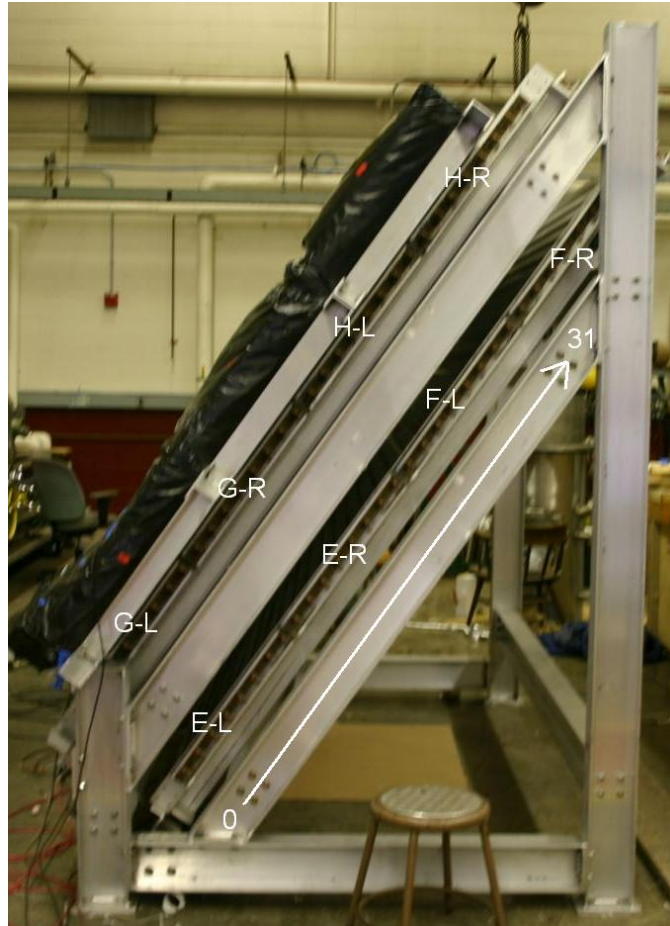


Figure 5-3: A view of the side of the EMuS setup. The numbers indicate the order of channels.



Figure 5-4: A view of the back side of the EMuS setup. The numbers indicate the order of channels.

farther away. Once the electrons get close to the wire, they gather enough energy between collisions to ionize other gas atoms, thus creating an avalanche of electron-ion pairs. This avalanche provides the gain that allows a one-electron signal to be seen, and should be roughly the same for electrons generated anywhere in the chamber. Thus while the output pulse from a wire should be essentially the same wherever the muon goes, the timing of the start of the pulse indicates the radius of closest approach of the muon. If the conversion function between timing and radius ( $r(t)$ ) is known, the tracking resolution of the detector can be smaller than the size of the wire chambers.

The Garfield gas simulation [41] was used to generate expected  $r(t)$  curves as a function of gas pressure and applied voltage. The code was not able to perfectly model the shape of the wire chambers so two similar geometries were used to check the effects of this imperfect modeling: a circle with radius 3.75 cm, and a regular octagon with a longest radius of 4.06 cm. Simulated electrons were generated at 10 points along the longest radius, and the mean drift time for each point was calculated. Figure 5-5 shows that the that the two  $r(t)$  curves agree to within 2%. A parabolic fit to this data is accurate to 5%.

In order to directly measure the  $r(t)$  curve, the EMuS system was run on the surface at Bates Laboratory. Tracks were selected that pass through two adjacent chambers on two parallel planes. Since the channel numbers are known, an estimate of the angle of the muon trajectory can be calculated. Once the angle is known, the radii of closest approach are related as:

$$R_1 + R_2 = D \cos \theta \tag{5.1}$$

First, a series of data cleaning cuts are applied to remove hit pairs that are obviously noise: The sum of the hit times are plotted against their difference for each angle (see Figure 5-6). Random coincidences form an upside-down triangle, while paired hits form a parabola. For each angle, pairs of events with a very low or very high sum of times were cut. Then a trial  $r(t)$  function ( $\rho(t) = at^2 + b$ ) is used to

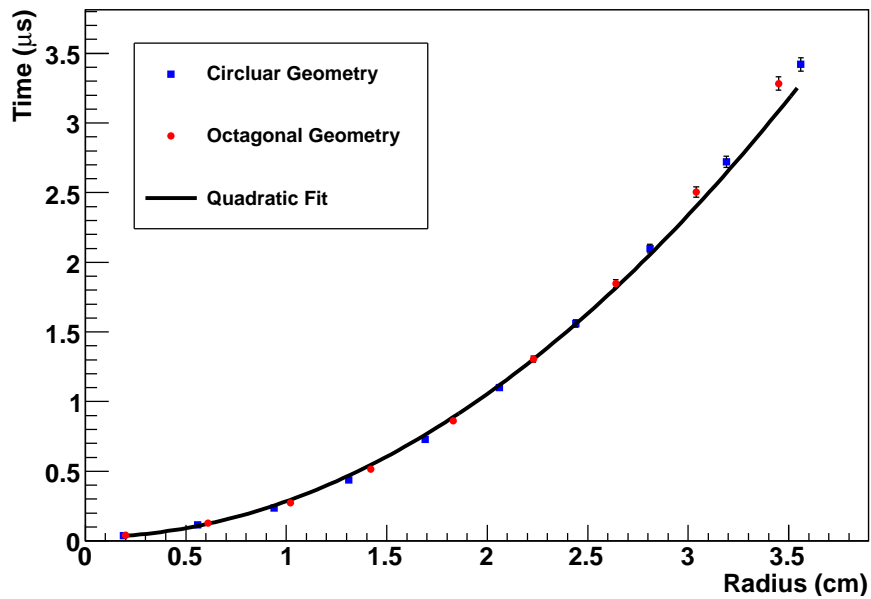


Figure 5-5: Drift time as a function of starting radius for simulated electrons. The quadratic fit is accurate to 5% at the maximum simulated radius.

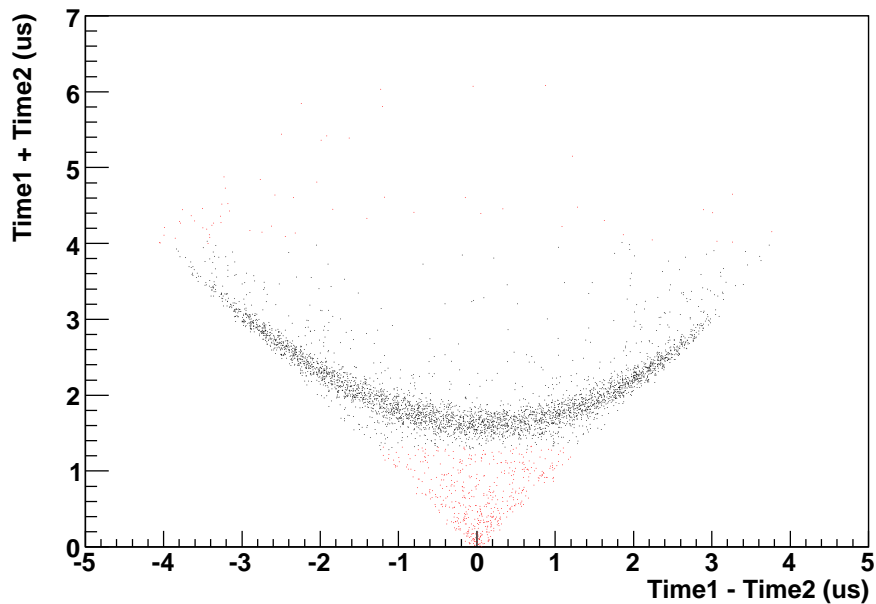


Figure 5-6: Timing relationships between adjacent tubes with a muon angle of  $60^\circ$ . Correlated events should fall on a parabola. The red points are random coincidences and were cut out of the analysis.

estimate  $R_2$  as a function of the time from the other chamber:

$$R'_2 = D \cos \theta - \rho(t_1) \quad (5.2)$$

A least-squares parameter  $B$  is constructed from these variables:

$$B = (\rho(t_2) - R'_2)^2 \quad (5.3)$$

$B$  is then minimized with respect to  $a$  and  $b$ , and the resulting  $r(t)$  curve is shown in Figure 5-7. This fit seems to work nicely since slices in time show a gaussian shape. The maximum width of these slices is 0.243 cm, which is taken as the uncertainty of the  $r(t)$  conversion at the surface. The width of those gaussians is likely determined by the inaccuracies in the estimates of  $\theta$ . A more in depth analysis using 3-tube hits could likely give a smaller width. However, the current width gives a position uncertainty that is half as small as the uncertainty from the survey. Thus it was not investigated any further.

The fit also gives a negative time offset of 72.3 ns which is likely due to electronic delays. The PMT trigger signal has to go through a series of logic units before it gets to the TDC modules, which could easily delay it by this much. This problem could be fixed by adding more cable between the FEE cards and the TDC modules, however this was not done due to time and space concerns. In the end, this delay means that a muon that passes within 5 mm of the wire may not trigger a hit. This inefficiency means that 35% of events which should have hit 4 chambers will only hit 3, while 36% of events which should hit 3 chambers will hit 2 or fewer, and thus be excluded from the analysis. While this will decrease the number of reconstructed events, it should not significantly change the reconstruction accuracy.

Figure 5-7 shows that the reconstructed  $r(t)$  curve and the Garfield prediction are consistent for the running conditions at the surface. However running conditions were slightly different underground. Garfield simulations were used to estimate the magnitude of that change. The Garfield curves for underground and surface conditions were fit to parabolas ( $t = dr^2$ ) and the ratio of  $d$ -parameters taken. The extracted

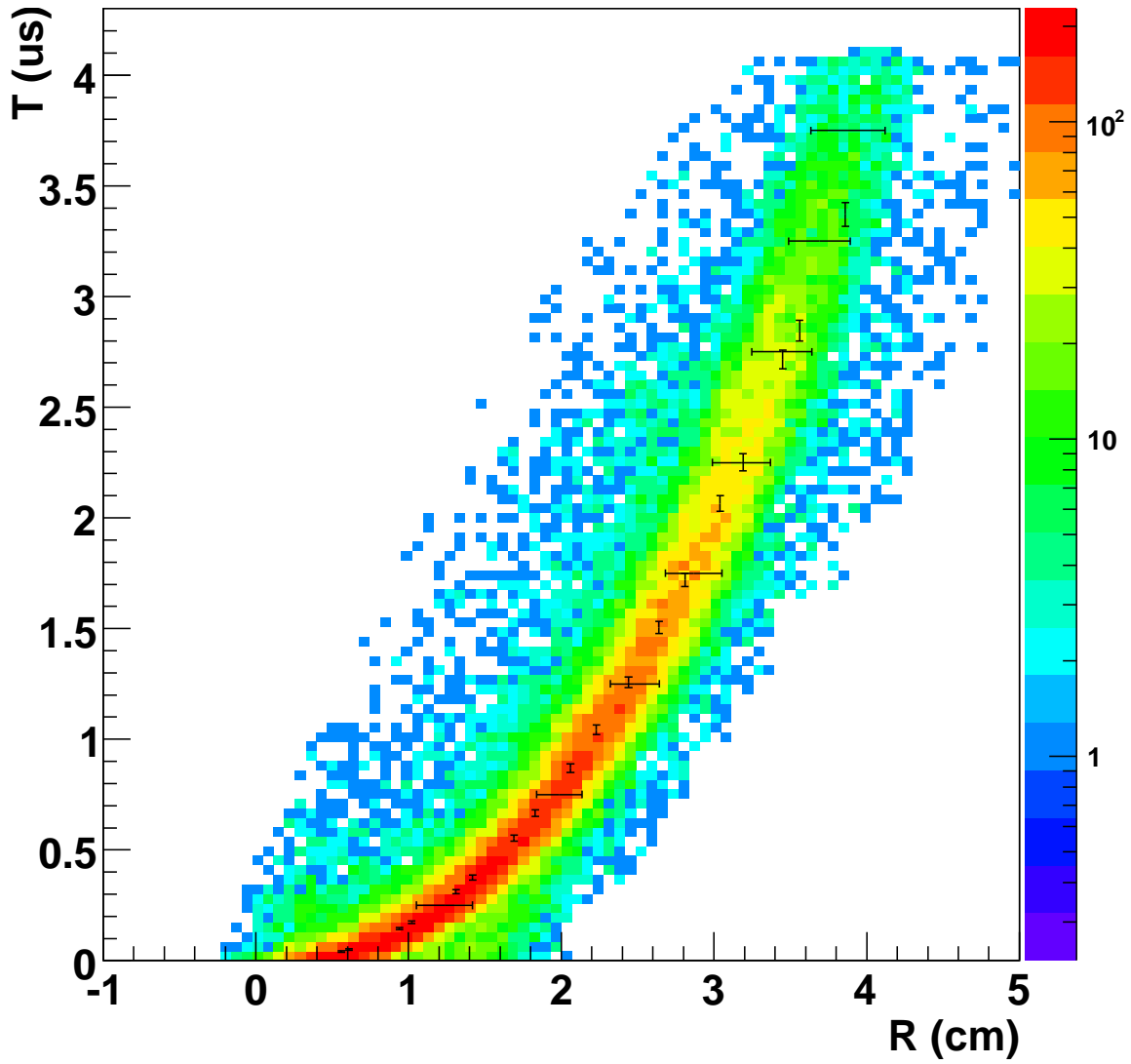


Figure 5-7: Drift time as a function of radius for data taken on the surface of the earth. The color axis indicates the number of events reconstructing with the given radius and time. The horizontal error bars are gaussian fits to slices in time. The vertical error bars are Garfield simulations of the drift time.

$\rho(t)$  curve was scaled by this ratio, yielding:

$$\rho(t) = 1.92\sqrt{t(\mu s) + 0.072} \pm 0.28 \text{ cm} \quad (5.4)$$

## 5.2 Data Selection

In order to find events that went through both SNO and the EMuS system, a number of data quality checks were made. First, the trigger rate for each channel was analyzed. It was found that three channels never fired, while another three channels fired almost continuously. These channels were disconnected half-way through the experiment because they were not providing useful data, and were removed from the analysis. In addition, it was found that some channels had multiple hits in a single event. In those cases the hit with the lowest time was assumed to correspond to the muon.

Multi-channel events are constructed by combining the hit information from the 4 wire planes and the PMTs. When the computer read out the CAMAC crate, it assigned a time to each module based on when it was read out. It took an average of 100  $\mu s$  to read out each module, so an event could consist of five blocks of data with event times spanning 500  $\mu s$ . On the surface, the event builder handled this feature by gathering together any events in a 1 ms window, and assigning them the time of the earliest event. Underground, where the muon rate is much lower, this window was expanded to 1 s.

In order to qualify as a muon hit, an event had to pass a number of cuts. First, wires on three or four of the planes had to fire. Second, the event had to have fewer than 30 wires fire. An event with more than 30 hit wires is most likely caused by electrical pickup, and would be difficult to reconstruct even if it was caused by a muon. Third, the event had to take place in a quiet run. The EMuS system acquired data during all types of SNO runs, including runs when sources were being moved.

Some of these runs are extremely noisy, with multiple wires hit for every trigger. If the average number of hit wires per event in a run was greater than one, all events in that run were cut. These cuts left 62 EMuS events.

To correlate these event with the SNO detector, all of the events were examined by hand with the XSnoED event viewer. Of the 62 candidate events, 32 corresponded to a muon track in SNO, while 16 corresponded to an event where a muon passed next to SNO and was seen by the outward looking tubes. Of the 32 muon tracks, 30 were reconstructed by the SNO muon fitter (FTI), and will be analyzed. The EMuS system ran for 94.6 days of livetime, giving a rate of 0.32 reconstructed coincident events per day.

### 5.3 Reconstruction

A Monte Carlo based method is used to reconstruct events in the EMuS system. For each event, random tracks are generated and the likelihood of each track is calculated. The most likely tracks are then used to estimate the agreement between SNO and the EMuS system for each event. Finally, the levels of agreement from all 30 tracks are used to estimate the accuracy of the FTI muon fitter.

To generate random tracks, the FTI track corresponding to each EMuS event is used as a seed, and a coordinate system is developed based on that track. The origin of the coordinate system is the point on the track closest to the center of SNO. The z direction is the direction of the track. The x and y directions are perpendicular to the z direction and to each other. The track is then randomly varied by: rotating the track direction about the x axis, rotating the new track direction about the z axis, and shifting the closest point in the x and y directions. The random tracks generated in this way cover all possible tracks close to the original track.

Once a random track has been produced, its likelihood must be calculated. The likelihood algorithm is based on calculating the closest distance between the line that defines the muon track and each of the wires that fired (the impact parameter  $b$ ). In order to calculate  $b$ , four vectors must be known:  $\vec{\mu}_p$ , a point on the muon track,  $\hat{\mu}_d$ ,

a unit vector in the direction of the muon track,  $\vec{w}_p$ , a point on the wire, and  $\hat{w}_d$ , the direction of the wire:

$$b = (\vec{w}_p - \vec{\mu}_p) \cdot \frac{\hat{w}_d \times \hat{\mu}_d}{|\hat{w}_d \times \hat{\mu}_d|} \quad (5.5)$$

The negative log likelihood value (hereafter referred to as the likelihood) for each random track is calculated as:

$$L = \sum_{\text{wires } i} \frac{[b_i - \rho(t_i)]^2}{\sigma^2} \quad (5.6)$$

where  $\rho(t_i)$  is the expected radius given the TDC time recorded for the wire and  $\sigma$  is the wire position uncertainty. Wires with a likelihood greater than 25 have their likelihood artificially reduced to prevent noise hits from biasing the likelihood. Each track is given a weight:

$$w = e^{-(L-L_{min})} \quad (5.7)$$

where  $L_{min}$  is the smallest likelihood value calculated for any track in that event. In figure 5-8, the locations of the best fit tracks are projected onto the two most important parameters for the FTI fitter: the change in impact parameter and the angle between the FTI track direction and the random track direction. In these parameters, the FTI track is at (0,0). The inverted triangle shape is characteristic of all of the events, and is actually the projection of an inverted cone. This occurs because there is a high correlation between changes in angle and changes in impact parameter<sup>1</sup>.

Because this analysis gives a set of possible tracks instead of a single track, an assumption is made that the FTI track has either the correct direction or the correct impact parameter. However if the the angular misreconstruction distribution is large, assuming that the track direction is correct will lead to a large increase in the width of the extracted impact parameter distribution. Figure 5-9 shows that this is the case.

---

<sup>1</sup>It is as if the EMuS system is a dart board, and the random tracks are darts. If the direction of the dart is changed slightly, it can still hit the bull's eye as long as the throwing position is shifted to compensate.

The top two plots show the angular and impact parameter distributions given by comparing the true and reconstructed tracks in the Monte Carlo. The bottom plots show the same distributions if a correlation between angle and impact parameter similar to that expected in the EMuS system is added, and the assumptions of correct impact parameter or direction are used. This simulation is accomplished by changing the original track parameters  $b_i$  and  $\theta_i$  into  $b_{new}$  and  $\theta_{new}$ :

$$\theta_{new} = \left| \theta_i + \frac{b_i \sin(\theta_{rand})}{S |\sin(\theta_{rand})|} \right| \quad (5.8)$$

$$b_{new} = b_i - \theta_i S \sin(\theta_{rand}) \quad (5.9)$$

The constant  $S$  has a value of 22 cm/degree and comes from the fact that the EMuS detector is around 12 m away from the center of the SNO detector. Thus a  $1^\circ$  angular misreconstruction should be indistinguishable from a 22 cm impact parameter misreconstruction.  $\theta_{rand}$  is a random angle introduced because the angular misreconstruction comes from a two-dimensional distribution while the impact parameter distribution is only one-dimensional.

A likelihood fit using two gaussians has been adopted as the main fitting method. The impact parameter misreconstruction distribution is fit to the form:

$$p(x) = A \left( f e^{-\frac{(x-\mu)^2}{2\sigma^2}} + (1-f) e^{-\frac{(x-\mu)^2}{2(m\sigma)^2}} \right) \quad (5.10)$$

where  $A$  is a normalization constant,  $\mu$  is the mean,  $\sigma$  is the width of the first gaussian,  $f$  is the weight fraction of the first gaussian, and  $m$  is the width of the second gaussian divided by the width of the first. The angular misreconstruction distribution is similarly fit to:

$$p(x) = A \theta \left( f e^{-\frac{\theta^2}{2\sigma^2}} + (1-f) e^{-\frac{\theta^2}{2(m\sigma)^2}} \right) \quad (5.11)$$

Figure 5-9 demonstrates that two gaussians reproduce the Monte Carlo distributions well using the standard likelihood fitting method. However this method introduces two extra floating variables. When fitting the low statistics EMuS data,

these extra variables are likely to make the fit unstable. So the  $f$  and  $m$  parameters were fixed based on fits to the Monte Carlo distributions, thus reducing the number of free parameters. For the impact parameter distribution,  $f$  was fixed at 0.988 and  $m$  was fixed at 7. For the angular distribution,  $f$  was fixed at 0.990 and  $m$  was fixed at 4.

Figures 5-10 and 5-11 show the results of applying the two gaussian fit to the EMuS data. The fit angular width is  $0.61^\circ \pm 0.06^\circ$ . This means that the EMuS system has measured an angular misreconstruction distribution that is 50% larger than predicted by SNOMAN. Section 8.3 will estimate the effect of this misreconstruction on the atmospheric neutrino analysis. The fit impact parameter mean is  $4.2 \pm 3.7$  cm, while fit impact parameter width is  $18 \pm 3$  cm. As demonstrated by simulations, the correlation between angular and impact parameter misreconstruction renders the EMuS measurement of impact parameter misreconstruction unreliable at best. In this analysis, the mean of the impact parameter distribution is found to be consistent with zero, while the width is found to be 1.65 times larger than predicted by SNOMAN if correlations are taken into account. It is likely that this is a direct result of the fact that the angular misreconstruction distribution is 1.5 times larger than predicted by SNOMAN.

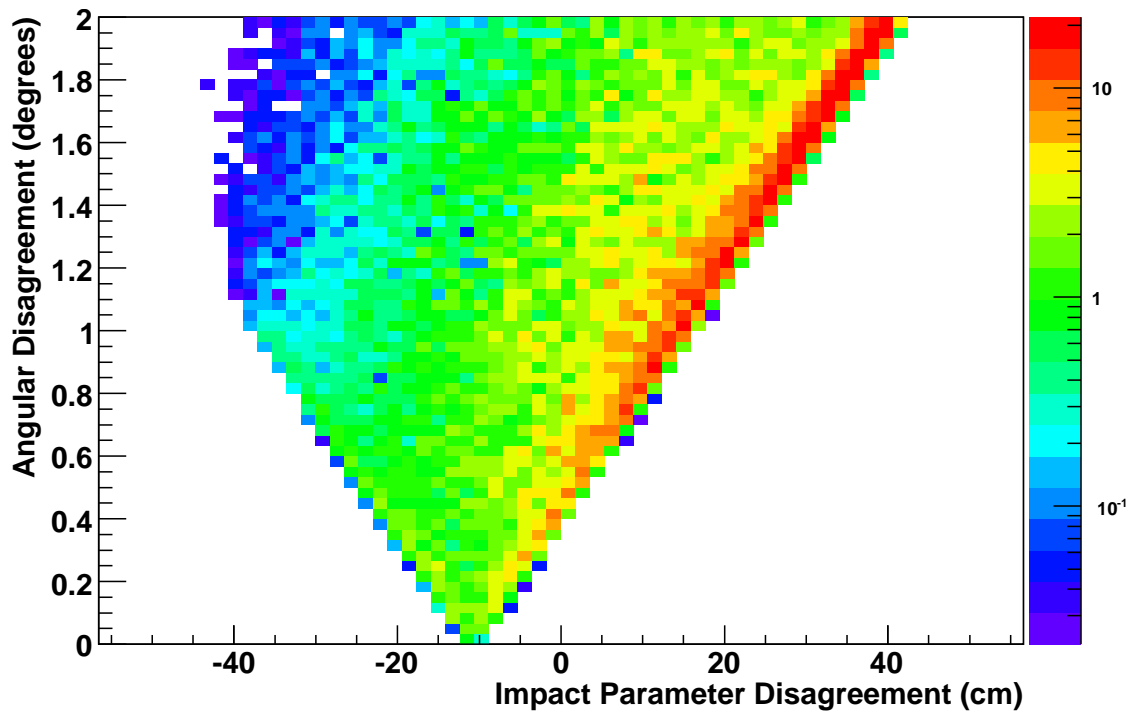


Figure 5-8: Angular disagreement vs impact parameter disagreement between the FTI fitter and the EMuS system for the most likely tracks. The color scale indicates the density of possible tracks weighted by their probability.

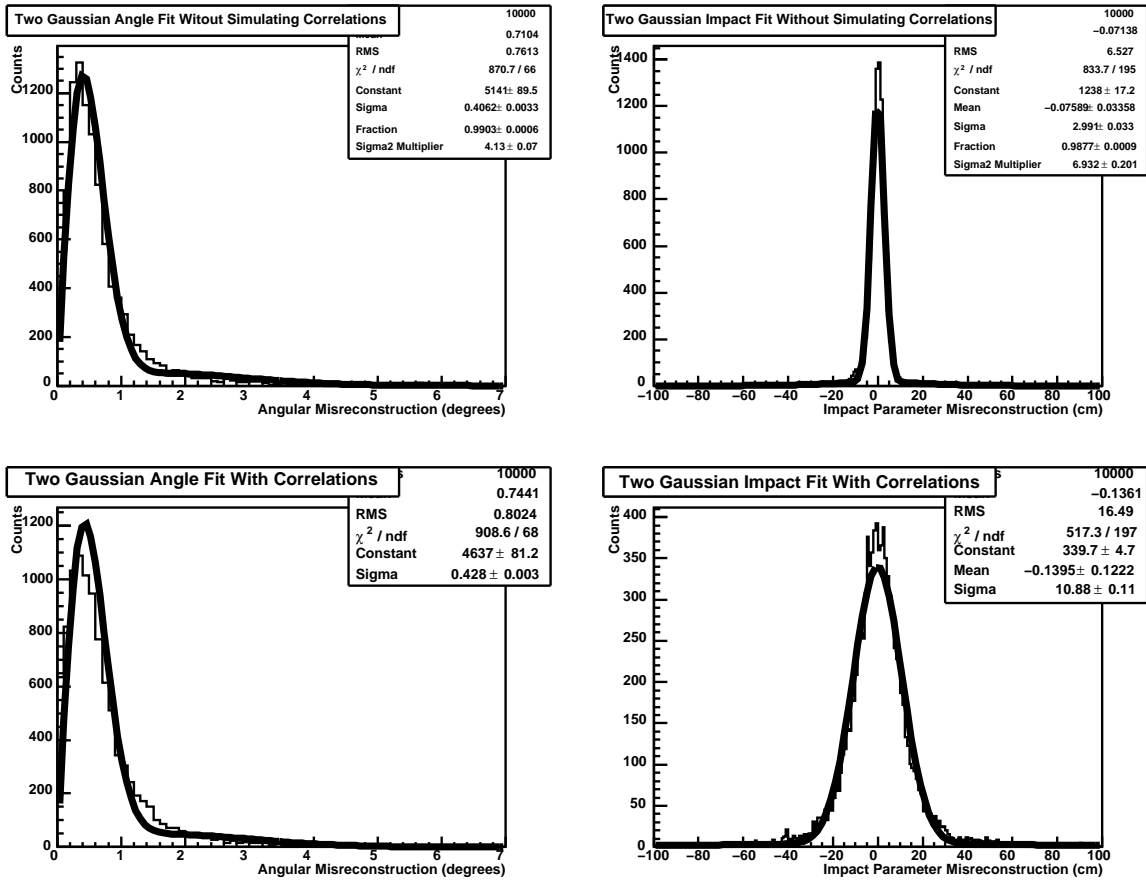


Figure 5-9: Results of fitting the angular and impact parameter distributions using two gaussians and ROOT's likelihood fitting method. The top plots show the results of fitting the distributions directly from SNOMAN Monte Carlo. Based on these fits, the size and relative width of the second gaussian is fixed as described in the text. The bottom plots show the results of using these two gaussian fits on SNOMAN Monte Carlo including the expected correlations due to the EMuS analysis.

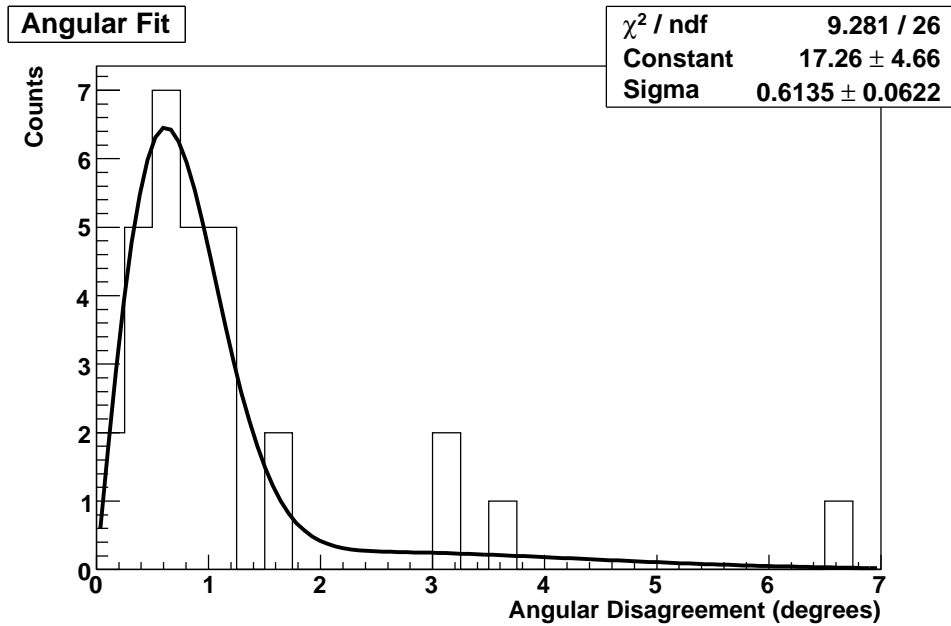


Figure 5-10: Fit to EMuS angular misreconstruction data. The fit width of the main gaussian is  $0.61^\circ \pm 0.06^\circ$ . The second gaussian has a fixed weight fraction of 1.1%, and a fixed width of 4 times that of the main gaussian.

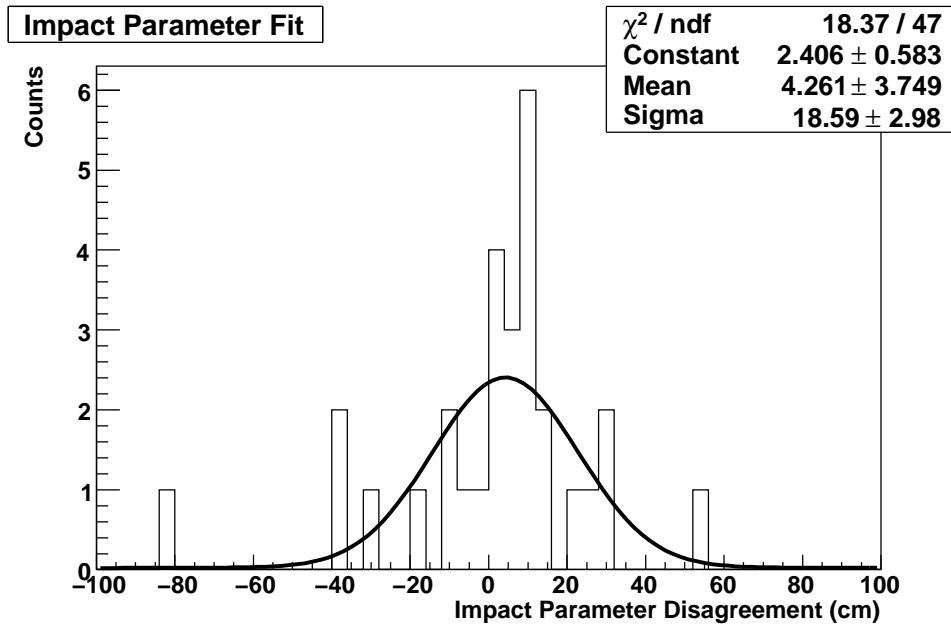


Figure 5-11: Fit to EMuS impact parameter misreconstruction data. The fit mean of the gaussians is  $4.2 \pm 3.7$  cm, while the width of the main gaussian is  $18 \pm 3$  cm. The second gaussian has a fixed weight fraction of 1.12% and a fixed width of 7 times that of the main gaussian.

# Chapter 6

## Analysis

### 6.1 Analysis Overview

The majority of the neutrino-induced muons seen by SNO are produced in the surrounding rock, and are identified as produced by neutrinos due to their direction of travel. When the muons enter the detector from the rock, their production point and original energy are unknown. Thus the oscillation probability cannot be measured as a function of neutrino energy. However, using Monte-Carlo simulations, the rate of through-going muons as a function of their direction can be used to extract the oscillation parameters.

In order to do this, Monte-Carlo neutrinos and muons are generated with the correct livetime and detector conditions assuming no neutrino oscillations. This generates an expected muon flux as a function of zenith angle. For a given set of oscillation parameters, the Monte-Carlo events are re-weighted, producing a different muon flux as a function of zenith angle. The measured number of muons as a function of zenith angle is then compared to these predictions, and a maximum likelihood fit is used to extract the oscillation parameters and overall flux of atmospheric neutrinos.

The beauty of this method is that the detector efficiency is already built into the analysis. For example, the neck of the detector does not have PMTs, making it more difficult to reconstruct muons going straight up. If the reconstruction efficiency drops by 10% for muons going straight up, the resulting deficit of measured muons could be

mistaken for a change in the oscillation parameters. But with this Monte-Carlo based method, the expected number of muons should show the same deficit, removing the confusion.

Although the fitting procedure is relatively easy, creating and validating the Monte-Carlo simulations is much more difficult. If a source of events that look like through-going muons is left out or the Monte-Carlo simulations are significantly different from the real data, the extracted oscillation parameters will be wrong. In addition, the systematic uncertainties associated with the Monte-Carlo simulations must be included in the fits. This section will detail the codes used to generate the Monte-Carlo, the cuts used to isolate a through-going muon sample, the procedures used to ensure data-Monte-Carlo agreement, the methods used to estimate uncertainties, and finally the fitting method itself.

## 6.2 Simulations

The SNO muon group has identified six sources of events that could look like through-going muons:

1. cosmic ray muons
2. through-going neutrino-induced muons
3. stopping muons
4. muon neutrino interactions inside the detector
5. electron neutrino interactions inside the detector
6. instrumental backgrounds (light-based or electronic)

The first five are physics-based and can be simulated. Instrumental backgrounds cannot be simulated, but they often come in bursts of more than four events in 2 seconds. These bursts are used to estimate the amount of noise contamination in section 6.3.3.

The physics-based sources are simulated in three different Monte Carlo routines based on the codes necessary to produce them. The first code simulates primary cosmic ray muons that reach SNO. It includes through-going and stopping muons. The second code simulates electron, muon, and tau neutrino interactions in the surrounding rock with the proper fluxes. Almost all of the events that reach the detector from this simulation are neutrino-induced muons that either pass through the detector or stop in it. The final routine simulates neutrino interactions in the SNO detector and the water shielding surrounding it. All three neutrino types are simulated, producing samples of through-going and stopping muons as well as internal electron and muon neutrino interactions.

### 6.2.1 Cosmic Ray Muon Simulation

This simulation is based on the MUSIC muon propagation code [42]. MUSIC is an event-by-event Monte Carlo that propagates muons through rock in three dimensions. It models the energy loss and direction change from continuous processes such as ionization and multiple scattering as well as from rare stochastic processes such as bremsstrahlung, inelastic scattering, and pair production. MUSIC properly accounts for the energy and angular distributions of cosmic ray muons as well as their expected rate. MUSIC has been extensively validated in other experiments, and its parameterizations are found to be accurate to within 1% for water-equivalent depths of 5-10 km [43]. However uncertainties in the flux of high energy muons and muon-nuclear cross-sections dominate for these high energy muons.

Once a simulated muon reaches the top of the SNO detector, it is passed to the SNOMAN detector Monte Carlo. SNOMAN simulates the propagation of the muon and generates secondary particles and Cherenkov photons. All photons are tracked through the detector until they are absorbed or detected. If a photon is detected, SNOMAN uses run-by-run calibrations to simulate the charge and timing seen by the detector. For muons, SNOMAN simulates all of the dominant processes including: ionization (Bethe-Bloch), multiple scattering, Cherenkov radiation, bremsstrahlung, moller scattering ( $\delta$  rays), pair production, photo-neutron production, deep inelastic

scattering, muon capture, and muon decay.

SNOMAN has been validated intensively at low energies for the solar neutrino analysis [34, 44, 45]. These checks mean that the detector geometry, calibrations, and the Cherenkov radiation routine have been well tested. The muon group has also performed extensive data - Monte Carlo comparisons for cosmic ray muon samples, and good agreement is seen. The specific comparisons are detailed in section 6.3. Good data - Monte Carlo comparisons mean that the dominant processes including ionization, Cherenkov radiation, moller scattering, muon capture, and muon decay are well modeled. The remaining subdominant processes have not been validated.

### 6.2.2 Rock Neutrino Interaction Simulation

This simulation uses the NUANCE V3 neutrino interaction code [46] to generate neutrino-induced muons which enter the SNO detector. The electron and muon neutrino fluxes as a function of detector zenith angle from the BARTOL group [21] are used as an input to NUANCE. In addition, a tau neutrino flux equal to that of the muon neutrinos is used in order to correct for tau neutrino appearance. NUANCE uses this flux to generate neutrino interactions in the rock surrounding SNO. It includes cross-sections for many neutrino interaction modes including quasi-elastic, resonance, deep-inelastic, coherent, diffractive, and elastic scattering. The muon group has verified these cross-sections and adjusted their parameters to match the standard calculations used by Super Kamiokande and K2K.

The largest cross-section for neutrino-induced muons comes from deep-inelastic scattering. The uncertainty on this process is well-constrained by high-energy neutrino beamline experiments to be  $\pm 3\%$  [47, 48, 49] which contributes a 2.3% uncertainty to the flux of atmospheric neutrinos. Another important reaction is one in which a single pion is resonantly produced. This is incorporated in NUANCE as a modified Rein and Sehgal model [50]. The uncertainties on this cross-section are around 20%, however this mode is not as dominant, so it only gives a 2.1% uncertainty on the flux. The other major process that produces muons is neutrino quasi-elastic scattering. This process is modeled according to the Llewellyn Smith Formalism [51],

with the Smith and Moniz fermi gas model [52] used for nuclear effects. Uncertainties associated with this cross-section produce a 0.8% uncertainty on the atmospheric neutrino flux. In addition recent measurements by K2K [53] and MiniBooNE [54] give a higher value of the axial mass than previously measured. While this is likely due to outdated nuclear models, this uncertainty on the axial mass is included as its own systematic. This gives an uncertainty on the flux of 1.2%.

If a muon is produced in the final state, NUANCE propagates the muon to the SNO detector using the muon propagation algorithm PROPMU [55]. Although this algorithm is not as well-developed as MUSIC, it is incorporated into NUANCE and agrees with MUSIC to within a few percent. Once the muon reaches the edge of the SNO cavity, it is passed to SNOMAN for final simulation.

### 6.2.3 Internal Neutrino Interaction Simulation

This simulation also uses NUANCE V3, but skips the muon propagation step. In this simulation, all of the final state particles from the NUANCE simulation are passed to SNOMAN. Since SNOMAN simulates both the detector and the water shield, this simulation will include through-going neutrino-induced muons as well as neutrino interactions inside of the detector volume.

## 6.3 Analysis Cuts

The analysis cuts are designed to remove all of the muon-like events that are not through-going muons. While in principle it is possible to cut on the minimum likelihood from the FTI fitter, it was found that the likelihood was highly correlated with the number of PMT hits, making a likelihood cut difficult. Instead a set of data quality cuts were developed to differentiate through-going muon events. The cuts can be generally divided into low-level cuts, which mostly remove instrumental background events, and high-level cuts, which use the track fit parameters to remove stopping muons and neutrino interactions inside the detector. These cuts are summarized in table 6.1 and are explained in detail in the following section.

Level	Cut	Value
Low	Event Reconstruction	NHit > 250
		No Retrigger
	Bursts	< 4 Events in 2 Seconds
	Neck Tubes	< 4 Fire
	NCD Run Boundary	PMTs and NCDs Must Be Online
	Calibrated PMTs	> 500
	Raw $Q_{RMS}$	> 4.5 GSU
Raw $T_{RMS}$	< 38 ns	
High	Impact Parameter	< 830 cm
	Fit Number of Photoelectrons	> 2000 pe
	dE/dx	> 200 MeV/cm
	Cherenkov Cone In-time Ratio	> 0.85
	Fraction of Cherenkov Cone PMTs That Fire	> 0.7
	Linear Discriminant	> 0.6

Table 6.1: The analysis cuts used to isolate through-going muon events from instrumental backgrounds, stopping muons, and internal neutrino interactions

### 6.3.1 Low Level Cuts

#### Fitter Event Selection

The FTI fitter requires a significant amount of computing power to find the best muon track. Thus it makes sense not to run the fitter on events which are obviously not muons. Muon events are expected to produce a lot of light, so only events with more than 250 hit PMTs are sent through the muon fitter. In addition, due to PMT effects and reflected light, many events produce secondary events soon after the original event. These events are almost always detector noise, and so all events within  $5 \mu\text{s}$  after another event are cut by the retrigger cut, and are not reconstructed with the FTI fitter.

#### Burst Cut

Many detector noise events including flashing PMTs, bursting bubbles, and electronic pickup are known to come in bursts of a few events per second. If four or more events passing the retrigger cut with greater than 250 hit PMTs occur within 2 seconds, all

of the events are classified as burst events and are removed from the analysis. Since through-going muon events should not occur in bursts, the data tagged by the burst cuts gives a sample of noise events which can be used to test the discriminating power of the rest of the cuts. Tests using this sample will be detailed in section 6.3.3.

### **Neck Tube Cut**

Another source of detector noise is light generated in or leaking through the glove box on top of the detector. The glove box is where calibration sources are deployed, and is at the top of the neck of the detector. Any light generated in the glove box is not visible to any PMTs except those at the bottom of the detector. So these events are likely to look like a ring of light on the bottom of the detector, which could be reconstructed as a downward muon. In order to veto these events, four small PMTs were installed at the top of the neck. If all four PMTs fire in coincidence with a detector event, the event is cut out of the muon analysis.

### **NCD Run Boundary Cut**

In the NCD phase, a cut was implemented to make sure that both the PMTs and the Neutral Current Detectors were online before physics data was taken. Any event that occurs before the first or after the last NCD event in a run is removed. Although the NCDs are not used in the atmospheric neutrino analysis, this cut only removes 0.07% of the NCD phase livetime and is more conservative.

### **Calibrated PMTs**

By studying Monte Carlo simulations of cosmic ray muons and through-going neutrino-induced muons, it was found that no muons fired less than 500 calibrated PMTs<sup>2</sup>. Thus a cut is placed that a muon must have greater than 500 calibrated PMTs.

---

<sup>2</sup>A calibrated PMT is one which was online and had good charge and timing calibration constants according to the SNO database.

## Raw $Q_{RMS}$

Muons deposit a large amount of light in the PMTs closest to their exit point and much less light away from the Cherenkov cone. Since light is converted into charge in the PMTs, this should show up as a large spread in the amount of charge the PMTs see. Thus a cut was designed to look for the Root Mean Squared (RMS) of the charge seen on the PMTs. Using simulations, it was decided that  $Q_{RMS}$  should be greater than 4.5 gain scaled units<sup>3</sup>.

## Raw $T_{RMS}$

Some instrumental background events were found to have very flat PMT hit time distributions, which led to a cut on the RMS of the PMT hit times with respect to the data acquisition trigger. By comparing burst data and simulations, it was found that a cut of  $T_{RMS} < 38$  ns removed a significant fraction of the noise events.

## 6.3.2 High Level Cuts

### Impact Parameter

The impact parameter of a muon track is the distance of closest approach of the muon to the center of the detector. Thus a cut on the impact parameter defines the fiducial area of the detector. Originally the fiducial area was going to be the heavy water volume inside of the Acrylic Vessel for an impact parameter cut of 600 cm. However it was found that SNOMAN simulates muons very well out to large radii, and the impact parameter cut was extended out to 830 cm out of a possible 850 cm. Past 830 cm, there is very little light, and the light concentrators on the PMTs make the hit pattern very different from that of standard muons.

### Fit Number of Photoelectrons

The FTI muon fitter fits for the expected number of detected photons (FNP) given a standard detector as described in section 4. This calibrates out offline PMTs and

---

<sup>3</sup>A gain scaled unit is the calibrated charge expected for a single photoelectron for each PMT.

the neck of the detector. Based on simulations, it was found that no muons with an impact parameter less than 830 cm had FNP > 2000.

## **dE/dx**

Because muons are minimum ionizing particles, they should produce an amount of light proportional to their track length in the detector. Muons can also produce delta-rays which produce their own Cherenkov radiation, so it is possible for a muon to produce more light than the minimum. A procedure was implemented to cut out events that do not produce enough light for their track length. This should help remove stopping muons, internal neutrino interactions, and muons that are misreconstructed to smaller impact parameters.

This cut was designed to cut out values of deposited energy divided by track length that were too small. However it was found that this ratio is dependent on the impact parameter in a non-trivial way. So this dependence was factored out using simulations. In particular, the fit number of photoelectrons (FNP) divided by path length ( $l$ ) was plotted against impact parameter squared ( $b^2$ ) for a sample of simulated muons with minimum ionizing energies (simulated dE/dx between 220 and 230 MeV/m). This was then fit to two parabolas, one in the heavy water region, and one in the light water region. An estimate of dE/dx was then constructed as:

$$\frac{dE}{dx} = 230 \frac{\text{FNP}/l}{P(b^2)} \quad (6.1)$$

where  $P(b^2)$  is the result of the fit. Due to changes in the detector optics over time, this procedure was done over 6 time regions, 2 during the D<sub>2</sub>O phase, 3 during the salt phase, and 1 for the NCD phase. It was found that the fit for the NCD phase was based on old simulations and had to be updated. Once this was done, the distribution of dE/dx agreed well between phases. With this calibrated estimate of dE/dx, a simulation-based cut was placed at dE/dx > 200.

## **Cherenkov Cone In-time Ratio**

The best way to distinguish a Cherenkov cone from a circular instrumental background event is to look at the timing of each of the detector hits. In the FTI fitter, an estimate is made for the time that each PMT should fire, and the difference between the real time and the estimated time is calculated as the time residual (see section 4). Unfortunately, the distribution of time residuals was found to differ slightly between data and Monte Carlo, making the time residuals a poor choice for a precise analysis cut. However another cut was defined which is able to compensate for these differences and provide a precise cut for removing instrumental backgrounds.

In this cut, only PMTs inside of the Cherenkov cone are considered. The number of PMTs with time residuals less than 5 ns are divided by the total number of PMTs that fired. Isotropic noise events should have a different timing profile than Cherenkov radiation, and thus many of the PMTs should fail this cut. For real muon events, this ratio should be close to 1, while for isotropic noise events, it can be much smaller. Because 5 ns is larger than the shift between data and Monte Carlo, this cut works for both. Based on simulations, the cut was set at  $\text{CITR} > 0.85$ .

## **Fraction of PMTs in the Cherenkov Cone That Fire**

Through-going muons produce a tremendous number of Cherenkov photons which cause almost every PMT within the Cherenkov cone to fire. Stopping muons and neutrino-induced muons do not travel the entire length of the detector, and thus should not fill in the entire Cherenkov cone. Thus the fraction of PMTs in the Cherenkov cone that fire (the RICH parameter) is a powerful tool for rejecting stopped muons, internal neutrino interactions, and instrumental backgrounds. This parameter works well for central muon events, but it was found that the light concentrators reduced this ratio for events at large impact parameters. In order to fix this, PMTs illuminated by the first and last 50 cm of the track are excluded from the calculation. Based on simulations, a cut is placed that this trimmed RICH parameter (TRICH) must be greater than 0.7.

## Linear Discriminant

In order to check that the above cuts were effective, all of the events in the D<sub>2</sub>O phase were scanned by hand using the XSNOED event viewer. It was found that the vast majority of the events were through-going muons, but that a small number of internal neutrino interactions and instrumental events such as bubbles and flashing PMTs had made it through the cuts. These events had abnormally large PMT time residuals which are captured by the RMS of the time residuals (CRMS). It was also found that the large values of CRMS were correlated with the Cherenkov cone in-time ratio (CITR). Using that information, a linear discriminant created:  $D = 3.1 - CITR - CRMS$ . Events with D near zero have are likely to be instrumental backgrounds, while events with D near one are likely to be through-going muons. Based on simulations, a cut of  $D > 0.6$  was chosen.

### 6.3.3 Phase Stability of Cut Variables

Figures 6-1, 6-2, and 6-3 show the normalized distributions of the cut variables in each phase for neutrino-induced muon simulations, cosmic ray muon simulations, and real data respectively. In each figure, the distribution of the cut variable has been drawn with all other cuts applied. While the distributions change from phase to phase, near the cut values, the distributions are very stable between phases. Based on these plots, it is reasonable to use the same cuts for all three phases. Tables 6.2 and 6.3 also demonstrate that the cuts are stable between phases by looking at the efficiencies of the cuts across phases. Table 6.3 demonstrates that the cuts do an excellent job of removing internal neutrino interactions and instrumental backgrounds flagged by the burst cut. In fact, only 3 events from the burst cut sample made it through the cuts, and these appear consistent with cosmic ray muons coincident with an instrumental burst.

Table 6.2 shows that the total efficiency<sup>4</sup> of the cuts on simulated cosmic ray

---

<sup>4</sup>The efficiency is defined as the number of through-going muons with simulated impact parameter less than 830 cm that pass the cuts divided by the total number of through-going muons with simulated impact parameter less than 830 cm.

Cut	Cosmic Rays			Neutrino-Induced Muons		
	D <sub>2</sub> O %	Salt %	NCD %	D <sub>2</sub> O %	Salt %	NCD %
Calibrated PMTs	100.0	100.0	100.0	100.0	100.0	100.0
Raw $Q_{RMS}$	100.0	100.0	100.0	99.9	99.8	99.8
Raw $T_{RMS}$	100.0	100.0	100.0	99.9	99.8	99.8
Impact Parameter	99.4	99.4	99.5	99.1	99.2	99.1
FNP	99.4	99.4	99.5	99.1	99.2	99.1
dE/dx	99.4	99.2	99.3	96.9	96.4	95.3
CITR	99.4	99.2	99.3	96.9	96.4	95.3
TRICH	99.3	99.2	99.3	96.7	96.3	95.2
Linear Discriminant	99.0	98.8	99.1	96.5	96.0	95.1

Table 6.2: Cumulative cut efficiencies for through going muon simulations. Only muons with a simulated impact parameter less than 830 cm are included in the calculation.

muons is stable at 99%, while the efficiency for simulated neutrino-induced muons is relatively stable at around 96%. The efficiencies are not the same for these two types of through-going muons because their energies are different. This shows up in the dE/dx estimate. The neutrino-induced muon sample has lower energies, and thus a larger portion of the muons are close to stopping. These sometimes produce a low estimate of dE/dx, giving the dE/dx estimate a longer tail at low values. The dE/dx cut was based on the cosmic ray muon simulation, and so this longer tail is cut by the dE/dx cut. While it would be nice to move this cut to a lower value, it was approved by the collaboration before this feature was found, and will not be changed. This is reasonable because the loss of efficiency is very small.

### 6.3.4 Data - Monte Carlo Agreement of Cut Variables

Figure 6-4 shows the normalized cut variable distributions for the cosmic ray muon simulations and the real data. Since the real data is dominated by the cosmic ray muons, this is the best data - Monte Carlo comparison. Most of the variables show good agreement, but a few such as  $Q_{RMS}$  and the Linear Discriminant demonstrate shifts between the two distributions. In order to measure these shifts, the simulated distributions were shifted until they lined up with the data distributions. The agree-

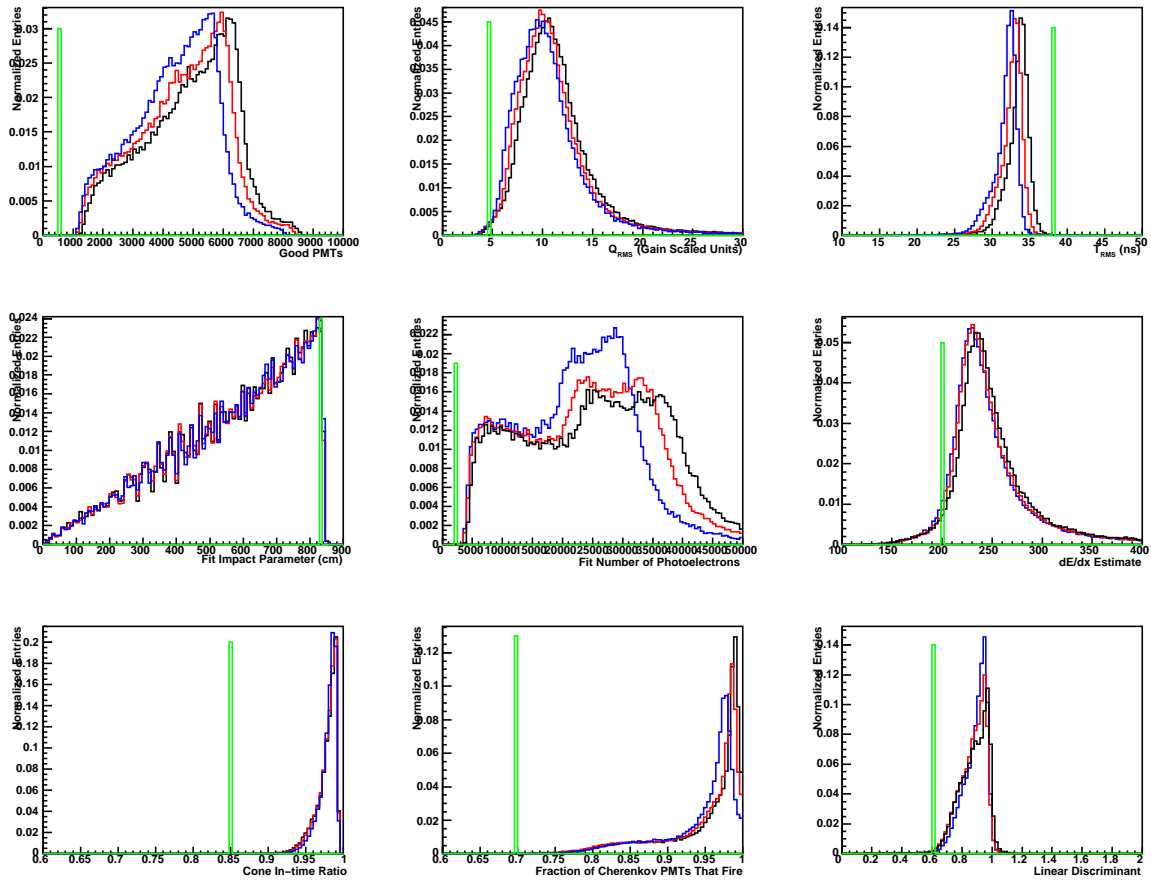


Figure 6-1: Phase stability of cut variables for simulated neutrino-induced muons. The black histograms are for D<sub>2</sub>O, red for salt, blue for NCD, and the cut values are represented by the green lines. While some of the distributions change shape between phases, near the cut values, all variables are stable.

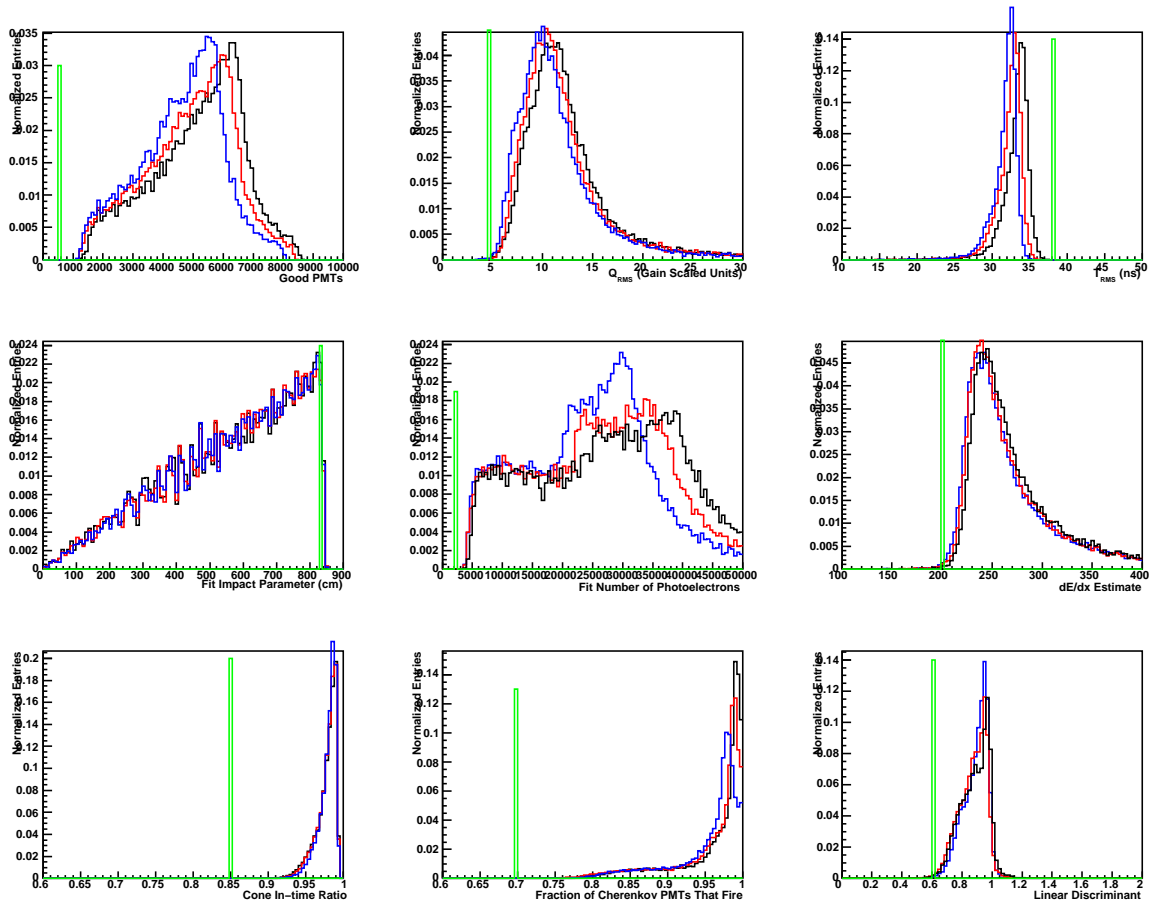


Figure 6-2: Phase stability of cut variables for simulated cosmic ray muons. The black histograms are for D<sub>2</sub>O, red for salt, blue for NCD, and the cut values are represented by the green lines.

Cut	Internal Neutrino Interaction MC			Burst Data		
	D <sub>2</sub> O %	Salt %	NCD %	D <sub>2</sub> O %	Salt %	NCD %
Calibrated PMTs	64.8	66.5	67.3	30.28	11.24	32.58
Raw $Q_{RMS}$	29.2	29.2	28.6	1.83	0.79	0.40
Raw $T_{RMS}$	21.6	22.5	22.7	1.14	0.36	0.14
Impact Parameter	16.7	17.7	17.9	1.10	0.36	0.14
FNPF	15.2	15.7	15.7	1.09	0.23	0.05
dE/dx	7.0	7.1	6.7	0.04	0.11	0.02
CITR	4.1	4.1	4.0	0.03	0.00	0.02
TRICH	4.0	4.0	4.0	0.03	0.00	0.02
Linear Discriminant	2.7	2.8	2.9	0.03	0.00	0.02

Table 6.3: Cumulative rejection efficiencies for internal neutrino interaction simulations and burst data. Only events that pass the event reconstruction cuts are included in the calculation.

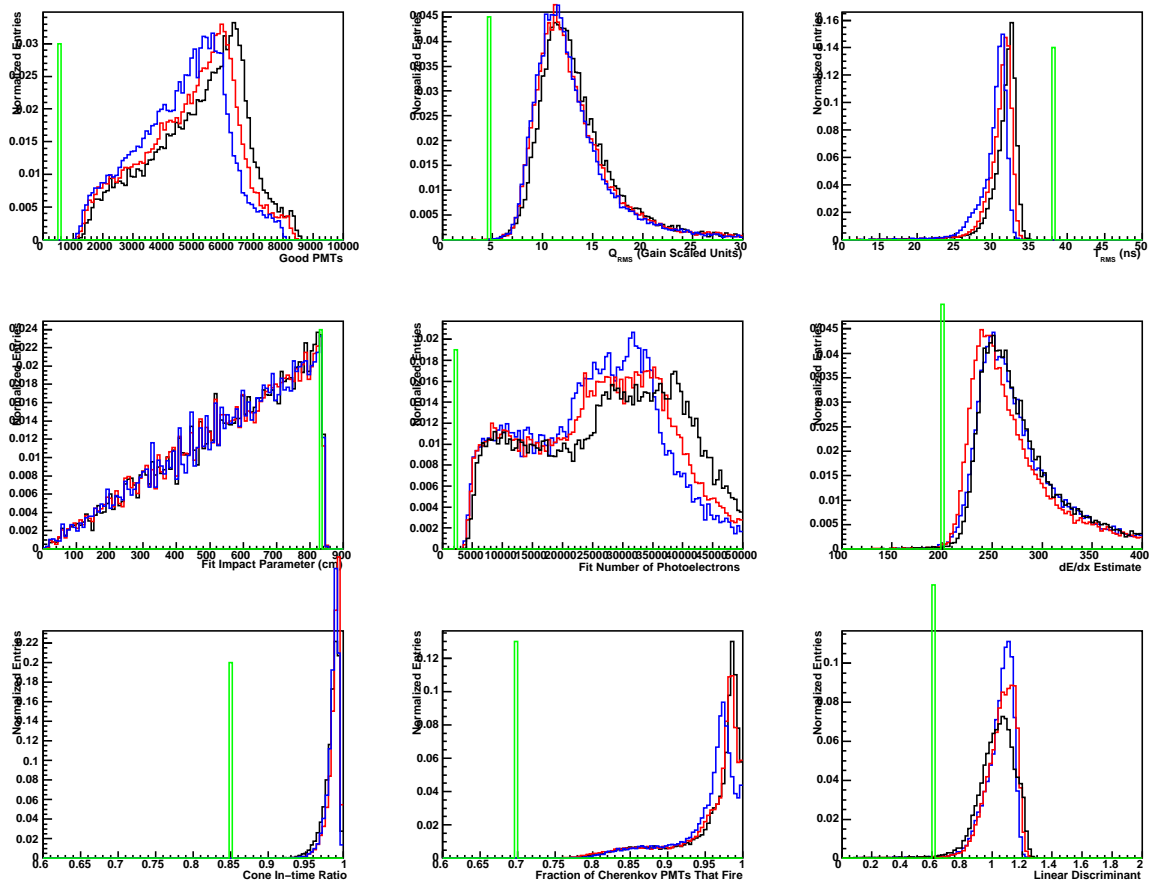


Figure 6-3: Phase stability of cut variables for data. The black histograms are for D<sub>2</sub>O, red for salt, blue for NCD, and the cut values are represented by the green lines.

Cut	Shift Value			Cut Value
	D <sub>2</sub> O	Salt	NCD	
Calibrated PMTs	125	135	35	> 500
$Q_{RMS}$	1.45	1.5	1.55	> 4.5 GSU
$T_{RMS}$	-1.6	-1.2	-1.3	< 38 ns
Impact Parameter	-0.1	0.0	0.3	< 830 cm
Fit Number of Photoelectrons	350	900	700	> 2000 pe
dE/dx	9.5	8	9	> 200 MeV/cm
CITR	0.003	0.0045	0.0035	> 0.85
TRICH	-0.004	-0.003	-0.004	> 0.7
Linear Discriminant	0.11	0.2	0.165	> 0.6

Table 6.4: Amounts that the simulated cut variable distributions must be shifted to agree with the data distributions. A positive value indicates that the data distribution is at higher values than the simulated distribution.

ment between the two distributions was measured by a  $\chi^2$  test, and the best fit point was the minimum  $\chi^2$  value. Table 6.4 shows the size of the best fit shifts with respect to the cut values. While some of the shifts are large compared to the cut values, they are all shifted away from the cut values. This means that any change in the cut efficiencies due to these shifts are likely to be small. However these possible changes need to be included in the signal extraction routine, and will be incorporated as systematic errors in section 8.2.

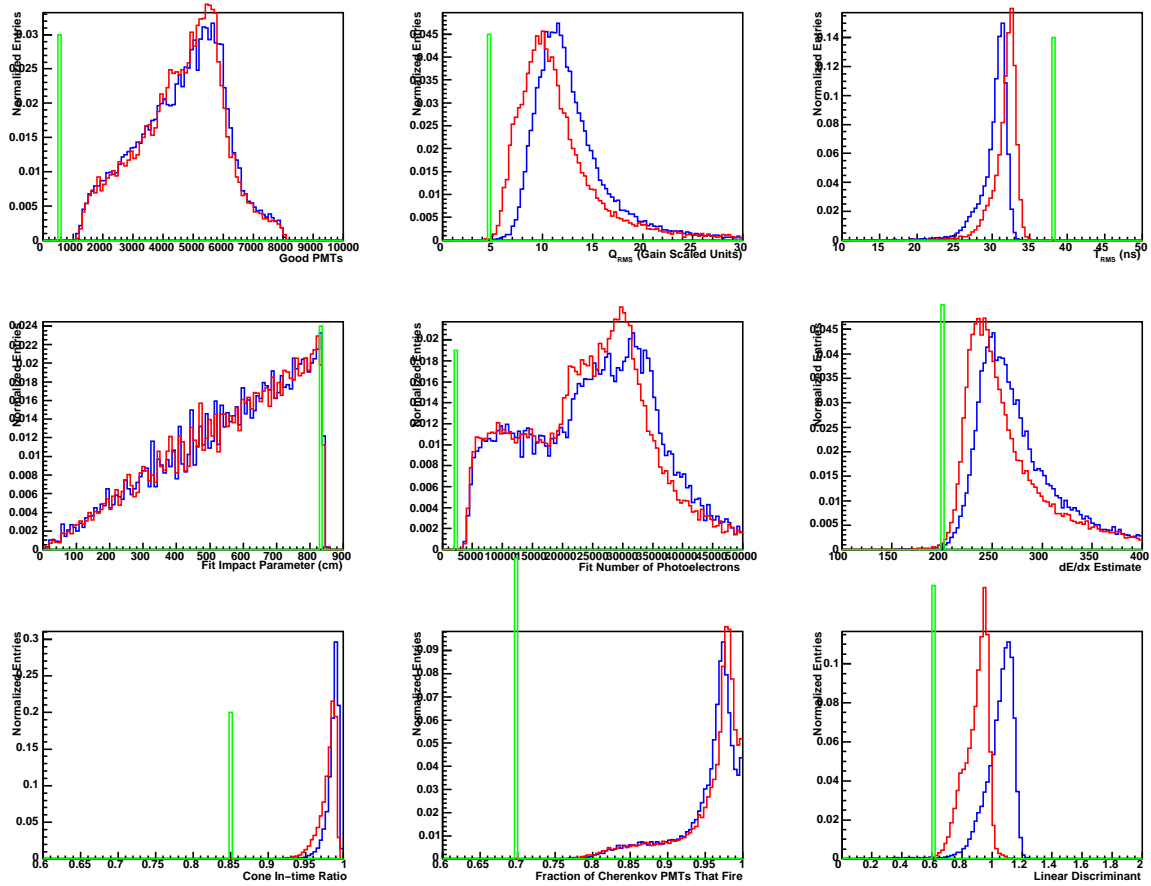


Figure 6-4: Comparison of cut variables for simulated cosmic ray muons (red) and data (blue) for the NCD phase. While most of the distributions agree well, a few such as  $Q_{RMS}$  and the Linear Discriminant show a definite shift between data and Monte Carlo.



# Chapter 7

## Signal Extraction

The signal extraction method is a grid-based binned likelihood fitter. A three dimensional grid of possible  $\Delta m_{23}^2$ ,  $\sin^2(2\theta_{23})$ , and flux multiplier values is created. For each of those points, an expected results histogram is created using the Monte Carlo. The likelihood of the data given that expected histogram is calculated and modified by floating the systematic parameters using the analytical pulls technique. Finally the three dimensional grid of likelihoods is used to calculate the best fit point and the confidence interval contours.

In order to create the expected histograms for each grid point, the Monte Carlo simulations are looped over. If the Monte Carlo event passes the analysis cuts, it is added to the expected histogram with a weight of:

$$\begin{aligned} &w_j \text{ for } \nu_e \text{ and } \bar{\nu}_e \\ w_j [1 - \sin^2(2\theta_i) \sin^2(1.27 \frac{\Delta m_i^2 L}{E})] &\text{ for } \nu_\mu \text{ and } \bar{\nu}_\mu \\ w_j \sin^2(2\theta_i) \sin^2(1.27 \frac{\Delta m_i^2 L}{E}) &\text{ for } \nu_\tau \text{ and } \bar{\nu}_\tau \end{aligned} \quad (7.1)$$

where  $w_j$  is the weight (based on Monte Carlo statistics) of run type  $j$  (i.e.  $\frac{1}{500}$  for upward rock neutrino interactions),  $\theta_i$  and  $\Delta m_i^2$  are the are the oscillation parameters at the given grid point,  $L$  is the distance the neutrino traveled in the simulation, and  $E$  is the energy of the simulated neutrino. The event is binned based on its reconstructed

Dimensions	68%	90%	99%
1-D	1	2.69	6.64
2-D	2.3	4.61	9.21

Table 7.1: Likelihood Cutoff Values for Contours

direction rather than its true simulated direction to take into account the resolution of the muon fitter. If the fitter behaves similarly on data and Monte Carlo, no correction needs to be made for angular misreconstruction. The expected histogram is then multiplied by the flux normalization factor of the grid point, and the cosmic ray muon background is added to produce the final expected signal histogram for the grid point.

Once an expected histogram is created for each grid point, the likelihood is calculated. The likelihood used in this analysis is twice the standard binned likelihood value. It is calculated as:

$$L = 2 \sum_{\text{bins } k} \left[ N_k \ln \frac{N_k}{E_k} + E_k - N_k \right] \quad (7.2)$$

where  $N_k$  is the number of events in bin  $k$  in the data histogram and  $E_k$  is the number of events in bin  $k$  in the expected histogram. This likelihood does not include any systematic uncertainties. In order to include these uncertainties, a change in the likelihood is calculated using the analytical pulls technique. After the changed likelihood is calculated for all grid points, the best fit point is found by scanning over all the points. Contours are then drawn around all points with  $L < L_{min} + CL$  where  $CL$  is given in table 7.1.

## 7.1 Analytical Pulls Technique

The Analytical Pulls Technique was originally developed for  $\chi^2$  based analyses [56], and has been extended to likelihood based analyses by the SNO collaboration [57]. This section will review the technique and demonstrate how it applies to the atmospheric neutrino analysis.

First, define the set of systematic uncertainties as  $\vec{\alpha}$  where the expected values of the uncertainties have been accounted for ( $\langle \vec{\alpha} \rangle = 0$ ) and the error matrix is  $\sigma^{-2}$ . Define the observed number of events in each bin as  $n_i$ , the expected number of events in each bin as  $\mu_i(\vec{\alpha})$ , and the expected number of events with the systematics equal to zero as  $\mu_i$ . With these definitions, the log likelihood (including the factor of 2) can be calculated as:

$$L_{total} = 2 \sum_i [n_i \ln \frac{n_i}{\mu_i(\vec{\alpha})} + \mu_i(\vec{\alpha}) - n_i] + \vec{\alpha}^T \cdot \sigma^{-2} \cdot \vec{\alpha} \quad (7.3)$$

If the systematics are small, the expected number of events can be expanded to first order as:

$$\mu_i(\vec{\alpha}) = \mu_i(1 + \vec{\beta}_i^T \cdot \vec{\alpha}) \quad (7.4)$$

where  $\vec{\beta}_i$  is defined as:

$$\vec{\beta}_i = \frac{1}{\mu_i} \frac{\partial \mu_i}{\partial \vec{\alpha}} \Big|_{\vec{\alpha} \rightarrow 0} \quad (7.5)$$

Using a second-order expansion in  $\ln(1 + x)$ , the likelihood can be expanded as:

$$\begin{aligned} L_{total} &= L_0 + \Delta L \\ L_0 &= 2 \sum_i n_i \ln \frac{n_i}{\mu_i} + \mu_i - n_i \\ \Delta L &= -2 \sum_i (n_i - \mu_i) \vec{\beta}_i^T \cdot \vec{\alpha} + \vec{\alpha}^T \cdot (\sigma^{-2} + \sum_i n_i \vec{\beta}_i \times \vec{\beta}_i^T) \cdot \vec{\alpha} \end{aligned} \quad (7.6)$$

Minimizing  $\Delta L$  with respect to  $\vec{\alpha}$  gives:

$$\vec{\alpha}_{min} = \sum_i \vec{\beta}_i^T (n_i - \mu_i) S^{-2} \quad (7.7)$$

where  $S^2$  is the new error on the systematic parameters  $\vec{\alpha}$ :

$$S^2 = \sigma^{-2} + \sum_i n_i \vec{\beta}_i \times \vec{\beta}_i^T \quad (7.8)$$

Substituting  $\vec{\alpha}_{min}$  back into equation 7.6 yields a compact form for the change in

likelihood:

$$\Delta L = -\vec{\alpha}_{min}^T S^2 \vec{\alpha}_{min} \quad (7.9)$$

The beauty of this method is that by assuming that the effect of the systematics vary linearly with the size of the systematics, we can turn a problem involving minimizing in  $n_{sys}$  dimensions into a problem involving inverting a  $n_{sys} \times n_{sys}$  matrix. In the atmospheric neutrino analysis, the  $\vec{\beta}_i$  terms are calculated by varying each of the systematics by their expected  $1\sigma$  uncertainties, and approximating the derivative as the change in the bin contents:

$$\beta_i^j = \frac{\mu_i - \mu_i^j}{\mu_i} \quad (7.10)$$

Where  $\mu_i^j$  is the expected number of counts in bin  $i$  if systematic  $j$  is changed by  $1\sigma$ . The atmospheric neutrino analysis floats eight systematics using the analytical pulls technique. These will be summarized in section 8. In order to verify that the technique works properly, the likelihood as a function of systematics was calculated independently using equation 7.2 where  $E_k$  is replaced by  $E_k \cdot \prod_{\text{sys } l} \beta_k^l \alpha_l$ . It is found that the analytical pulls technique calculates the correct change in likelihood to within 5%. Figure 7-1 shows the likelihood calculated in this manner as a function of each of the systematics parameters at the best fit point. The minimum of each likelihood curve lies at the extracted best fit point, demonstrating that the technique has found the minimum likelihood value.

## 7.2 Signal Extraction Validation

In order to validate the signal extraction code, two simulations were run to test whether the signal extraction recovers the correct best fit point, and whether the contours correctly account for statistical fluctuations. In the first simulation, contours are generated for a fake data set at the MINOS best fit point ( $\Delta m^2 = 0.002625$ ,  $\sin^2(2\theta) = 1$ , flux multiplier =1) without statistical fluctuations or systematic uncertainties. This means that the fake data distribution is set exactly equal to the Monte Carlo prediction for that set of parameters and that the signal extraction routine does

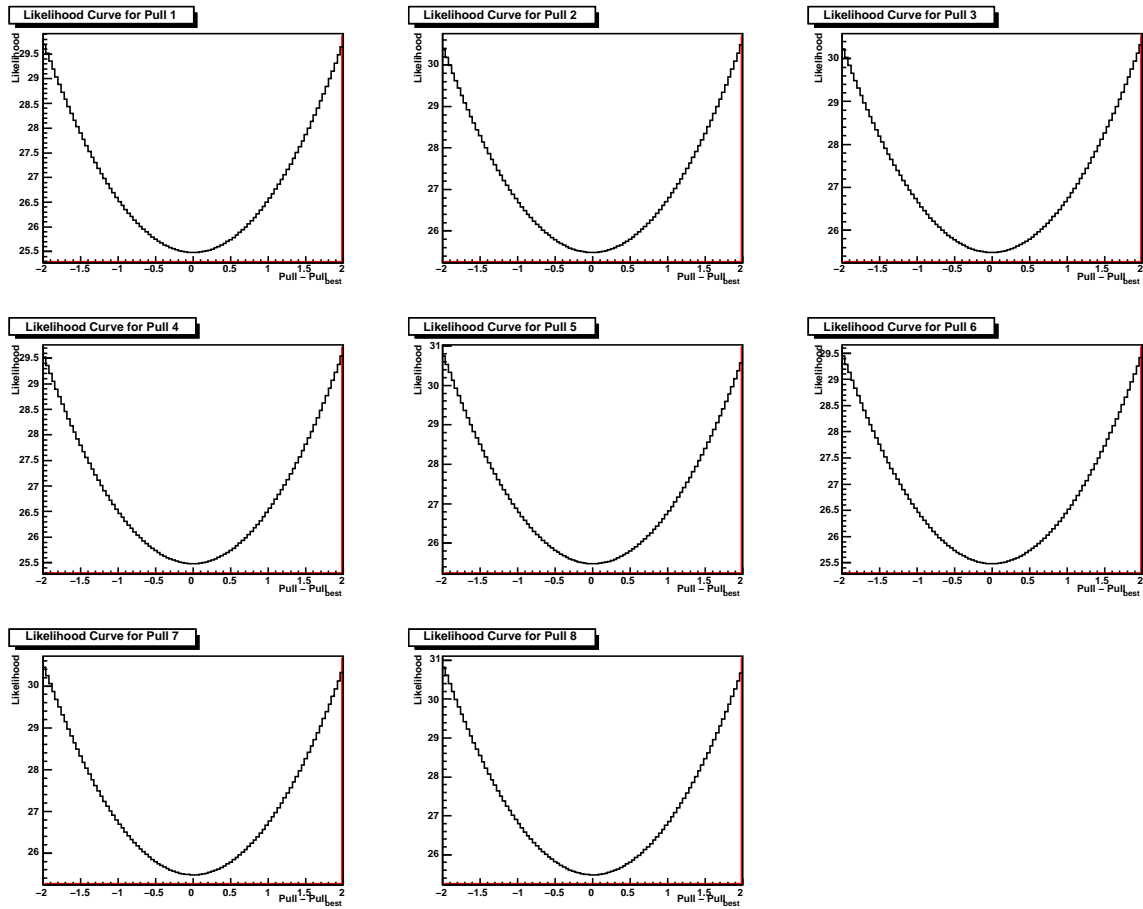


Figure 7-1: Likelihood as a function of systematic parameter. Each curve shows the effect of changing the given systematic parameter while keeping the other systematic parameters and oscillation parameters at their best fit points from the analytical pulls technique. The fact that each curve has a minimum at zero indicates that the analytical pulls technique works. The correspondence between pull number and systematic is given in table 8.3.

not include systematics. Then many fake data sets are generated with the same oscillation parameters, but including statistical fluctuations. The best fit point (without systematics) from each of these fake data sets is then compared to the contours.

Figures 7-2, 7-3, and 7-4 show the contours overlaid with the results of 1000 fake data sets. These demonstrate that the general shape of the contours agrees with the distribution of best fit points. In order to test the statistical validity of the 68%, 90%, and 99% contours, the percentage of best fit points within the contours was calculated in each of the three presentation planes. The percentages are roughly 74%, 94%, and 99.8% respectively for all of the planes, larger than expected. The most likely reasons for this are that many of the best fit points lie on the edge of the signal extraction region, which may make them appear in the wrong contour, and that the fake data set without statistical fluctuations may overestimate the width of the contours. In a data set with statistical fluctuations, the best fit point will have roughly half of the data points below the prediction and roughly half above. This makes the likelihood curve steeper than when all of the data points lie exactly on their predictions. Thus it seems reasonable that this 68% contour contains more than 68% of the best fit points.

In the second simulation, fake data distributions without statistical fluctuations are created for randomly chosen  $\Delta m^2$ ,  $\sin^2(2\theta)$ , and flux normalization parameters. The standard signal extraction routine including systematics is then run on the fake data and the best fit point compared to the simulated value. Figures 7-5, 7-6, and 7-7 show the results of these comparisons for each of the three parameters.

Figure 7-5 demonstrates that the signal extraction does not work well for very low values of  $\Delta m^2$ . For these values, the energy above which neutrinos do not oscillate becomes very low, and therefore few neutrinos will oscillate. Thus it becomes difficult to tell the difference between cases with a low  $\Delta m^2$  and large  $\sin^2(2\theta)$  and cases with a large  $\Delta m^2$  and small  $\sin^2(2\theta)$ . Luckily, these problems do not occur in the region where Super Kamiokande and MINOS expect the best fit point to be. In this good region, the signal extraction accuracy is around 10% for the oscillation parameters, which is better than the expected statistical uncertainty.

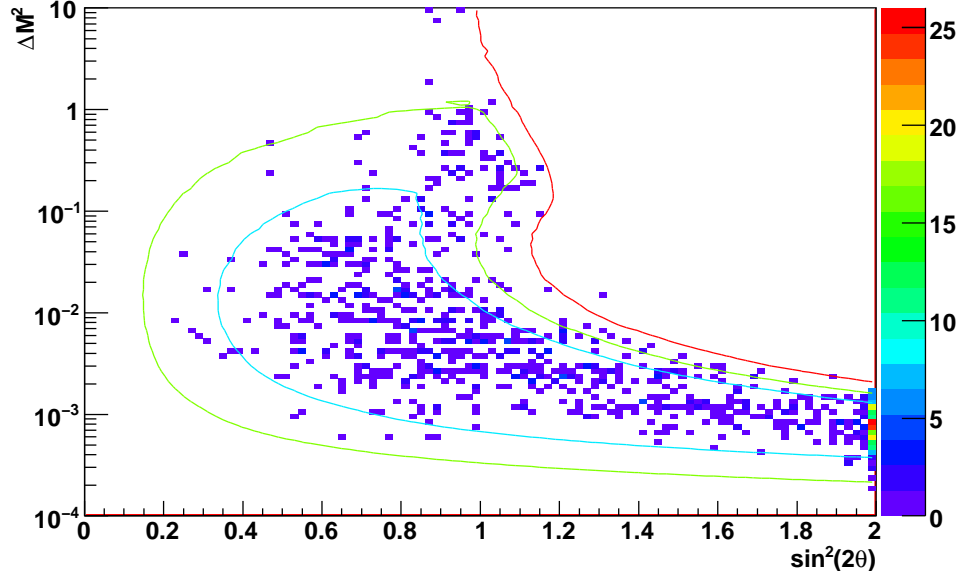


Figure 7-2: Contours from a fake data set without statistical fluctuations overlaid on the best fit points from 1000 fake data sets including statistical fluctuations. The 68%, 90%, and 99% contours contain 75.4%, 93.8%, and 99.8% of the best fit points respectively.

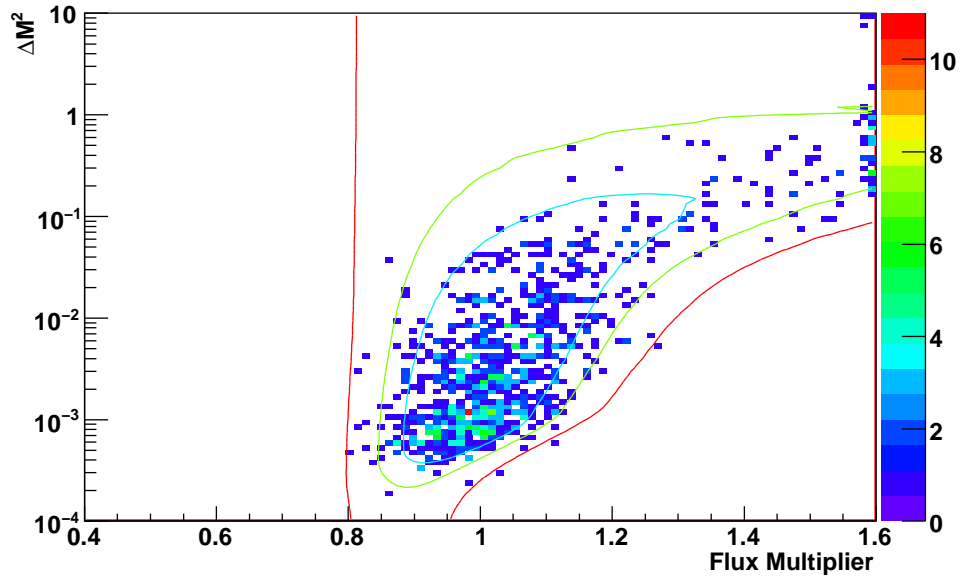


Figure 7-3: Contours from a fake data set without statistical fluctuations overlaid on the best fit points from 1000 fake data sets including statistical fluctuations. The 68%, 90%, and 99% contours contain 72.5%, 94.2%, and 99.7% of the best fit points respectively.

Figure 7-6 shows the signal extraction accuracy on  $\sin^2(2\theta)$  as a function of simulated  $\sin^2(2\theta)$ . The signal extraction accuracy is  $\pm 0.03$ , which is significantly better than the expected statistical uncertainty. Figure 7-7 shows the signal extraction accuracy on the flux multiplier. The signal extraction comes within 2% of the input flux multiplier, which is again better than the expected statistical uncertainty.

These two studies demonstrate that the signal extraction routine finds the correct best fit point and draws statistically correct contours.

### 7.3 Super Kamiokande and MINOS Constraints

In order to perform a global atmospheric neutrino analysis and set better limits on the flux of atmospheric neutrinos, the likelihood surfaces from other experiments must be included. The current best measurements of  $\sin^2(2\theta_{23})$  and  $\Delta m_{23}^2$  come from Super Kamiokande and MINOS. The best constraint on  $\sin^2(2\theta_{23})$  comes from Super Kamiokande's angular distribution analysis [7], while the 2008 MINOS result [11] gives the best constraints on  $\Delta m_{23}^2$ . Super Kamiokande's L/E analysis [58] constrains  $\Delta m^2$  better than its angular distribution analysis, but not as well as MINOS. Thus the two results that will be included are Super Kamiokande's angular distribution analysis (figure 7-8) and the MINOS result (figure 7-10).

Since likelihood maps are not readily accessible for these two results, two-dimensional gaussian approximations to their likelihood curves have been created. Two-sided gaussian approximations to the likelihood space were created and the parameters varied by hand until the 68% and 90% contours of the approximations were as close as possible to the digitized points. Although both papers used  $\chi^2$  techniques with confidence levels set at slightly different  $\chi^2$  values, the approximation uses the likelihood method with 68% set at 2.30, 90% set at 4.61, and 99% set at 9.21 as required for 2-D distributions.

The functional form of the log-likelihood approximation to the Super K results is:

$$\begin{aligned}
L = & 4.61 \frac{(x - x_{center})^2}{s_x^2} \\
& + 4.61 \frac{(\Delta m^2 - \Delta m_{center}^2)^2}{s_{\Delta m^2+}^2} (\Delta m^2 \geq \Delta m_{center}^2) \\
& + 4.61 \frac{(\Delta m^2 - \Delta m_{center}^2)^2}{s_{\Delta m^2-}^2} (\Delta m^2 < \Delta m_{center}^2)
\end{aligned} \tag{7.11}$$

where  $x = \sin^2(2\theta)$ . The first term is a gaussian approximation of the  $\sin^2(2\theta)$  uncertainty, while the second and third terms are a two-sided gaussian approximation of the  $\Delta m^2$  uncertainty. The  $s$  parameters in this fit are not standard deviations. They are the 90% confidence level equivalent of the standard deviation, and can be converted into standard deviations by dividing by  $\sqrt{4.61}$ . Figure 7-9 displays the results of this approximation.  $\Delta m_{center}^2$ ,  $s_{\Delta m^2+}^2$ , and  $s_{\Delta m^2-}^2$  were adjusted so that the 90% contour (green) matched the data well while the 68% contour (blue) was reasonably correct. The values obtained are summarized in table 7.2.

The functional form of the log-likelihood approximation to the MINOS results is

Parameter	Super Kamiokande	MINOS
$x_{center}$	1	1
$s_x$	0.072	0.295
$\Delta m_{center}^2$	$1.9 \times 10^{-3}$	$2.6 \times 10^{-3}$
$s_{\Delta m^2+}$	$1.46 \times 10^{-3}$	$7.4 \times 10^{-4}$
$s_{\Delta m^2-}$	$3.6 \times 10^{-4}$	$4.4 \times 10^{-4}$
$\alpha$		$2.8 \times 10^{-3}$

Table 7.2: Gaussian fit parameters for oscillation parameter constraints from Super Kamiokande and MINOS.

slightly more complicated:

$$\begin{aligned}
L = & 4.61 \frac{(x - x_{center})^2}{s_x^2} \\
& + 4.61 \frac{(\Delta m^2 - (\Delta m_{center}^2 + \alpha(1 - x)))^2}{s_{\Delta m^2+}^2} \\
& \cdot (\Delta m^2 \geq \Delta m_{center}^2 + \alpha(1 - x)) \\
& + 4.61 \frac{(\Delta m^2 - (\Delta m_{center}^2 + \alpha(1 - x)))^2}{s_{\Delta m^2-}^2} \\
& \cdot (\Delta m^2 < \Delta m_{center}^2 + \alpha(1 - x))
\end{aligned} \tag{7.12}$$

where  $\alpha$  is a correlation term. This is simply the previous two-dimensional gaussian function with the addition of a correlation between  $\sin^2(2\theta)$  and  $\Delta m^2$ . The results of the approximation displayed in figure 7-11 are summarized in table 7.2. These constraints will be used to improve the measurement of the atmospheric neutrino flux.

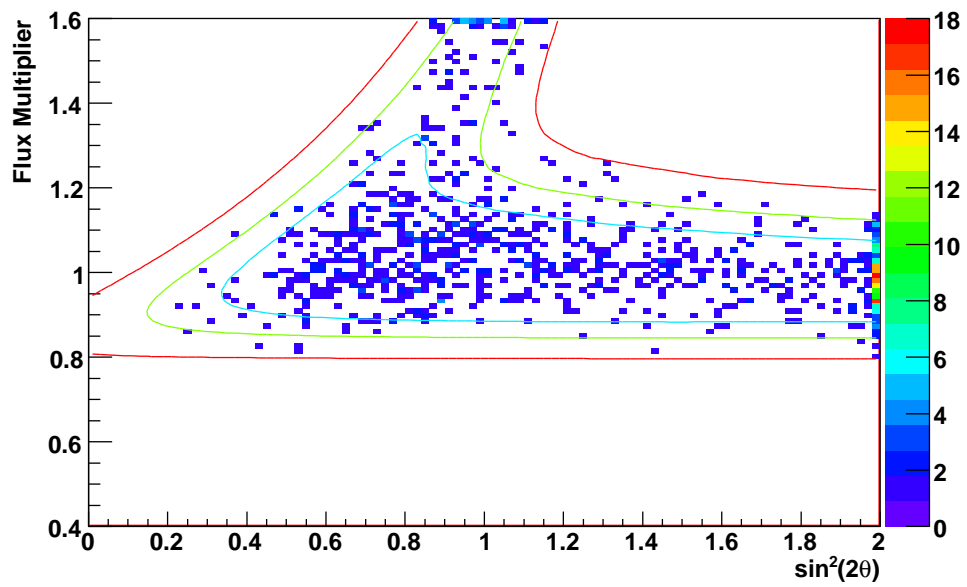


Figure 7-4: Contours from a fake data set without statistical fluctuations overlaid on the best fit points from 1000 fake data sets including statistical fluctuations. The 68%, 90%, and 99% contours contain 75.5%, 94.5%, and 100% of the best fit points respectively.

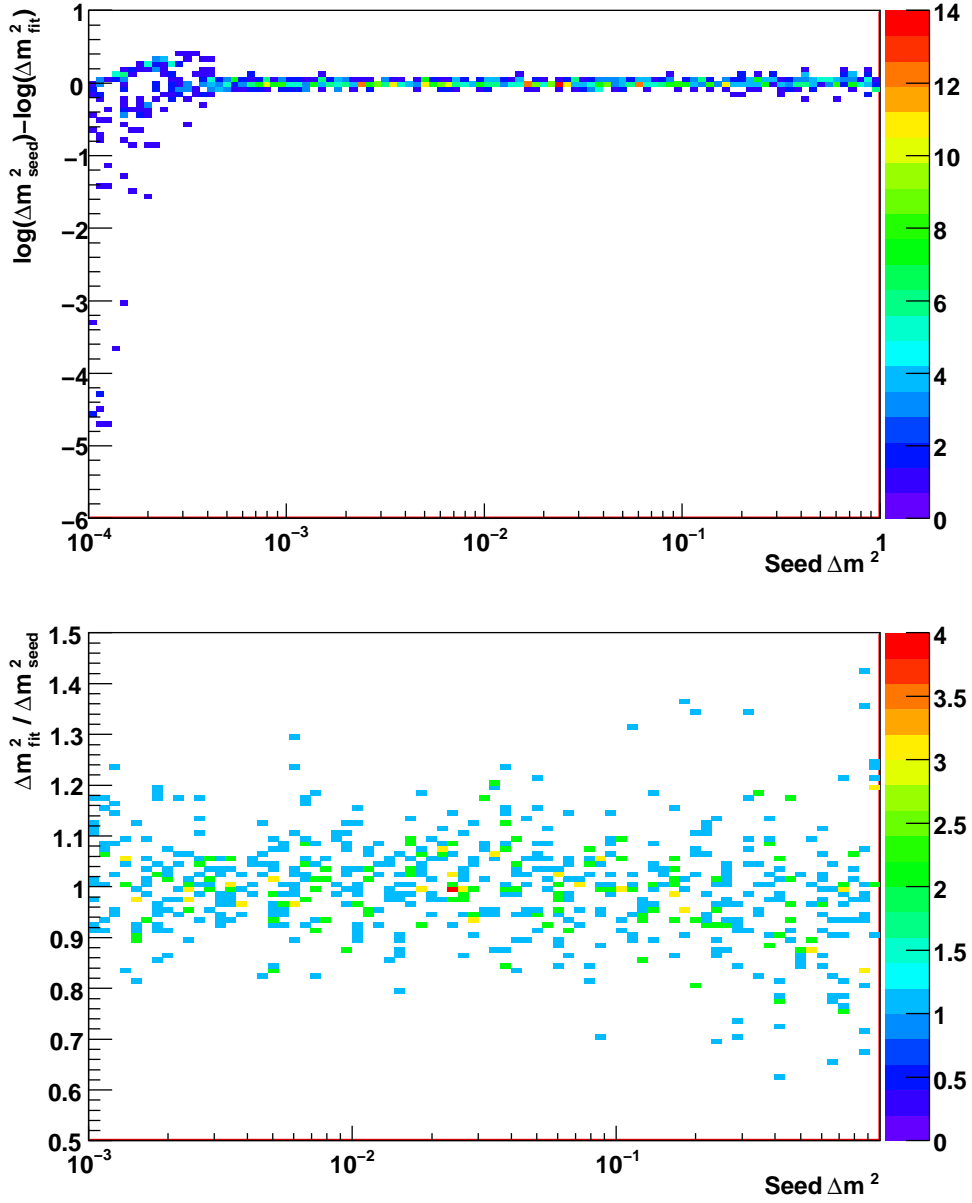


Figure 7-5: Signal extraction accuracy on  $\Delta m^2$  as a function of simulated  $\Delta m^2$ . The top plot shows that the signal extraction is very bad for  $\Delta m^2 < 5 \times 10^{-4}$ . The bottom plot shows that above that cutoff, the extraction is good to  $\pm 20\%$ , which is much better than the statistical uncertainty on the measurement of  $\Delta m^2$ .

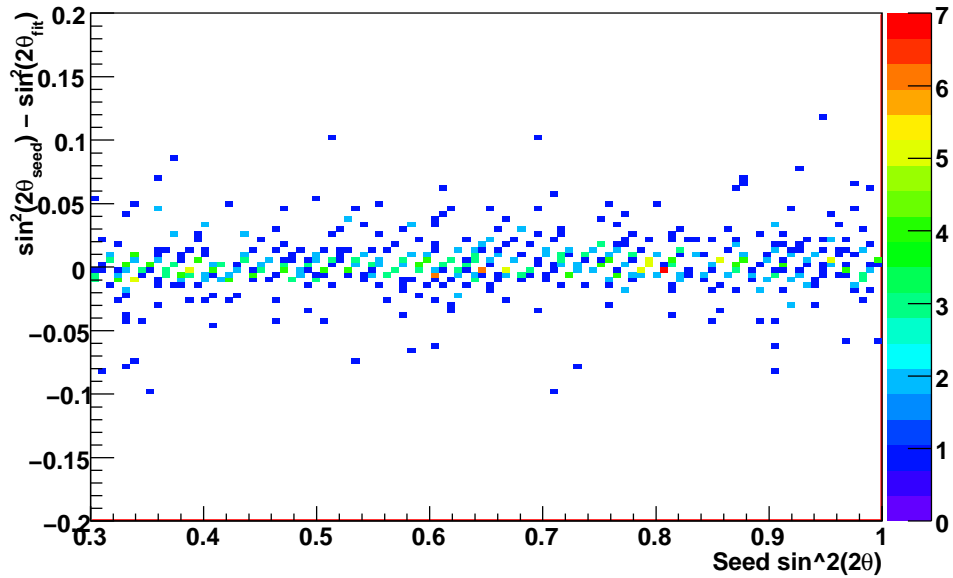


Figure 7-6: Signal extraction accuracy on  $\sin^2(2\theta)$  as a function of simulated  $\sin^2(2\theta)$ . The diagonal lines come from the fact that the best fit points have a grid spacing of 0.02. This plot shows that the signal extraction accuracy is better than  $\pm 0.03$  which is significantly better than the statistical uncertainty on the measurement of  $\sin^2(2\theta)$ .

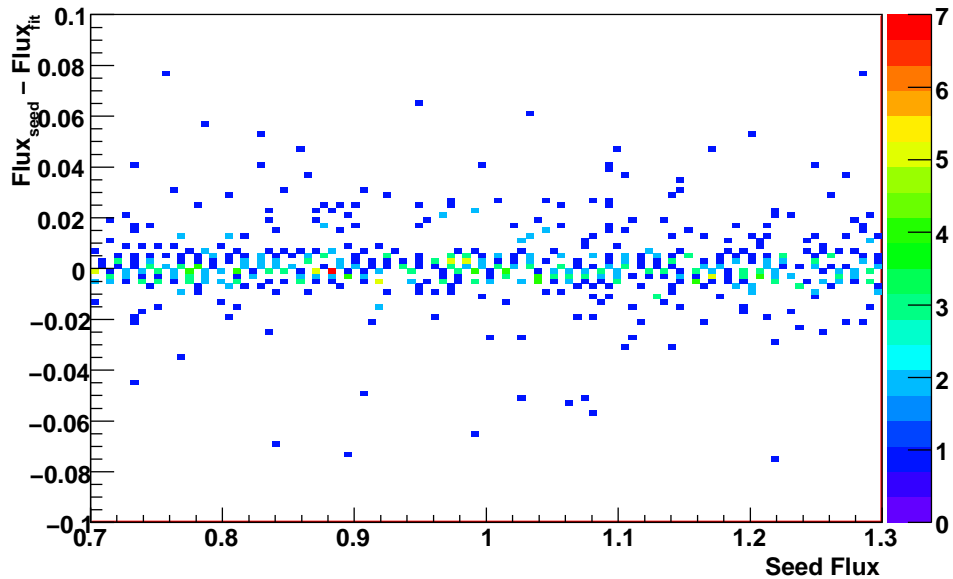


Figure 7-7: Signal extraction accuracy on the flux multiplier as a function of simulated flux multiplier. For all values, the flux multiplier is reconstructed to better than 2%, which is better than the statistical uncertainty on the flux multiplier measurement.

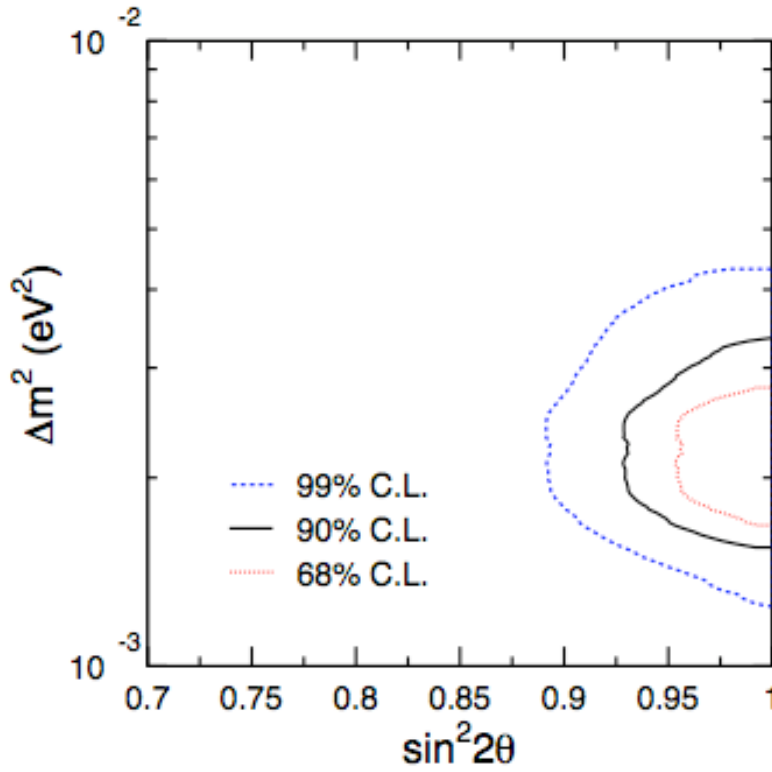


Figure 7-8: Contour plot from Super Kamiokande [7].

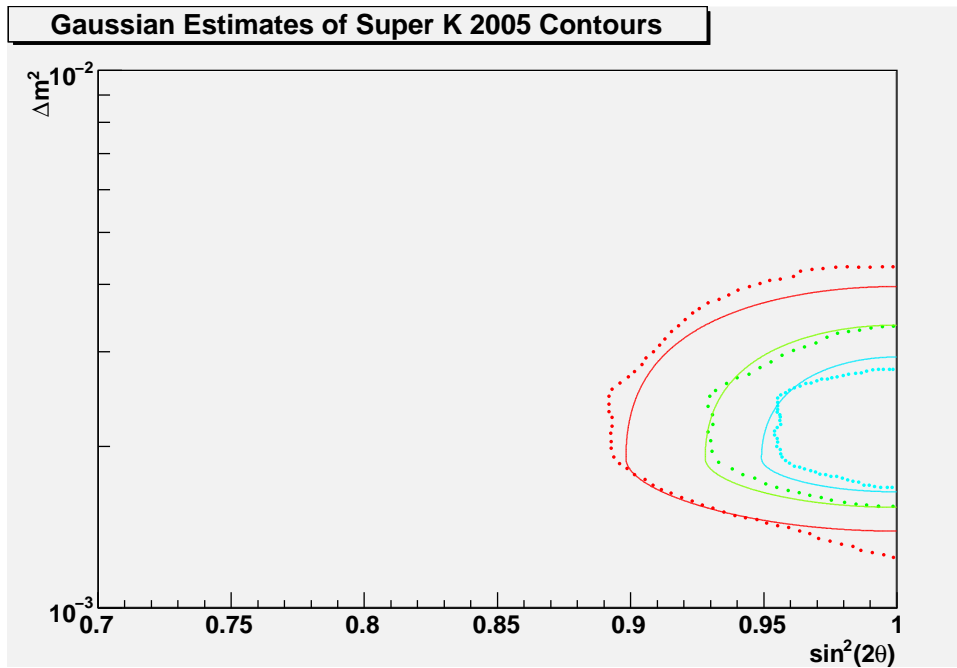


Figure 7-9: The colored dots indicate the results of digitizing figure 7-8. The lines are the 68% (blue), 90% (green), and 99% (red) contours obtained from a gaussian approximation to the log-likelihood surface.

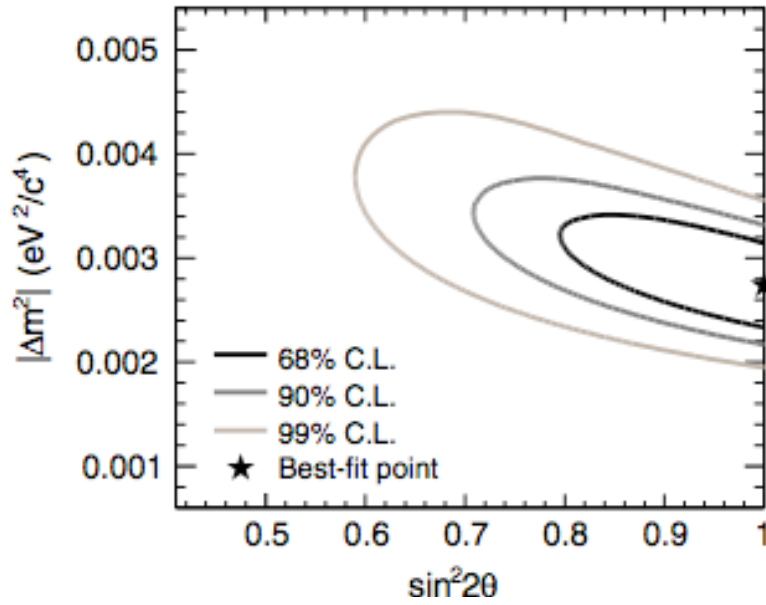


Figure 7-10: Contour plot from MINOS [11]

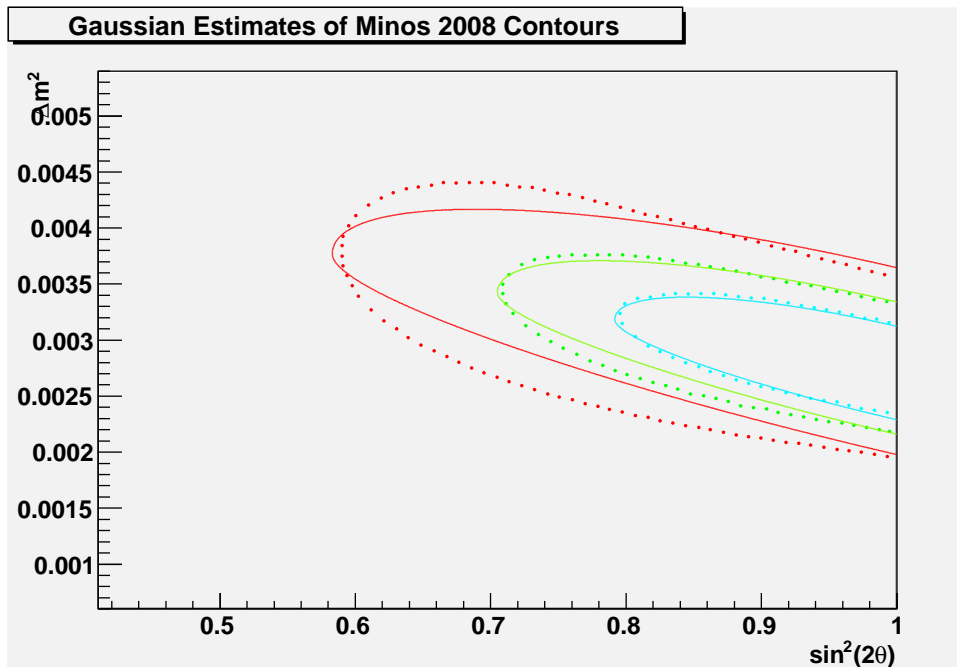


Figure 7-11: The colored dots indicate the results of digitizing figure 7-10. The lines are the 68% (blue), 90% (green), and 99% (red) contours obtained from a gaussian approximation to the log-likelihood surface.



# Chapter 8

## Systematic Uncertainties

To take into account uncertainties in the simulations and the parameters that went into them, systematic uncertainties will be added to the signal extraction routine. In particular, in order to allow the systematic uncertainties to change the shape of the  $\cos(\theta_{zenith})$  distribution, the dominant uncertainties are included as  $\vec{\beta}_i$  terms in the analytical pulls technique (see section 7.1), where the  $\vec{\beta}_i$  terms are calculated by varying each of the systematics by their expected  $1\sigma$  uncertainties, and approximating the derivative as the change in the bin contents:

$$\beta_i^j = \frac{\mu_i - \mu_i^j}{\mu_i} \quad (8.1)$$

Where  $\mu_i^j$  is the expected number of counts in bin  $i$  if systematic  $j$  is changed by  $1\sigma$ . This section will document the systematic uncertainties that have been evaluated for the atmospheric neutrino analysis.

### 8.1 Cross-Section Uncertainties

One of the largest uncertainties associated with all neutrino oscillation experiments is the uncertainty on previously measured neutrino interaction cross-sections. The uncertainties on the cross-sections are detailed in section 6.2.2, along with their estimated impact on the total flux of neutrinos. For this analysis, the effects of these

uncertainties were treated in more detail as floating systematics. In each case, a secondary simulation was run with the cross-section in NUANCE modified by the 68% uncertainty, and the  $\cos(\theta_{zenith})$  distribution based on this altered simulation was calculated. With the new distribution, the  $\vec{\beta}_i$  terms for each systematic were calculated using equation 8.1.

## 8.2 Data - Monte Carlo Based Uncertainties

Section 6.3.4 demonstrated that there are significant shifts between the data and Monte Carlo distributions of some of the cut variables. These shifts could change the efficiencies of the cuts, and thus need to be accounted for as systematic uncertainties. To evaluate these uncertainties, the  $\cos(\theta_{zenith})$  distribution of neutrino-induced muons is produced with the cuts at their nominal values and at the shifted values. Some of the variables such as the number of calibrated PMTs and  $T_{RMS}$  have the cut value far enough from the distribution that shifting the distribution does not change the cut efficiency. However three of the variables show a definite change in efficiency due to the shift seen between data and Monte Carlo. Figure 8-1 shows the fractional change in the  $\cos(\theta_{zenith})$  distribution due to the change in efficiency caused by shifting the dE/dx distribution. Notice that it is much larger for upward going neutrino-induced muons than for downward going ones. This is likely due to the neck of the detector. While the muon fitter does its best to compensate for the neck, if too many photons are missed because of the neck, the estimate of the dE/dx will be low. This is one case where not floating this systematic could lead to an incorrect measurement of  $\Delta m^2$  or  $\sin^2(2\theta)$ . Figures 8-2 and 8-3 show the effects of shifting the  $Q_{RMS}$  and Linear Discriminant distributions. In both cases the systematic shows no structure with respect to  $\cos(\theta_{zenith})$  except for the upward-going bin in the Linear Discriminant. Once again, this is most likely due to the neck of the detector. These three systematics lead to an overall uncertainty in the atmospheric neutrino flux of 2.5%, 0.4%, and 2.1% respectively, putting them well in line with the other systematics.

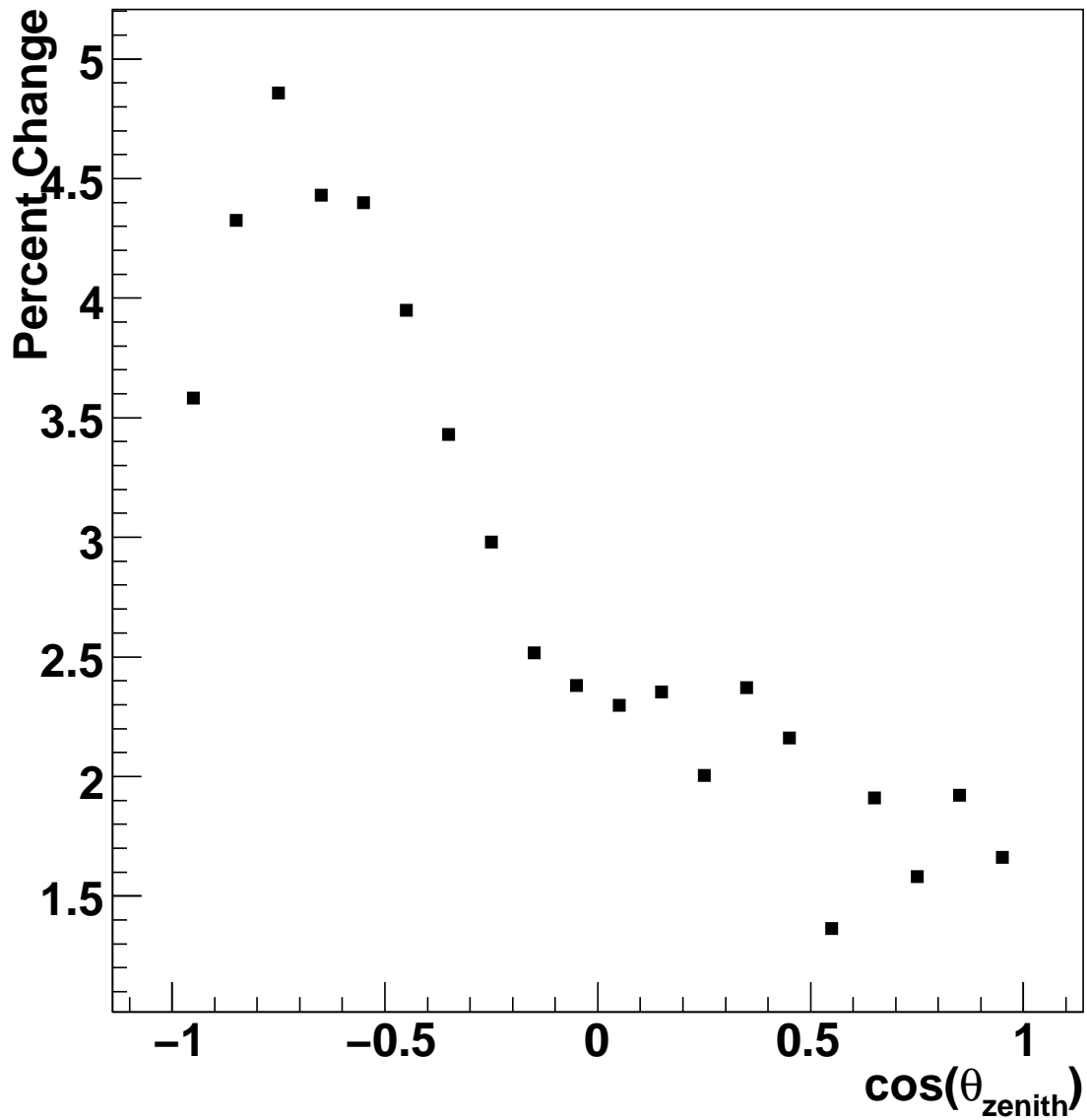


Figure 8-1: Percent change in the  $\cos(\theta_{zenith})$  distribution due to shifting the  $dE/dx$  simulation distribution to match that of the data.

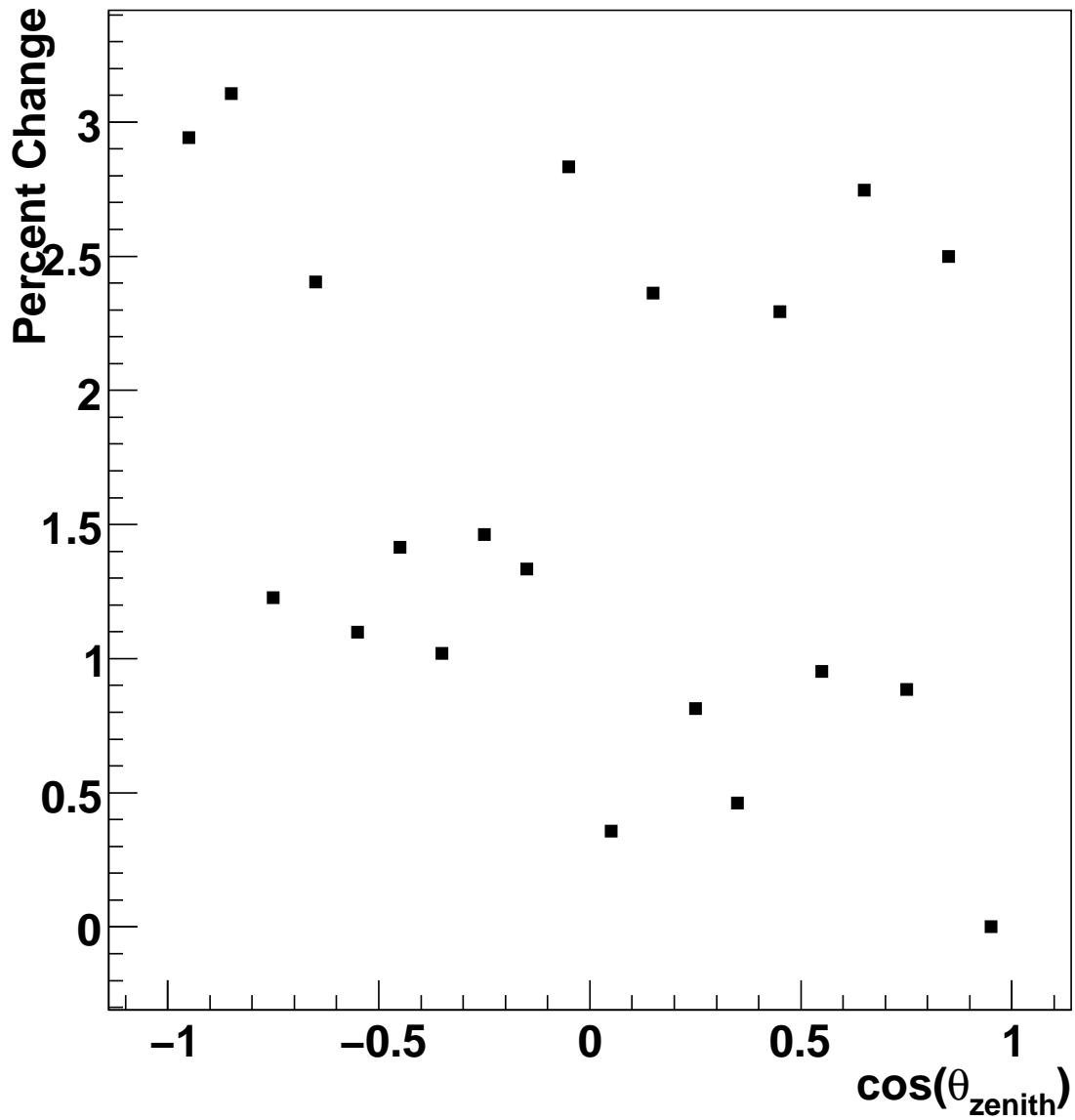


Figure 8-2: Percent change in the  $\cos(\theta_{zenith})$  distribution due to shifting the  $Q_{RMS}$  simulation distribution to match that of the data.

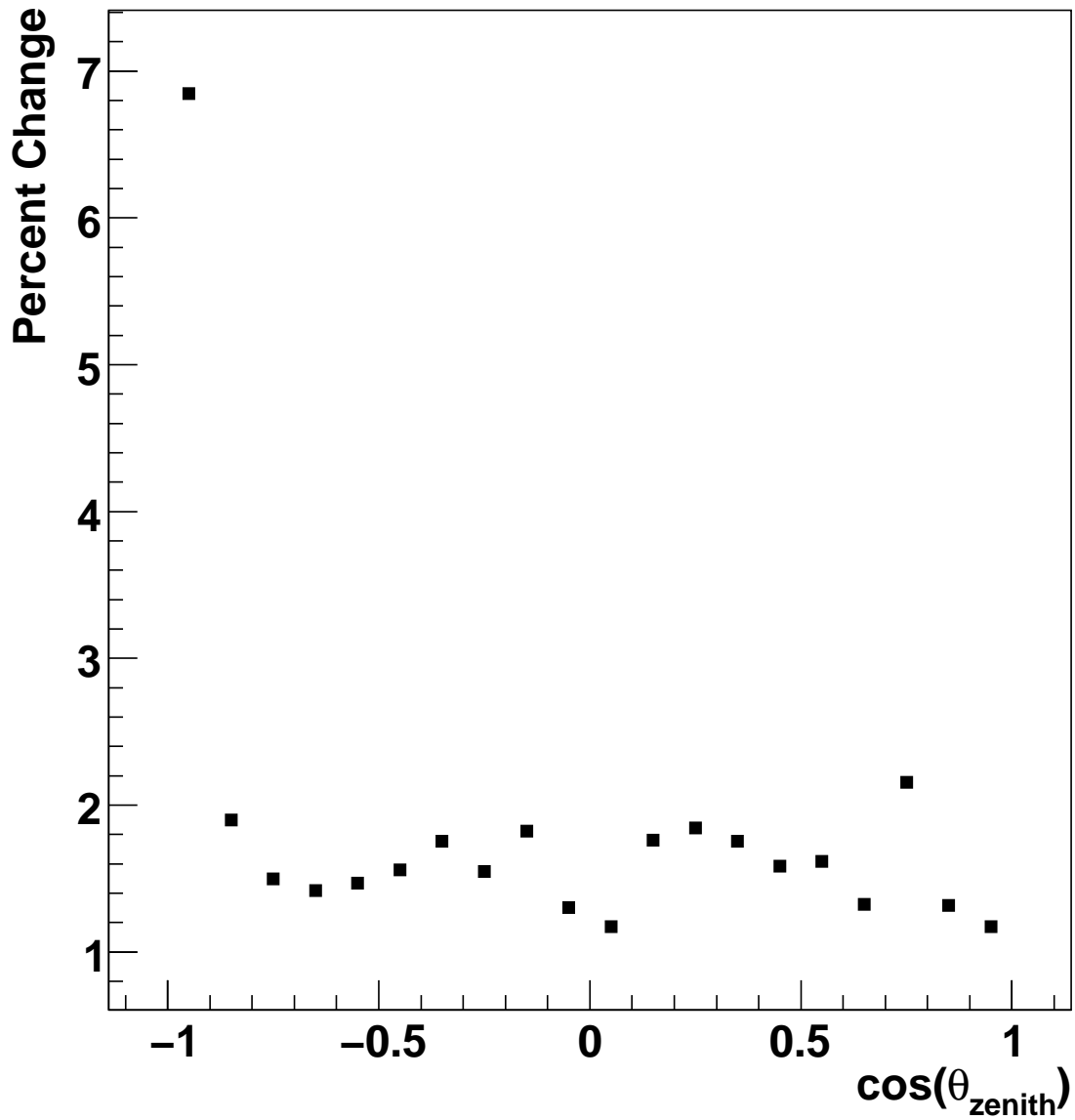


Figure 8-3: Percent change in the  $\cos(\theta_{zenith})$  distribution due to shifting the Linear Discriminant simulation distribution to match that of the data.

## 8.3 Uncertainty Due To Measured Angular Misreconstruction

One uncertainty that could have a large impact on the oscillation parameters in the atmospheric neutrino analysis is the angular reconstruction accuracy of the muon fitter. If the accuracy is on the order of the bin size of the  $\cos(\theta_{zenith})$  histogram, it will be very important to include this smearing in the expected histogram. Since the atmospheric neutrino analysis is based off of SNOMAN Monte Carlo, it has the angular and impact parameter misreconstruction distributions of the simulations built in. However the EMuS analysis has measured the angular misreconstruction distribution to be 50% wider than predicted by SNOMAN. In order to estimate the effect of this systematic on the atmospheric neutrino analysis, a study was performed on the SNOMAN upward muon Monte Carlo. For each event, the misreconstruction angle was multiplied by 1.5 to get a new muon direction. Figure 8-4 shows the fractional change in each bin due to this systematic. Since the fractional change in any bin is less than 1.2% in the analysis region, has no distinct shape, and is not expected to change the overall atmospheric neutrino flux, this systematic is insignificant compared to cross-section and other detector response uncertainties.

## 8.4 Impact Parameter Bias Uncertainty

In order to estimate the uncertainty on the fiducial area of the detector, we must have an estimate of the uncertainty on the impact parameter reconstructed by the muon fitter. To do this, a study was performed comparing the impact parameter distributions from data and Monte Carlo. In the study, the data distribution was held constant while the Monte Carlo distribution was shifted by a multiplicative scaling factor ( $fib' = fib * (1 + scale)$ ). For each shift, the  $\chi^2/dof$  was calculated, and the  $1\sigma$  uncertainty was defined as the shift for which the  $\chi^2/dof$  becomes the minimum value plus 1 as seen in figure 8-5. Table 8.1 shows the extracted 68% confidence limits on a possible scaling difference for each of the three phases. To be conservative, the

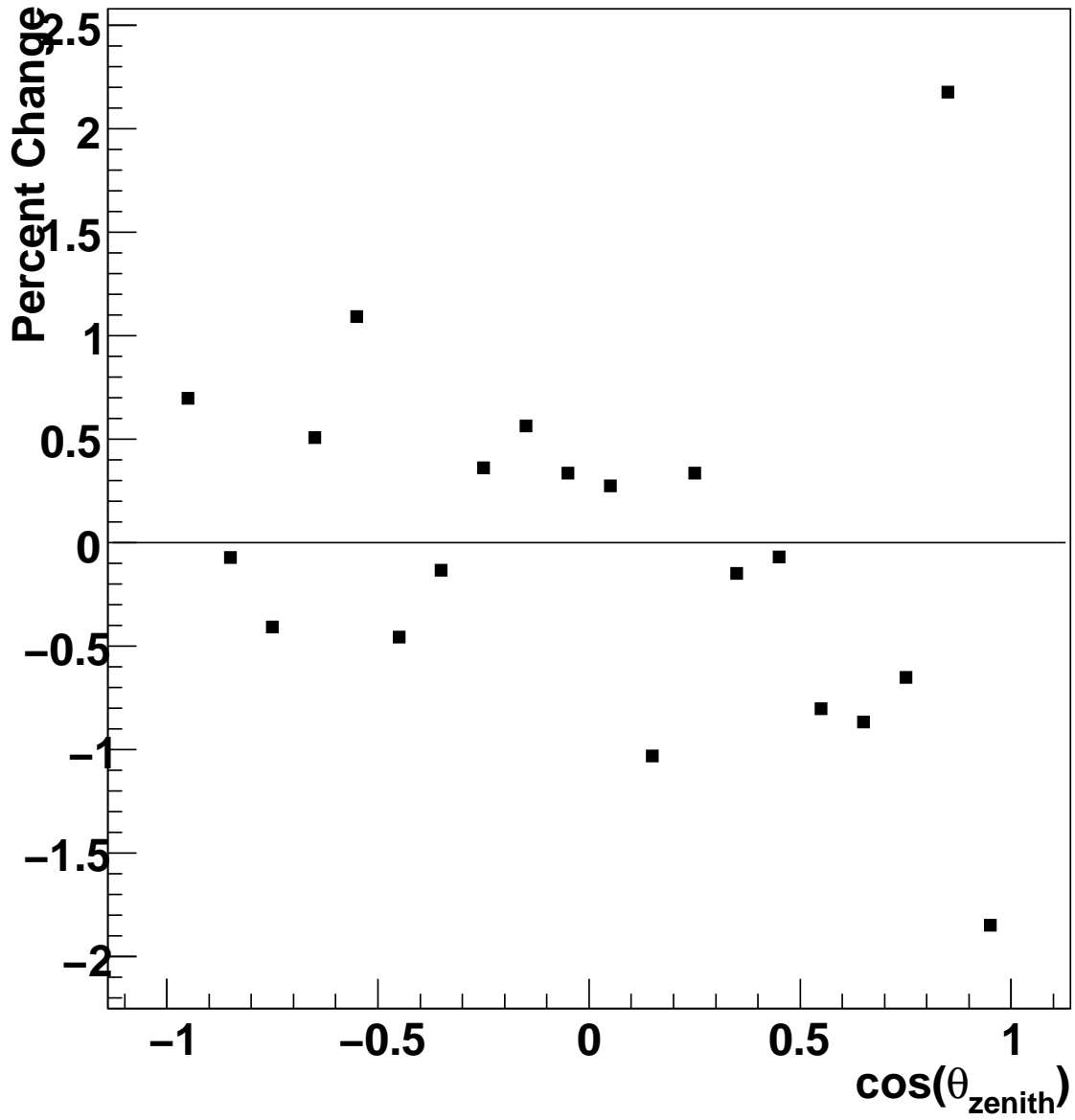


Figure 8-4: Percent change due to increased angular misreconstruction. The fractional change is less than 1.2% in the atmospheric neutrino analysis region ( $\cos(\theta_z) < 0.4$ ).

D <sub>2</sub> O	-0.25%	+0.45%
Salt	-0.23%	+0.48%
NCD	-0.30%	+0.45%

Table 8.1: 68% confidence level limit estimates obtained by comparing data and Monte Carlo impact parameter distributions.

largest of these uncertainties (0.48%) was chosen as the systematic uncertainty on the impact parameter. The majority of data and Monte Carlo used in this study comes from cosmic ray muons, which have very high energies. The neutrino-induced muons which will be studied in the atmospheric neutrino analysis have significantly lower energies and are slightly harder to reconstruct. Based on Monte Carlo studies, the impact parameter misreconstruction should be 20% worse for neutrino-induced muons than for cosmic ray muons. Thus the impact parameter uncertainty is 0.58% for neutrino-induced muons, which becomes a 1.2% uncertainty on the fiducial area of the atmospheric neutrino analysis.

## 8.5 Solar Modulation

The solar wind prevents low energy cosmic rays from reaching the surface of the earth. Over the many years of SNO data taking, the sun went from a solar minimum to a solar maximum, changing the strength of the solar wind. This solar modulation could change the number of low energy atmospheric neutrinos, which would in turn change the extracted oscillation parameters. The BARTOL group [21] has produced simulations for solar minimum and solar maximum. The difference between those predictions is shown in figure 8-6. Figure 8-7 shows the simulated energies of the neutrinos that produce muons observed in the detector. More than 80% of the neutrinos observed by SNO are above 10 GeV, where there is no solar modulation. Almost all of the remaining neutrinos are above 3 GeV, where there is less than 5% change between solar minimum and solar maximum. Thus there is less than 1% expected change in the flux due to solar modulations. Seasonal variations in the cosmic ray flux are also expected to produce around a 1% uncertainty on the atmospheric neutrino flux.

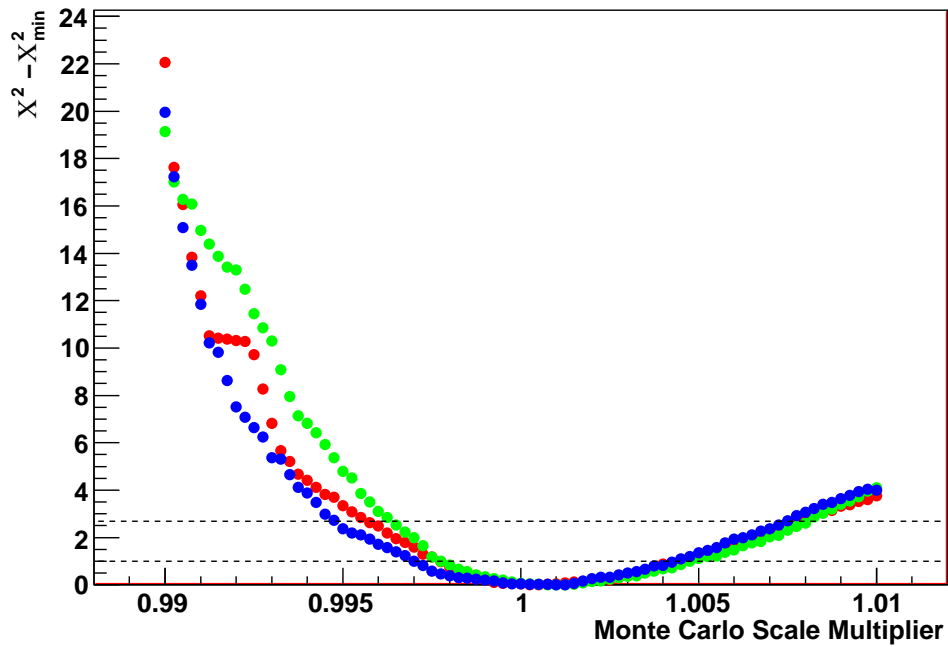


Figure 8-5:  $\chi^2/dof$  as a function of multiplicative scale factor between data and Monte Carlo impact parameter distributions. The lines correspond to 68% and 90% confidence limits on a possible impact parameter scale change.

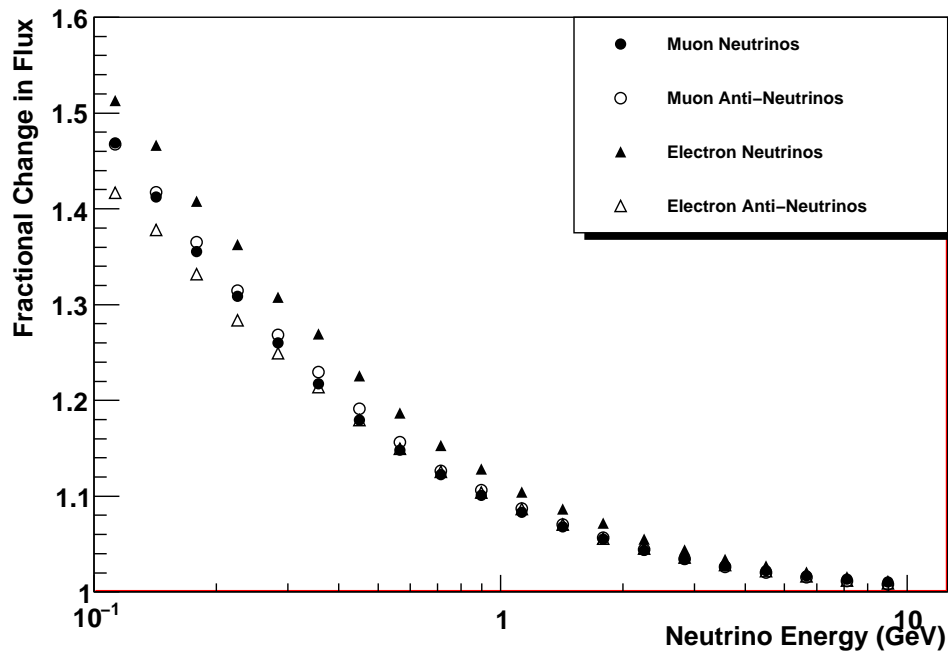


Figure 8-6: Percent change in neutrino fluxes predicted by the BARTOL group between solar minimum and solar maximum.

## 8.6 Other Uncertainties

The remaining uncertainties are generally small, and are not easily categorized. The largest of these is the uncertainty on the PROPMU muon transport code [55], which produces a 2% uncertainty on the flux of atmospheric neutrinos. Similarly, the SNO-MAN Monte Carlo has uncertainties that contribute a 0.3% uncertainty to the flux. Uncertainties on the density of the surrounding rock are estimated to produce a 0.3% uncertainty on the flux, while the stability of the clock used to calculate the livetime of the detector produces a 0.002% uncertainty.

## 8.7 Summary

The above systematic uncertainties are summarized in table 8.2. The four cross-section uncertainties and the three data-Monte Carlo based uncertainties are included as floating systematics which are allowed to change the shape of the  $\cos(\theta_{zenith})$  distribution. The remaining uncertainties are combined into a 2.6% flat floating systematic.

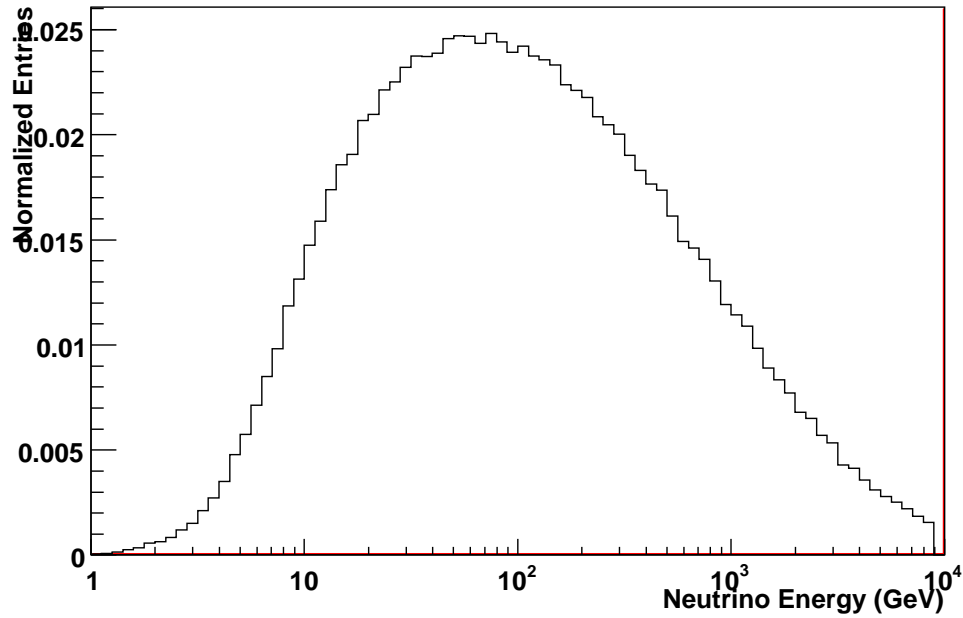


Figure 8-7: Energies of simulated neutrinos which produce muons observed in SNO.

Systematic Uncertainty	Change in Flux
<b>Detector Related</b>	
Detector Propagation Model	$\pm 0.3\%$
Angular Resolution	$\pm 0.1\%$
Impact Parameter Bias	$\pm 1.2\%$
Livetime	$\pm 0.002\%$
Energy Loss Model*	$\pm 2.5\%$
PMT Charge Model*	$\pm 0.4\%$
Linear Discriminant Cut*	$\pm 2.1\%$
<b>Cross Section</b>	
Axial Mass*	$\pm 1.2\%$
Quasi-Elastic*	$\pm 0.8\%$
Resonance Production*	$\pm 2.1\%$
Deep Inelastic Scattering*	$\pm 2.3\%$
<b>Muon Propagation Model</b>	
Rock Density	$\pm 0.3\%$
Transport Model	$\pm 2\%$
Seasonal Variation	$\pm 1\%$

Table 8.2: Systematic uncertainties associated with the atmospheric neutrino analysis. The uncertainties marked with a \* are treated as floating systematics in the analytical pulls technique, and are allowed to change the shape of the expected distribution. The other uncertainties are combined into a flat 2.6% uncertainty on the flux which is used in the analytical pulls technique.

Systematic Number	Systematic Name	Bin 1	Bin 2	Bin 3	Bin 4	Bin 5	Bin 6	Bin 7	Bin 8
1	Axial Mass	0.0137	0.0136	0.0128	0.0121	0.0134	0.0125	0.0092	0.0106
2	Deep Inelastic Scattering	-0.0219	-0.0221	-0.0219	-0.0223	-0.0223	-0.0222	-0.0228	-0.0230
3	Pion Resonance	-0.0239	-0.0218	-0.0229	-0.0228	-0.0219	-0.0217	-0.0201	-0.0207
4	Quasi Elastic	-0.0095	-0.0092	-0.0091	-0.0085	-0.0089	-0.0090	-0.0084	-0.0074
5	Dedx	0.0318	0.0331	0.0376	0.0355	0.0343	0.0334	0.0264	0.0238
6	Qrms	0.0097	0.0056	0.0069	0.0046	0.0026	0.0036	0.0036	0.0032
7	Linear Discriminant	0.0806	0.0150	0.0186	0.0182	0.0163	0.0189	0.0173	0.0175
8	Flat Systematics	0.026	0.026	0.026	0.026	0.026	0.026	0.026	0.026

Systematic Number	Systematic Name	Bin 9	Bin 10	Bin 11	Bin 12	Bin 13	Bin 14	Overall Change in Flux
1	Axial Mass	0.0111	0.0101	0.0107	0.0107	0.0128	0.0122	0.0116
2	Deep Inelastic Scattering	-0.0229	-0.0231	-0.0232	-0.0230	-0.0226	-0.0226	-0.0227
3	Pion Resonance	-0.0206	-0.0200	-0.0198	-0.0200	-0.0209	-0.0206	-0.0210
4	Quasi Elastic	-0.0075	-0.0072	-0.0074	-0.0078	-0.0084	-0.0084	-0.0082
5	Dedx	0.0212	0.0196	0.0192	0.0196	0.0184	0.0195	0.0251
6	Qrms	0.0027	0.0037	0.0024	0.0032	0.0044	0.0027	0.0039
7	Linear Discriminant	0.0192	0.0183	0.0199	0.0178	0.0189	0.0187	0.0213
8	Flat Systematics	0.026	0.026	0.026	0.026	0.026	0.026	0.026

Table 8.3:  $\vec{\beta}_i$  terms for each of the eight floating systematics.

# Chapter 9

## Results

A total of 514 events are recorded with  $-1 < \cos \theta_{zenith} < 0.4$  in the 1229.30 days of livetime. Of these, 201 are observed in the range  $0 < \cos \theta_{zenith} < 0.4$  in which the neutrinos should not oscillate. The corresponding atmospheric neutrinos fluxes in this region and below the horizon ( $\cos \theta_{zenith} < 0$ ) are  $3.48 \pm 0.25$  (stat.)  $\pm 0.12$  (sys.)  $\times 10^{-13}$   $\text{cm}^{-2}\text{s}^{-1}\text{sr}^{-1}$  and  $2.17 \pm 0.12$  (stat.)  $\pm 0.08$  (sys.)  $\times 10^{-13}$   $\text{cm}^{-2}\text{s}^{-1}\text{sr}^{-1}$  respectively.

The measured flux of through-going muons as a function of zenith angle is displayed in figure 9-1. The blue line represents the expected flux without oscillations while the red line shows the best fit expectation including the floating systematics. The best fit parameters are  $\sin^2(2\theta_{23}) = 1$ ,  $\Delta m_{23}^2 = 1.8 \times 10^{-3}$   $\text{eV}^2$ , and the flux multiplier equals 1.24. Table 9.1 shows the values of the floating systematic parameters at the best fit point. The fact that all of the extracted values are within  $\pm 1$  indicates that the floating systematics are not altering the shape of the distribution significantly. Figures 9-2, 9-3, and 9-4 show the results of the three-dimensional oscillation fit projected onto the three possible correlation planes. In each case, the likelihood is minimized with respect to the missing variable. Figure 9-2 demonstrates that SNO sees a slight correlation between  $\sin^2(2\theta_{23})$  and  $\Delta m_{23}^2$ . This plot is used to extract the 2-D confidence levels for the oscillation parameters:  $\Delta m_{23}^2 = 1.8_{-1.1}^{+7.1} \times 10^{-3}$   $\text{eV}^2$  at the 68% confidence level, and  $\sin^2(2\theta_{23}) > 0.33$  at the 90% confidence level. The best fit point is consistent with the Super Kamiokande and MINOS results, although

Systematic Number	Systematic Name	Extracted Value	Extracted Uncertainty
1	Axial Mass	-0.021	0.986
2	Deep Inelastic Scattering	0.005	0.943
3	Pion Resonance	0.025	0.953
4	Quasi Elastic	0.014	0.993
5	Dedx	-0.116	0.929
6	Qrms	-0.065	0.998
7	Linear Discriminant	-0.548	0.941
8	Flat Systematics	-0.139	0.926

Table 9.1: Best fit values for the floating systematics. A value of 1 would indicate that the systematic has fit to  $1\sigma$  away from its originally estimated value. If the extracted uncertainty is much less than 1, the systematic is well constrained by the data.

not competitive with them. In addition, the fact that  $\sin^2(2\theta) = 0$  is excluded at the 99% confidence level indicates that SNO has ruled out the no oscillation hypothesis. Figure 9-3 shows that there is a correlation between  $\Delta m^2$  and the flux multiplier as expected. This implies that constraining  $\Delta m^2$  based on other measurements should lead to an increase in the precision of the flux measurement. Figure 9-4 demonstrates that  $\sin^2(2\theta)$  and the flux multiplier are mostly independent.

Figures 9-5, 9-6, and 9-7 show the one-dimensional projections of each of the variables with the others minimized. These are used to extract the one-dimensional limits on the oscillation parameters:  $\sin^2(2\theta_{23}) > 0.53$  at 90% confidence,  $\Delta m_{23}^2 = 1.8_{-0.8}^{+1.8} \times 10^{-3} \text{ eV}^2$  at 68% confidence, and the flux multiplier equals  $1.24_{-0.10}^{+0.11}$  at 68% confidence.

In order to improve the flux measurement, a global analysis is performed, including constraints from Super Kamiokande and MINOS as detailed in section 7.3. Figure 9-8 shows the  $\sin^2(2\theta) - \Delta m^2$  contours from this combined analysis. The best fit oscillation parameters using 2-D confidence intervals are  $\Delta m_{23}^2 = 2.5_{-0.3}^{+0.4} \times 10^{-3} \text{ eV}^2$  at the 68% confidence level and  $\sin^2(2\theta_{23}) > 0.936$  at the 90% confidence level. The added data from SNO does not significantly shrink the contours from their previous levels. However the constraints on the oscillation parameters do significantly change the flux multiplier measurement as shown in figure 9-9. With the constraints,

the best fit flux multiplier lies at  $1.27_{-0.09}^{+0.09}$  using 68% 1-D confidence levels.

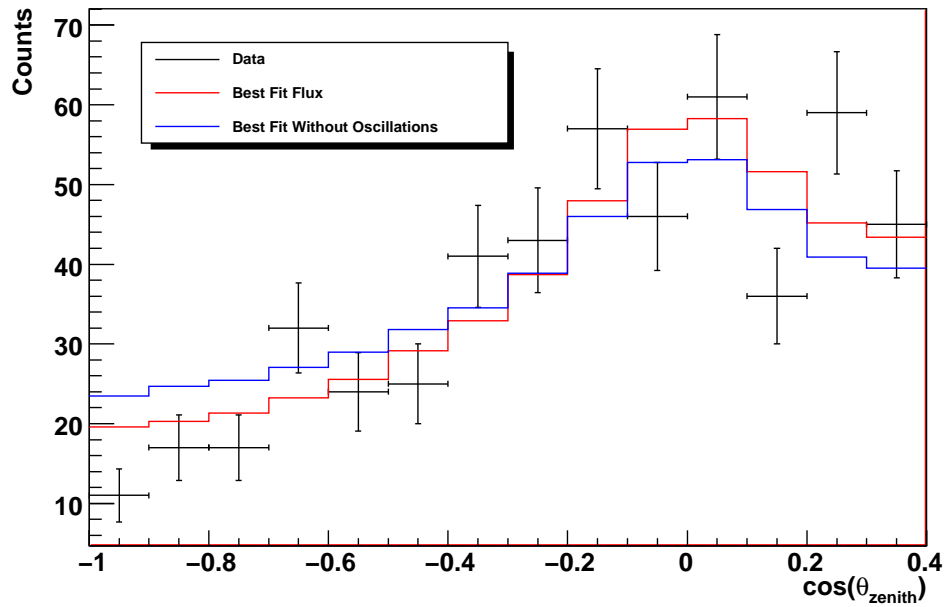


Figure 9-1: Measured flux of through-going muons as a function of zenith angle compared with the expectations for no oscillations and the best fit oscillation parameters.

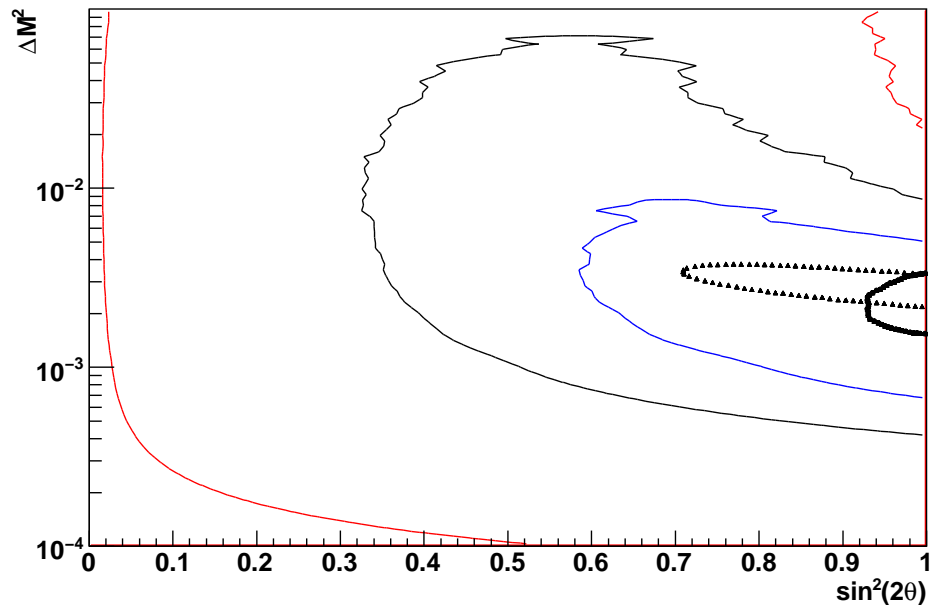


Figure 9-2: Allowed regions in oscillation parameter space based on the SNO data. The likelihood has been minimized with respect to the flux multiplier. The confidence levels are 68% (blue), 90% (black), and 99% red. The black dots represent the 90% confidence contour from Super Kamiokande, while the black triangles represent the 90% confidence contour from MINOS. Since the 99% contour excludes  $\sin^2(2\theta) = 0$ , the no oscillation hypothesis is excluded.

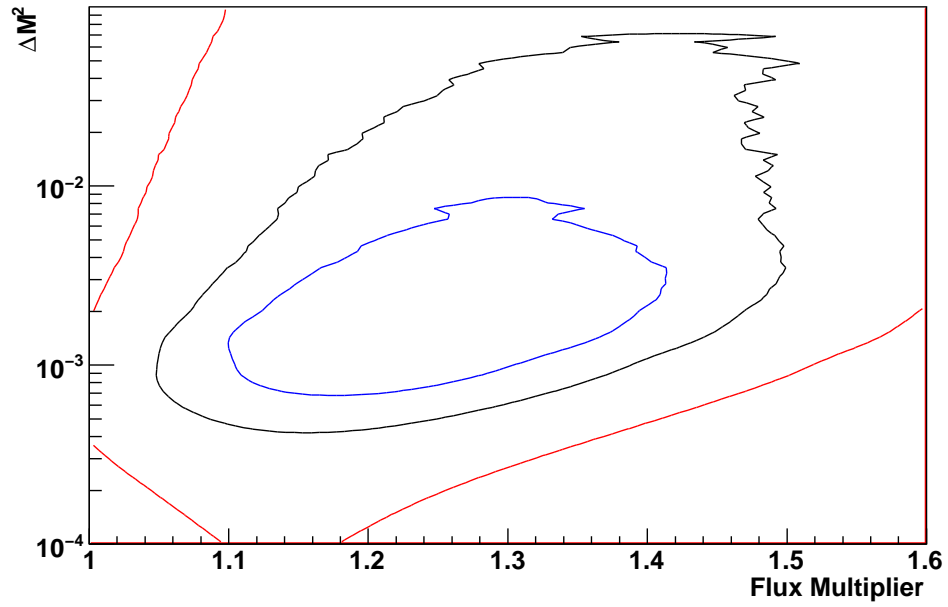


Figure 9-3: Allowed regions in oscillation parameter space based on the SNO data. The likelihood has been minimized with respect to  $\sin^2(2\theta)$ .

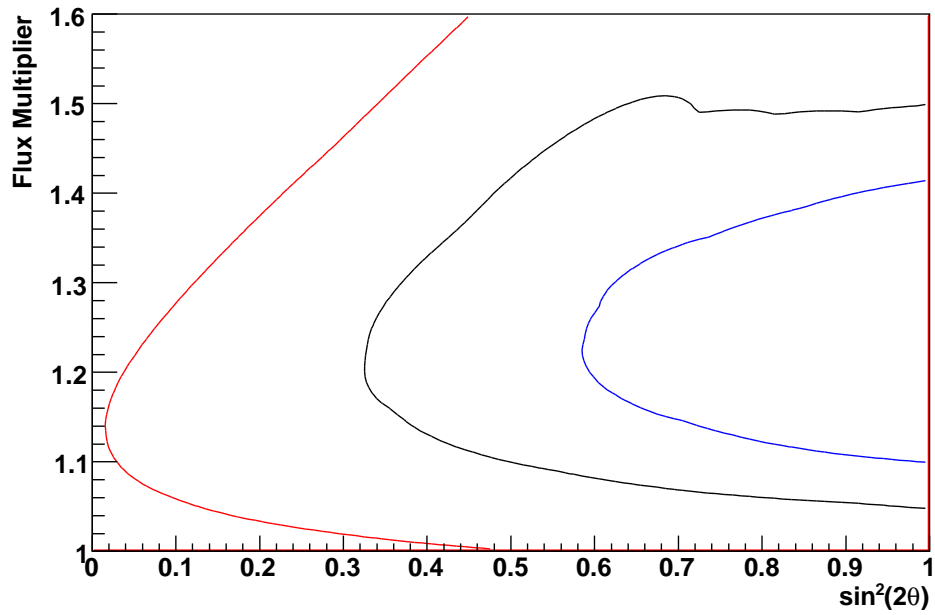


Figure 9-4: Allowed regions in oscillation parameter space based on the SNO data. The likelihood has been minimized with respect to  $\Delta m^2$ .

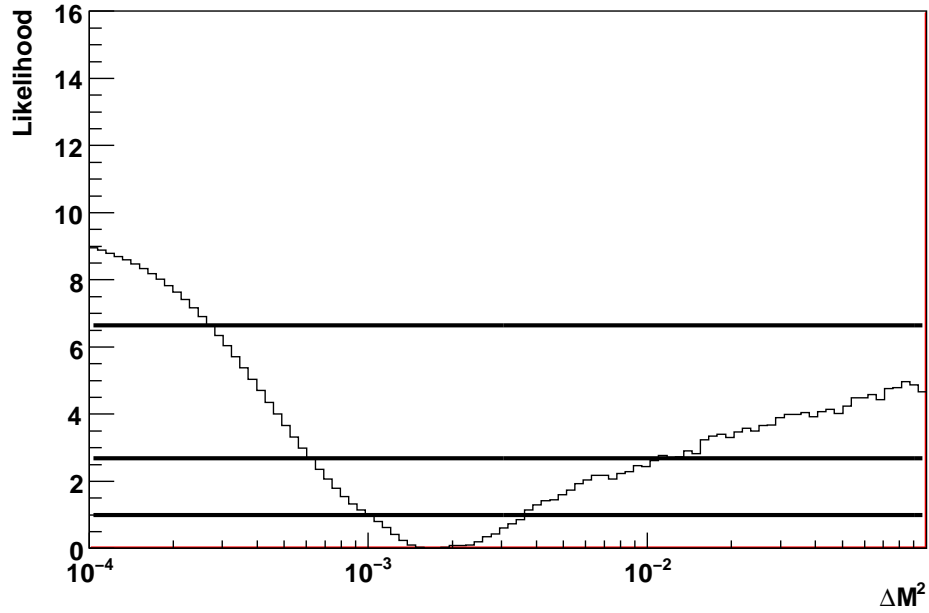


Figure 9-5: Likelihood curve for  $\Delta m_{23}^2$  based on SNO data. The likelihood has been minimized with respect to  $\sin^2(2\theta)$  and the flux multiplier. The black lines correspond to the 68%, 90%, and 99% confidence levels.

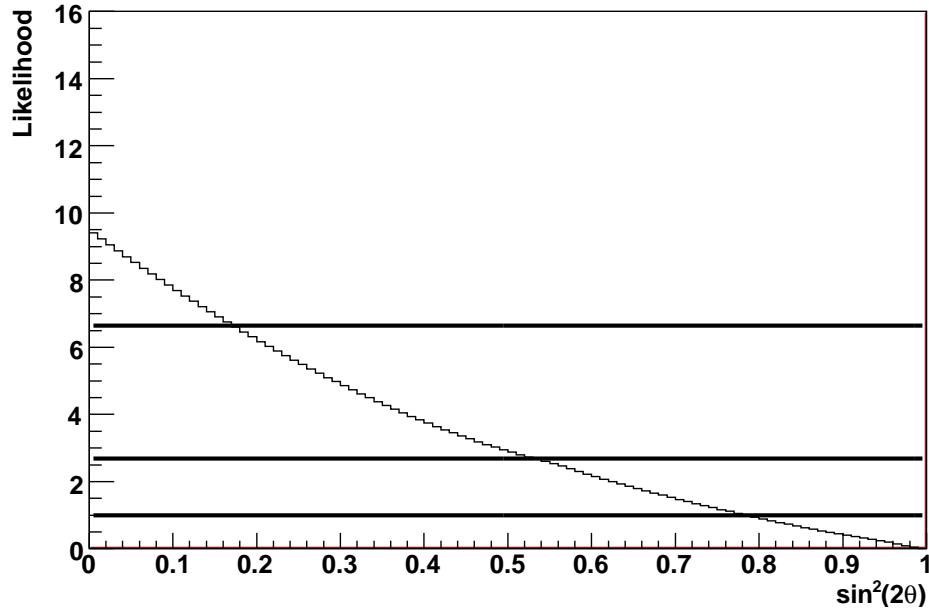


Figure 9-6: Likelihood curve for  $\sin^2(2\theta_{23})$  based on SNO data. The likelihood has been minimized with respect to  $\Delta m^2$  and the flux multiplier. The black lines correspond to the 68%, 90%, and 99% confidence levels.

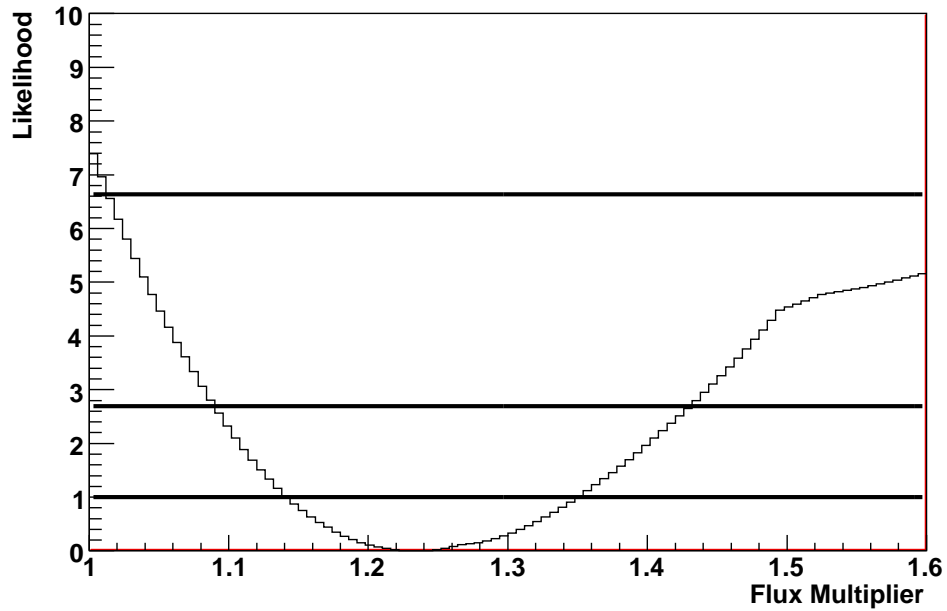


Figure 9-7: Likelihood curve for the flux multiplier based on SNO data. The likelihood has been minimized with respect to  $\sin^2(2\theta)$  and  $\Delta m^2$ . The black lines correspond to the 68%, 90%, and 99% confidence levels.

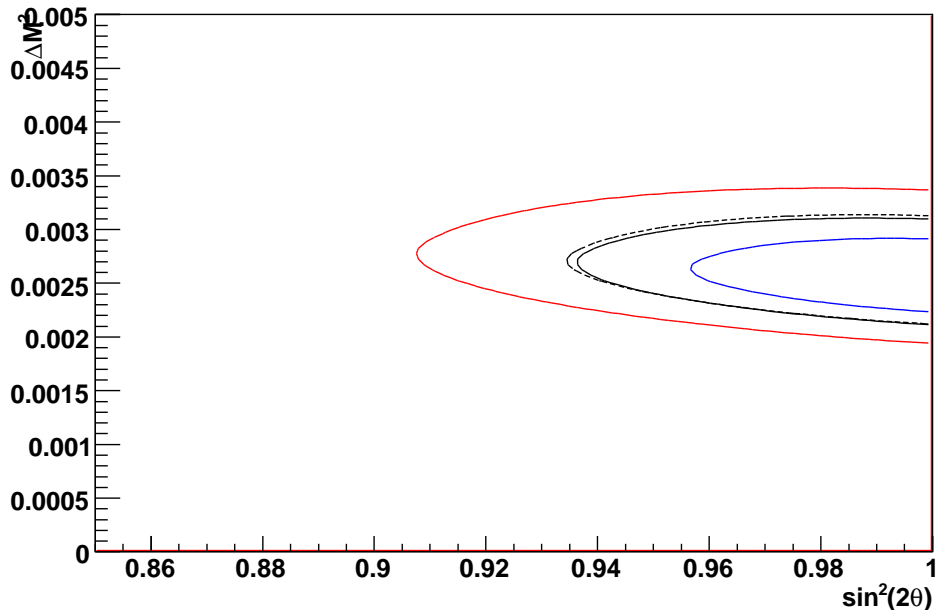


Figure 9-8: Allowed regions in oscillation parameter space based on a global analysis of SNO data, Super Kamiokande, and MINOS. The likelihood has been minimized with respect to the flux multiplier. The dashed black line represent the 90% confidence contour obtained using only the Super Kamiokande and MINOS constraints.

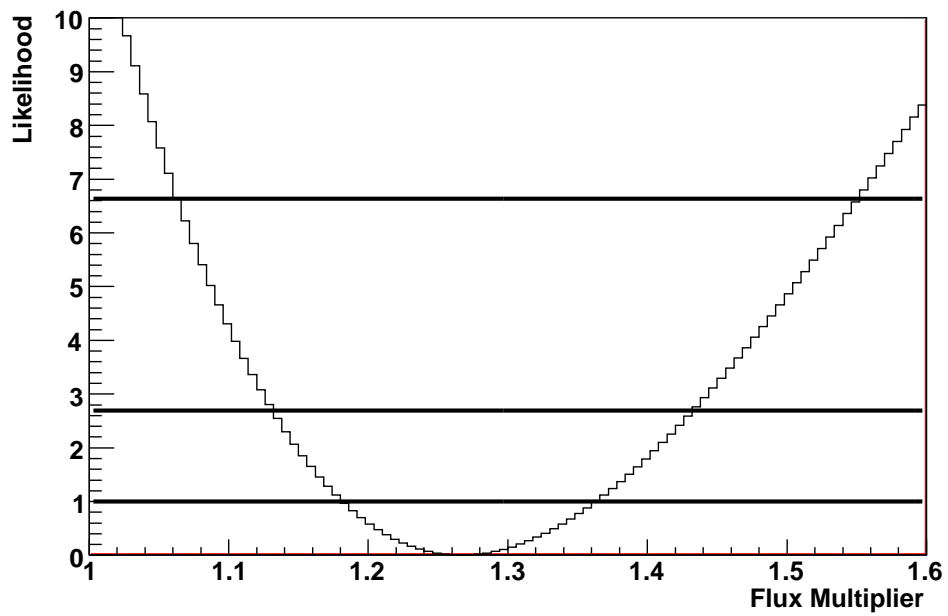


Figure 9-9: Likelihood curve for the flux multiplier based on SNO data with oscillation parameters constrained by the Super Kamiokande and MINOS results. The likelihood has been minimized with respect to  $\sin^2(2\theta)$  and  $\Delta m^2$ .

# Chapter 10

## Conclusions

This measurement of the flux multiplier will be useful in many ways. First it adds a constraint that may help theorists improve estimates of the atmospheric neutrino flux. Although this measurement is an integrated flux rather than a measurement of the energy spectrum of the atmospheric neutrinos, it can help constrain the normalization of the high energy atmospheric neutrino flux. In addition, as cosmic ray measurements such as Auger, Telescope Array, and AMS reduce the uncertainties on the flux of high energy cosmic rays, this constraint may help tune the high energy strong interaction cross-sections that go into the atmospheric neutrino flux simulations.

Secondly, this constraint on the atmospheric neutrino flux will improve searches for extra-solar neutrinos at neutrino telescopes such as AMANDA, Ice Cube, and Baikal. These experiments search for extremely high energy neutrino interactions which should only come from extra-solar sources. The atmospheric neutrino flux is a background to these processes, so a precise measurement of the high energy atmospheric neutrino flux will allow them to remove this background much more efficiently.

In addition, this measurement may help dark matter experiments reduce their backgrounds from neutrino interactions by giving a more precise estimate of the atmospheric neutrino flux. Atmospheric neutrinos can be very energetic and could cause a recoil in a dark matter experiment that would be indistinguishable from dark matter. For that reason, the flux of atmospheric neutrinos must be well known

so that the rate of these interactions can be subtracted. In addition, atmospheric neutrinos produce muons at all depths in the earth, limiting the effectiveness of going deeper underground to reduce the muon background. This measurement clearly demonstrates that neutrinos are an irreducible source of muons which can produce neutrons and radioactive elements through spallation.

Finally, this measurement could be used in a combined analysis with Super Kamiokande to further constrain the atmospheric neutrino oscillation parameters. Such an analysis would involve creating a joint likelihood based on a given atmospheric neutrino flux. Super Kamiokande floats many parts of the neutrino flux in order to properly account for the uncertainty on the flux, while SNO does not. This means that a straight-forward combination of the likelihood spaces will not yield the correct likelihood. Instead, the two analyses would have to be run with the same neutrino fluxes. In addition, systematic uncertainties from the different neutrino interaction models would need to be included. While this would be a complicated analysis, it has the potential to improve the constraints on the atmospheric neutrino oscillation parameters without any new data.

# Bibliography

- [1] F. Reines et al., Phys. Rev. Lett. **15**, 429 (1965).
- [2] C. Achar et al., Phys. Lett. **18**, 196 (1965).
- [3] R. M. Bionta et al., Phys. Rev. Lett. **51**, 27 (1983).
- [4] K. S. Hirata et al., Phys. Rev. Lett. **65**, 1297 (1990).
- [5] C. Berger et al., Nucl. Instrumen. Methods A **262**, 463 (1986).
- [6] C. D. Marzo et al., Nuovo Cim. C **9**, 281 (1986).
- [7] Y. Ashie et al., Phys. Rev. D **71**, 112005 (2005).
- [8] E. Andres et al., Astropart. Phys. **13**, 1 (2000).
- [9] V. A. Balkanov et al., Nucl. Phys. B Proc. Suppl. **91**, 438 (2001).
- [10] W.-M. Yao et al., Journal of Physics G **33**, 1+ (2006).
- [11] P. Adamson et al., Phys. Rev. D **77**, 072002 (2008).
- [12] M. H. Ahn et al., Phys. Rev. D **74**, 072003 (2006).
- [13] S. Abe et al., Phys. Rev. Lett. **100**, 221803 (2008).
- [14] B. Aharmim et al., Phys. Rev. Lett. **101**, 111301 (2008).
- [15] J. P. Cravens et al., Phys. Rev. D **78**, 032002 (2008).
- [16] S. Mikheyev and A. Smirnov, Yad. Fiz. **42**, 1441 (1985).
- [17] L. Wolfenstein, Phys. Rev. D **17**, 2369 (1978).
- [18] S. M. Bilenky and S. T. Petcov, Rev. Mod. Phys. **59**, 671 (1987).
- [19] M. Apollonio et al., Phys. Lett. B **466**, 415 (1999).
- [20] M. Honda, T. Kajita, K. Kasahara, and S. Midorikawa, Phys. Rev. D **70**, 043008 (2004).

- [21] G. D. Barr, T. K. Gaisser, P. Lipari, S. Robbins, and T. Stanev, Phys. Rev. D **70**, 023006 (2004), <http://www-pnp.physics.ox.ac.uk/~barr/fluxfiles/>.
- [22] T. K. Gaisser and M. Honda, Annual Review of Nuclear and Particle Science **52**, 153 (2002).
- [23] T. K. Gaisser, Phys. Scripta **T121**, 51 (2005).
- [24] J. Alcaraz et al., Phys. Lett. B **490**, 27 (2000).
- [25] T. Sanuki et al., The Astrophys. Journal **545**, 1135 (2000).
- [26] S. Haino et al., Phys. Lett. B **594**, 35 (2004).
- [27] M. Boezio et al., The Astrophys. Journal **518**, 457 (1999).
- [28] K. Asakimori et al., The Astrophys. Journal **502**, 278 (1998).
- [29] A. V. Apanasenko et al., Astropart. Phys. **16**, 13 (2001).
- [30] M. Furukawa et al., Proc. 28th Int. Cosmic Ray Conf. (Tsukuba) **4**, 1837 (2003).
- [31] J. Wefel et al., Proc. 28th Int. Cosmic Ray Conf. (Tsukuba) **4**, 1849 (2003).
- [32] P. L. T.K. Gaisser, M. Honda and T. Stanev, Proc. 27th Int. Cosmic Ray Conf. (Hamburg) **5**, 1643 (2001).
- [33] Q. R. Ahmad et al., Phys. Rev. Lett. **87**, 071301 (2001).
- [34] J. Boger et al., Nucl. Instrumen. Methods A **449**, 172 (2000).
- [35] C. Kyba, *Measurement of the atmospheric neutrino induced muon flux at the sudbury neutrino observatory*, PhD thesis, University of Pennsylvania, 2006.
- [36] K. K. S. Miknaitis, *A Search for Matter Enhanced Neutrino Oscillations through Measurements of Day and Night Solar Neutrino Fluxes at the Sudbury Neutrino Observatory*, PhD thesis, University of Washington, 2005.
- [37] K. M. Heeger, *Model-Independent Measurement of the Neutral-Current Interaction Rate of Solar 8B Neutrinos with Deuterium in the Sudbury Neutrino Observatory*, PhD thesis, University of Washington, 2002.
- [38] T. J. Walker, A measurement of the accuracy of the fti muon fitter using the sno external muon system, 2008, <http://manhattan.sno.laurentian.ca/sno/anantob.nsf/URL/MANN-7C4NSM>.
- [39] K. T. e. a. Lesko, Determination of True North for the Sudbury Neutrino Observatory Detector, 2000, <http://manhattan.sno.laurentian.ca/sno/anantob.nsf/URL/MANN-4LS6NN>.

- [40] A. Peisert and F. Sauli, Drift and Diffusion of Electrons in Gasses: a Compilation, 1984, CERN-84-08.
- [41] R. Veenhof, Garfield, CERN Program Library, 1998.
- [42] P. Antonioli, C. Ghetti, E. V. Korolkova, V. A. Kudryavtsev, and G. Sartorelli, *Astropart. Phys.* **7**, 357 (1997).
- [43] I. A. Sokalski et al., Proc. of 2nd Workshop on Methodical Aspects of Underwater/Underice Neutrino Telescopes (Hamburg) (2001).
- [44] M. R. Dragowsky et al., *Nucl. Instrumen. Methods A* **481**, 284 (2002).
- [45] B. A. Moffat et al., *Nucl. Instrumen. Methods A* **554**, 255 (2005).
- [46] D. Casper, *Nucl. Phys. Proc. Suppl.* **112**, 161 (2002).
- [47] P. S. Auchincloss et al., *Z. Phys.* **C48** (1990).
- [48] D. MacFarlane et al., *Z. Phys.* **C26** (1984).
- [49] J. P. Berge et al., *Z. Phys* **C35** (1987).
- [50] D. Rein and L. Sehgal, *Ann. Phys.* **133** (1981).
- [51] C. H. Llewellyn Smith, *Phys. Rep.* **3** (1972).
- [52] R. A. Smith and E. J. Moniz, *Nucl. Phys.* **B43** (1972).
- [53] R. Gran et al., *Phys. Rev. D* **74**, 052002 (2006).
- [54] A. A. Aguilar-Arevalo et al., *Phys. Rev. Lett.* **100**, 032301 (2008).
- [55] P. Lipari and T. Stanev, *Phys. Rev. D* **44**, 3543 (1991).
- [56] G. L. Fogli, E. Lisi, A. Marrone, D. Montanino, and A. Palazzo, *Phys. Rev. D* **66**, 053010 (2002).
- [57] J. A. Formaggio, Applying systematic pulls to a maximum likelihood analysis, 2007, <http://manhattan.sno.laurentian.ca/sno/ananteb.nsf/URL/MANN-76YNPY>.
- [58] Y. Ashie et al., *Phys. Rev. Lett.* **93**, 101801 (2004).